AN ACOUSTIC REMOTE SENSING STUDY OF AN ARCTIC SUBMARINE SPRING PLUME

EUGENE B. COLBOURNE

AN ACOUSTIC REMOTE SENSING STUDY OF AN ARCTIC SUBMARINE SPRING PLUME

BY

© *Eugene B. Colbourne,* B.Sc. (Hons.)

A thesis submitted to the School of Graduate Studies in partial fulfillment of the requirements for the degree of Master of Science

Department of Physics
Memorial University of Newfoundland

October 1987

St John's Newfoundland

ISBN 0-315-39458-7

ABSTRACT

A brackish water plume rising from a submarine spring was mapped using a 192 kHz acoustic sounder and a microwave positioning system. The submarine spring is located at 47 m depth at the head of Cambridge Fiord, Baffin Island. The results demonstrate the advantages of using acoustic remote sensing techniques to detect and characterize buoyant plumes in the ocean. The computer enhanced acoustic images yield critical information on maximum height of rise, plume shape, horizontal extent and vertical velocities in the rising plume. Additional observations included CTD measurements from a launch moored at different positions relative to the plume axis, and visual observations together with CTD and current measurements from a submersible.

The initial geometry and water properties of the flow at the vent together with the ambient stratification were used as inputs to a standard numerical model of a buoyant plume. The maximum height of rise calculated by the model is within the range determined from the acoustic images. The experimental and numerical plume widths show the same general increase with height. The results indicate a freshwater discharge rate of 0.05 to 0.10 m^3/sec. Vertical velocities calculated by the model are of the same order as those inferred from the acoustic images. However, discrepancies exist between calculated and observed variations of velocity with height. Numerical calculations of vertical velocities at 10 m height are about 35 cm/sec and decrease linearly to about 20 cm/sec at 20 m height. Vertical velocities calculated from the acoustic images have a similar magnitude but do not decrease in the 10 m to 20 m height range.

It is shown in the thesis that the radial decay of the acoustic backscatter is too rapid to be explained by simple radial spreading of conservative point scatterers. In fact the radial decay corresponds better to a simple model of turbulence decay. Also experimental observations indicate that the scatterers are not bubbles, suspended sediments or biological organisms. The correlation between the acoustic backscatter intensities and the fine structure in the temperature and salinity field plus the radial decay of these quantities in the spreading plume point to the backscatter mechanism being acoustic refractive index fluctuations caused by turbulent mixing.

ACKNOWLEDGEMENTS

I would like to thank my supervisor Dr. Alex Hay for his guidance and encouragement throughout this project. J. Foley and A. Walsh are thanked for their technical assistance during the field program. The help of A. Kucherra with image processing is greatly appreciated. Roger Guest drafted many of the figures in this thesis. The crews of the PANDORA II and the submersible PISCES IV are acknowledged for their help with the field program. The Keck Laboratory of Hydraulics and Water Resources at the California Institute of Technology is acknowledged for providing us with the computer code for the buoyant plume numerical model. The Bedford Institute of Oceanography and the Atlantic Geoscience Center are acknowledged for loaning us the portable CTD and the microwave positioning system, and also for providing us with current meter data and CTD data translation facilities.

I would also like to thank Dr. A. Hay and Memorial University for the financial support that allowed me to write this thesis. The project was supported by grants from the Natural Sciences and Engineering Research Council, the Department of Energy Mines and Resources Canada, and the Department of Fisheries and Oceans Canada. Finally I would like to thank my wife for her encouragement.

TABLE OF CONTENTS

LIST OF TABLES

LIST OF FIGURES

CHAPTER 1 INTRODUCTION

1.1 Background and purpose

Natural and man made plumes are a common phenomena, but theories describing their dynamics are not fully understood. Common examples include smoke plumes from industrial chimneys, hot gas and dust plumes from nuclear explosions volcanoes, and forest fires, sewage wastewater from ocean outfall diffusers and hot water discharge from thermal power plants. More recently the naturally occurring buoyant plumes from hydrothermal vents and the discharge of groundwater through the sea floor have become a focus for research. Monitoring these man-made and naturally occurring flows is important especially for pollution control, but in lakes and oceans monitoring using conventional measurement methods is difficult particularly if the plume does not emerge at the surface.

Submarine springs and their associated plumes have up until recently been virtually unstudied. Most known springs were discovered either because of some surface manifestation or through SCUBA divers observing the shimmering effect caused by variations in the optical refractive index. These observations are usually only possible in water shallow enough for divers or for the plume to rise to the surface. There is evidence however, suggesting that freshwater discharge occurs at depths as great as 500 m on the Florida continental slope (Manheim, 1967). A recent study by Blume et al. (1981) detected at least 44 submarine freshwater springs around the island of Puerto Rico. These were detected by using a

multifrequency radiometer sensitive to changes in temperature and salinity at the surface.

The submarine spring in Cambridge Fiord was discovered because of the annual formation of a polynya in late winter (Dunbar, 1957). The first study of the polynya was carried out by Sadler and Serson (1980), who made preliminary observations and suggested that the polynya was caused by a submarine freshwater spring. A recent study by Hay (1984) has shown that a freshwater spring does indeed exist, and that the buoyant plume can be detected using a high frequency acoustic sounder, even in the absence of any surface signature.

Turbulent plumes are fluid flows whose main source of energy arises from differences in density giving rise to buoyancy forces, whereas a turbulent jet is generated by a continuous source of momentum. The original analysis of turbulent buoyant jets and plumes was made by Morton et al. (1956), and their integral techniques are well known. Numerical models have been developed by Fan and Brooks (1969), Ditmars (1969) and others that give adequate estimates of mean behavior such as maximum height of rise, rates of spreading and dilution levels. Many other studies have been carried out. Abraham (1967) obtained solutions governing gross jet behavior. Experimental studies by Alberston et al. (1950) have demonstrated the similarity of velocity and concentration profiles. Numerous other numerical models have been written for buoyant jets and plumes some of which include ambient cross-flows. A comprehensive summary of buoyant jets and plumes is contained in a book by Fischer et al. (1979).

Buoyant plumes are a more complicated phenomenon than jets mainly because of the added effects of buoyancy, hence these flows have not been studied in the same detail as jets and are poorly understood. A recent review article by List (1982) concluded that "almost any additional piece of work describing the mechanics of turbulence in plumes will be essentially new work". He also

identified many other areas which require much more research, some of which are: (1) the measurement of temperature and momentum fluxes in buoyant plumes, (2) an evaluation of the entrainment hypothesis particularly for plumes in a density stratified fluid, (3) investigations of the effects of ambient turbulence and cross-flows, (4) and a detailed study of mixing criteria for the spreading plume at neutral density levels in stratified environments, possibly by concentrating on the radial decay of the turbulent kinetic energy.

In this thesis a buoyant plume is studied using acoustic remote sensing techniques. Acoustic imaging has several advantages over conventional physical sampling in the ocean. The most important of these are the large spatial area that can be covered in comparison to the relatively few stations that can be sampled conventionally in the same time period, and the fact that acoustic images are available in real time. During the past few years acoustic remote sensing techniques have been utilized in connection with several physical processes in the ocean. Acoustic images have been obtained of large amplitude internal waves and other hydraulic phenomena in widely differing parts of the ocean (e.g. Haury et al., 1979; Farmer and Smith, 1980; and Hay and Colbourne 1987). Acoustic imaging techniques have also been used in sediment transport studies (Young et al., 1982; Vincent et al., 1982), including turbidity currents (Hay, et al., 1982; Hay, 1983). In a recent study Palmer and Rona (1986) claim to have detected high temperature hydrothermal plumes at seafloor spreading centers using a sonar from a submersible. Merewether et al. (1985) have reported acoustic observations of plumes in Guaymas Basin of the Gulf of California. These plumes were interpreted as light hydrocarbons escaping from natural seeps on the seabed. One of the outstanding problems in interpreting some of the imagery has been the degree to which scattering from turbulent microstructure is important.

The scattering of sound by density inhomogenities has received more atten-

tion in the atmosphere than in the ocean (eg. Tatarski, 1961; Ottersten et al. 1973). Backscatter results from fluctuations in the acoustic refractive index at scales of about one-half the acoustic wavelength. Expressions for acoustic scattering cross-sections from turbulent fluctuations in the temperature and salinity fields in the ocean have been derived by Batchelor (1957). Recent studies by Pelech et al. (1982) and Thorpe and Brubaker (1983) have detected significant acoustic backscatter levels from turbulent microstructure produced artificially by towed bodies. Acoustic backscatter may also result from large changes in the acoustic impedance associated with sharp thermoclines (Weston, 1957; Kaye, 1978). A major problem in the ocean is in discriminating biological scattering from that due to turbulence, especially near thermocline regions. A recent theoretical study by Goodman and Kemp (1981) indicates that scattering from oceanic turbulence can exceed that from biological scatterers. Munk and Garrett (1972) estimated that acoustic scattering cross-sections from layered microstructure can be 10 to 50 dB above that from biological scatterers.

In this thesis the use of acoustic remote sensing to study the buoyant plume in Cambridge Fiord is explored further. It will be shown that this technique can give important information on plume characteristics. Acoustic backscatter amplitudes are compared to fine structure amplitudes in the temperature and salinity fields in an attempt to relate sound scattering to turbulent intensities. A complete understanding of the physical mechanism responsible for the acoustic scattering is very important if we are to gain the full benefit from these remote sensing techniques.

1.2 Physical description of study area

This study was a part of a multidisciplinary investigation of several fjords on the East coast of Baffin Island. Figure 1.1 shows Baffin Island and the

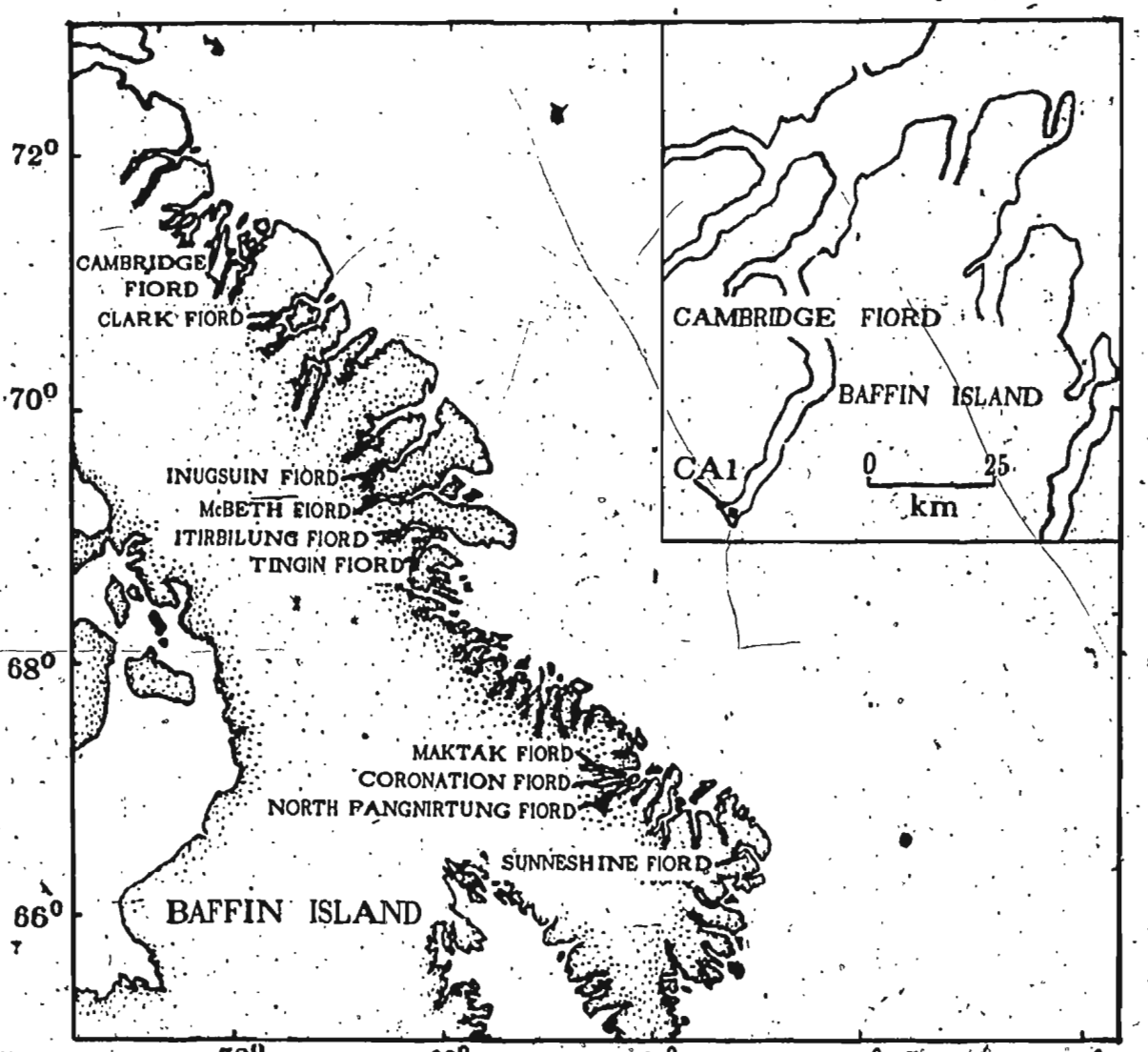

Figure 1.1 Location map showing Baffin Island and the Cambridge Fiord study area.

Cambridge Fiord study area. Station CA1 marks the location of the submarine spring experiment conducted in September of 1985. The fjord reaches inland for about 100 km and has a low tidal range, typically less than 1.0 meter.

Figure 1.2 shows the main features of the fjord delta system, and the large scale bathymetry. The head of the fjord is made up of two delta systems separated by a 500 m high plateau. To the northwest we have the Keel River delta. The southern delta consists of raised terraces up to 75 meters above sea level. The front of the raised delta is lined by a narrow beach. A freshwater lake of about 1.5 km^2 area is located approximately 3 km from the head of the fjord. This lake is drained by a seasonal stream which has cut a channel through the raised delta and enters the fjord near the eastern end of the beach.

The existence of a polynya about 50 m in diameter at the head of this fjord was noted by Dunbar (1957). The position of the polynya is shown as the solid circle just inside the 50 m isobath. The annual formation of this polynya in late winter was confirmed by a series of aerial survey photographs taken by the Royal Canadian Air Force between 1952 to 1957 and also reported by Inuit hunters from nearby Pond Inlet. Figure 1.3 shows a section of an aerial photograph of the head of Cambridge Fiord showing the polynya and a shore lead. Also shown is the seasonal stream channel in the lower half of the photograph. Sadler and Serson (1980) suggested that a submarine spring was responsible for the formation of this polynya. The groundwater discharge is believed to be channeled through the delta from the lake shown in Figure 1.2. The water level of this lake was found to decrease by approximately 1.0 to 2.0 m during the winter runoff-free period as determined from examination of sterio photographs and communications with Inuit hunters. This is equivalent to a discharge rate of 0.06 to 0.13 m^3/sec assuming a constant flow from September to May. A discharge rate of 0.14 m^3/sec was determined from heat loss considerations through the polynya (Sadler and Serson,

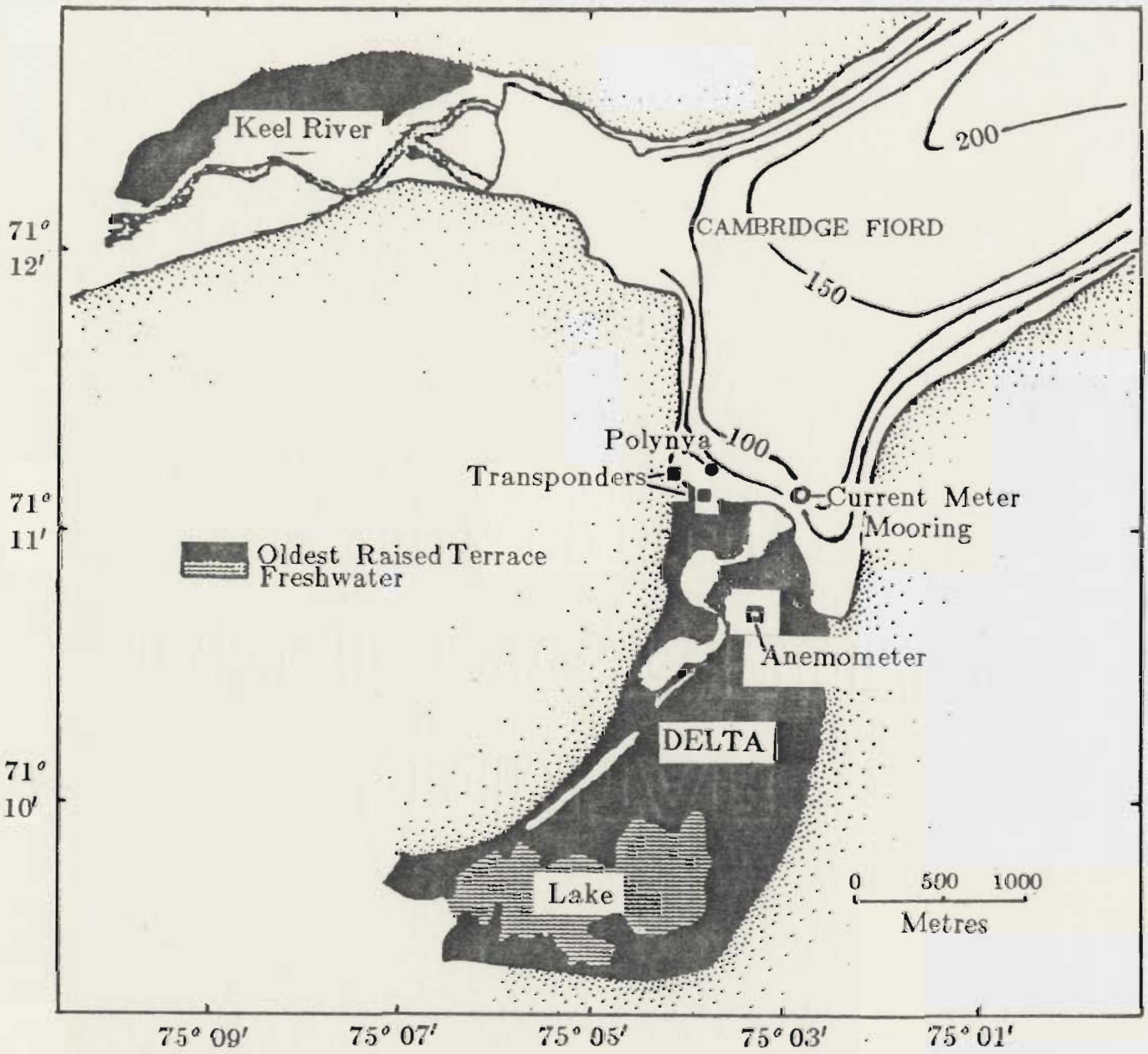

Figure 1.2 Main features of the head of Cambridge Fiord, the position of the polynya is marked by the solid circle.

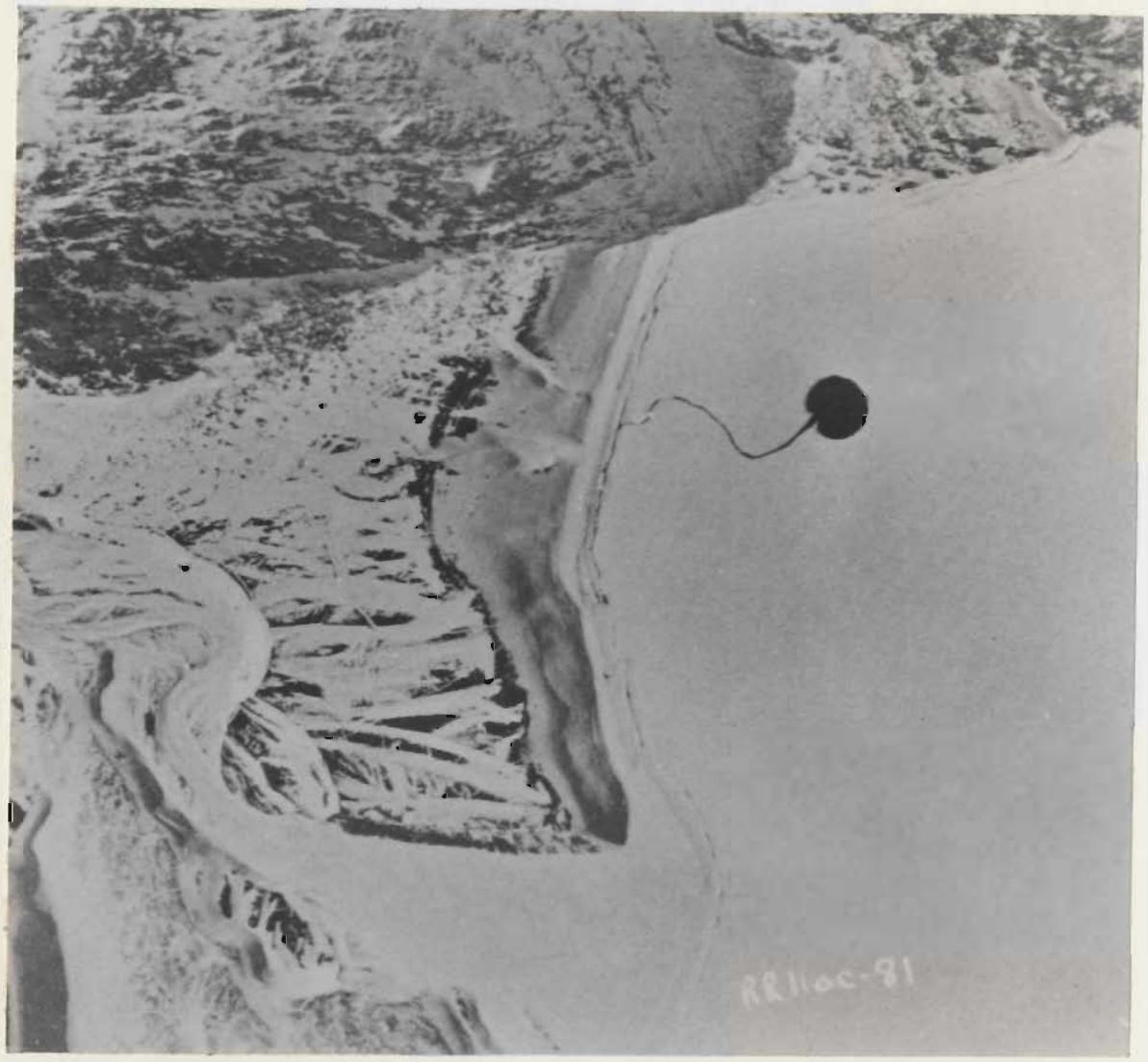

Figure 1.3 An aerial photograph of the head of Cambridge Fiord taken in April 1952, showing the polynya (taken from Sadler and Serson, 1980).

1980).

1.3 Organization of the thesis

This thesis is organized into 7 chapters. Chapter 2 includes a description of the field programs and a summary of the data collection and data processing methodology. Chapter 3 discusses the buoyant plume behavior and geometry in the context of data collected in 1983 and 1985. Chapter 4 describes the ambient environment during the 1985 experiment. Chapter 5 presents the comparisons between different plume models and the experimental data. Acoustic backscatter and turbulent fine structure in the temperature and salinity fields are discussed in Chapter 6. The seventh chapter gives a summary and the conclusions of the thesis.

CHAPTER 2 DATA SOURCES AND ANALYSIS

Field programs

Two field programs were carried out. The first took place in September 1983 aboard the C.S.S. HUDSON and the scientific launch GREBE. The second took place in September of 1985 with the PANDORA II and the submersible PISCES IV. The ship's launch ORCA was also used extensively during this field program.

2.1 The 1983 field program

Observations were made from the launch while four-point moored over the vent area. Most of the acoustic backscatter were recorded on chart paper. A small portion were recorded on magnetic tape for later processing. A total of 14 vertical CTD profiles were completed in the general area of the plume. Another four horizontal CTD profiles were obtained with the CTD package held in its normal orientation but moved horizontally while at constant depth using a pulley system integral to one of the mooring lines. Measurements were made for 1 to 2 minute intervals at probe positions separated by 1 m. Vertical velocities were also obtained with a current meter mounted in a horizontal orientation on a lead-ballasted frame held at fixed depths.

2.2 The 1985 field program

A current meter mooring and anemometer were deployed from a helicopter by personnel from the Atlantic Geoscience Center in early August. These instruments were used to monitor the ambient environment at the head of the fjord during the field program.

We were on location at the head of Cambridge Fiord with PANDORA II and PISCES IV for three days. During day 1 and 2 four dives were made to the vent site with PISCES, day 3 consisted of launch operations. Measurements and observations from the ship's launch were made difficult by waves generated by persistent high-speed up-inlet winds. We were restricted to working daylight hours only, for safety reasons.

The plume was easily located from the launch ORCA using an acoustic sounder. Navigation by PISCES was made possible by acoustic direction finding with a pinger deployed by ORCA at the vent. Measurements made with PISCES included vertical and horizontal velocity components, salinity, temperature and stereo bottom photography using a Photosea 2000 camera system. Also 15 water samples for laboratory analysis were taken using the submersible's rotary water sampler. In addition to these measurements photographic and visual observations were made from within the submersible.

The mooring lines used to four-point moor the launch over the vent which had been deployed in 1983, were dragged for and recovered in 1985 with little difficulty. The launch with the aid of the ship's inflatable boat was used to set up shore transponders for a microwave positioning system. Near the end of day 2 the plume was mapped by running 23 acoustic sounding lines. On day 3 the launch was used to map the plume with a grid of 23 CTD stations. Five more soundings lines were also made at the end of the day.

2.3 Instruments and methods

The positioning system used was a Motorola Miniranger with a rated accuracy of 1.0 to 2.0 m. The positions of the microwave transponders on the beach in front of the delta face are marked by solid squares in Figure 1.2. The baseline distance between the two transponders was 229 m. This was measured using an infrared Topcon DM-A2 distance measuring unit. Acoustic sounding transects spaced at approximately 10 m intervals were conducted by executing circular arcs around each shore transponder in the general area of the plume.

The brackish water plume from the submarine spring was mapped from the launch using an acoustic sounder. The sounder was a commercial prototype built by Ross Laboratories, Inc. The transmitted output power was 400 V peak-to-peak or 800 watts rms, the receiver had a sensitivity of 0.65×10^{-6} V over a bandwidth of 5 kHz. The transducer consisted of 32 barium titanate elements and had a resonant frequency of 192 kHz. The beamwidth, the angle between the half power points of the main lobe, was estimated to be 2.3° (Hay, 1983). The sounder was operated with a pulse length of 0.5 ms giving a range resolution of approximately 40 cm. The pulse repetition interval of the sounder was 270 ms. The analog acoustic backscatter signals and the trigger pulse were recorded on separate FM channels of a Racal Store 4 instrumentation tape recorder. The recorded signal was the envelope of the full wave rectified, low pass filtered echo.

The backscattered signals were monitored in real time on a Tektronix model 465B portable oscilloscope. The recordings were made at a tape speed of 38.1 cm/sec, for which the recorder's frequency response was flat from 0 to 5 kHz, -3 dB at 6.2 kHz, and -20 dB at 10 kHz. The rms tape noise level was approximately -43 dB at 3 kHz. Each analog tape was calibrated by recording the 3 DC levels from the recorder's calibrator output. The analog signal was digitized on a HP

model 5451B Fourier Analyzer at an effective rate of 20 kHz by using a playback tape speed of 19.1 cm/sec and a sampling rate of 10 kHz. The recorded trigger pulse was used to activate a 4096-point digitizing window giving a sampling interval of 0.025 ms. The acoustic data were processed on a VAX 11/785 and a HP-1000 computer system. False color images of the plume were constructed from the acoustic data using a Norpak VDP-11 image processing system. Figure 2.1 shows a block diagram of the acoustic data acquisition and processing systems.

A second acoustic mapping of the plume was made in conjunction with a grid of CTD stations while the launch was four-point moored. The CTD measurements were obtained using a Guildline model 8770 portable CTD system. The analog output of the CTD deck unit was recorded on an audio stereo cassette deck. The analog tapes were digitized and translated using facilities at the Bedford Institute of Oceanography. The time interval between successive pressure, conductivity and temperature records was 190 ms. The characteristics of this CTD system are given in Table 1. Typical ascent and descent rates were of the order of 0.3 m/sec giving a spatial resolution of about 5 cm outside the rising plume.

The vertical current measurements were made from PISCES with a Neil Brown Instrument Systems DRCM-2 acoustic current meter. The time interval between successive speed and direction measurements was 0.5 seconds. The specifications of this current meter are given in Table 2. The current meter was mounted on the remote manipulator arm of PISCES IV. Measurements were made while the submersible was sitting on the bottom and the current meter maintained in a horizontal orientation using externally mounted spirit levels. The analog output of the DRCM deck unit was recorded on an audio cassette

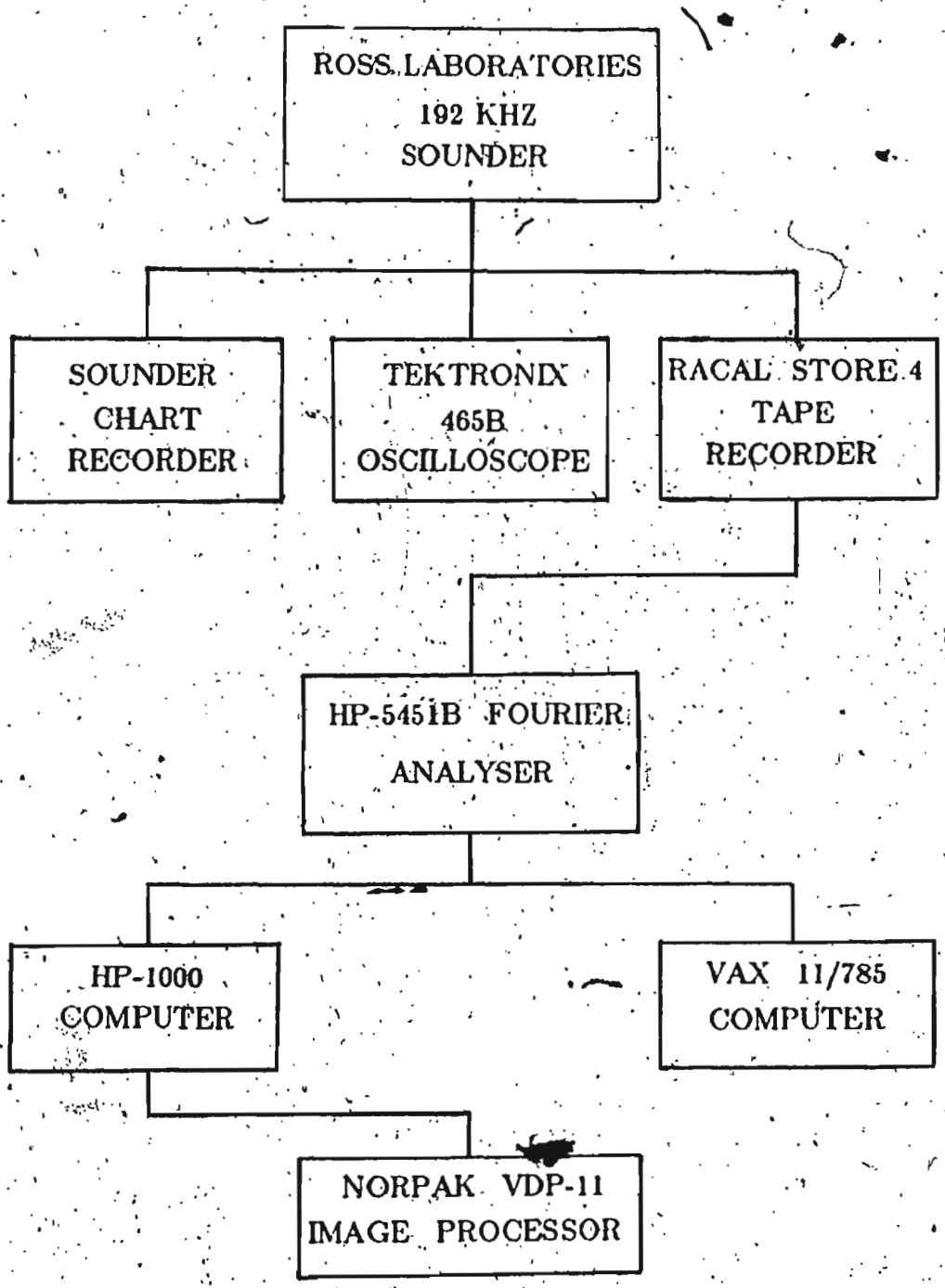

Figure 2.1 Block diagram of acoustic data acquistion and processing.

Table 1. Guildline CTD Characteristics.

	Resolution	Accuracy	Response Time
Pressure	0.123 dbars	±2.0 dbar	<1 msec
Temp.	0.00512 °C	±0.02 °C	60 ms
Cond Ratio	0.000195	±0.004	60 ms
Salinity	0.01 ppt	±0.04 ppt	

Table 2. Neil Brown Current Meter Specifications.

	Range	Accuracy	Response Time
Velocity	0-250 cm/sec	±1.0 cm/sec.	0.2 sec
compass	0-360 Deg.	±2.0 Deg.	0.2 sec
Temp.	3.0-32.7 °C	±0.05 °C	10 sec
Pressure	0-100 psi	0.5%	1.0 sec

tape deck. The serial output of the deck unit on playback was standard ASCII characters which were dumped directly to the VAX 11/785 for further processing.

2.4 CTD data processing

CTD data processing was done on the VAX 11/785 computer system. The pressure time series was smoothed by computing a sliding 15-point least squares fit to a second order polynomial. This eliminated the small amplitude random changes in the pressure arising from the low resolution of the digital output from the portable system (0.12 dbar per least significant bit) and noise in the least significant bit of the pressure word. Salinities and densities were then computed using the UNESCO 1978 practical salinity scale. A first edit of the CTD data was performed at BIO when the analog tapes were translated. Any remaining spikes

in the data were manually edited on the VAX. Profiles of temperature, salinity and sigma-t were then plotted for each cast. CTD measurements made from ORCA and PISCES with the probe at constant depths were plotted as time series of temperature, salinity and sigma-t.

The rms fine structure variations in temperature and salinity were computed by high pass filtering the data. The coefficients of the filter are given by

$$A_k = \frac{1}{2}\left(1 + \cos\frac{k\pi}{n}\right)\frac{\sin(k\pi\delta t f_c)}{2\pi k\,\delta t f_c} \qquad (2.1)$$

where k is the index number of each coefficient and n is the total number of filter coefficients, δt is the sampling interval and f_c is the cutoff frequency. The filter can be used in either a high pass or a low pass mode. The vertical CTD profiles were treated as time series. The probe descent rate of 0.35 m/sec was determined from the slope of the probe echo in the acoustic images. From the total number of scans per profile a sampling rate of 5.4 Hz was determined. A filter length of 21 samples or approximately 4 seconds and a cutoff frequency of 0.3 Hz was used. This filter length and cutoff frequency correspond to spatial scales of 1.5 and 1.0 m respectively. The square of the fluctuations in temperature and salinity were then block averaged over a time interval corresponding to the range resolution of the sounder. This interval was chosen in order to compare the rms fluctuations in temperature and salinity with the acoustic backscatter at the same depth.

2.5 Acoustic signal processing

We will consider a typical monostatic sonar system in which the same transducer is used to transmit and receive. Suppose that the scatterers are uniformly distributed across the width of the main lobe of the transducer antenna pattern,

which can be approximated by a cone. Then the incident sound pressure amplitude is given by

$$p_i = \frac{p_0 r_0}{r} e^{-\alpha r} D \tag{2.2}$$

where r is the range, r_0 and p_0 are reference values, D is the directivity factor for the transducer and α is the sound absorption coefficient. The backscattered amplitude of the sound pressure in given by

$$p_s = p_i \frac{D}{r} e^{-\alpha r} F_s \tag{2.3}$$

where F_s is a coefficient representing scattering strength of the targets. The detected amplitude of the backscattered wave at the transducer for a particular spatial configuration of scatterers in a given range cell (defined later) is

$$p_d = \sum_{j=1}^{N} p_{sj} e^{i\phi_j} \tag{2.4}$$

where N is the total number of particles in the range cell, and ϕ_j and p_{sj} are the phase and amplitude of the wave from the jth scatterer, i in this case is defined as the $\sqrt{-1}$. The square of the magnitude of the backscattered pressure level from any given range cell is given by

$$|p_d|^2 = \sum_{j=1}^{N} p_{sj} e^{i\phi_j} \sum_{k=1}^{N} p_{sk} e^{-i\phi_k} \tag{2.5}$$

which can be written as

$$|p_d|^2 = \sum_{j=1}^{N} p_{sj}^2 + \sum_{j \neq k}^{N} \sum p_{sj} p_{sk} e^{i(\phi_j - \phi_k)} \tag{2.6}$$

The instantaneous pressure waves from a particular range for a particular ensemble of scatterers are incoherent if the positions of the scatterers are random functions of time. Therefore the mean square pressure level at a given range for an

average over several pings is given by

$$\langle | p_d |^2 \rangle = \sum_{j=1}^{N} p_{sj}^2 \tag{2.7}$$

provided that the $\phi_j - \phi_k$ vary randomly from ping to ping. The angle brackets denote the average over all possible configurations of scatterers.

We approximate the main lobe of the transducer antenna pattern by a cone and define ϕ_0 to be the angle characterizing its half width. Then the detected volume element or range cell is written as

$$\int_0^{2\pi} \int_0^{\phi_0} \int_{r - c\frac{\tau}{4}}^{r + c\frac{\tau}{4}} r^2 \sin\phi \, dr \, d\phi \, d\theta \tag{2.8}$$

where τ is the duration of the transmitted pulse, or pulse length, and c is the speed of sound. The quantity $c\frac{\tau}{2}$ is then the range resolution of the sounder.

The effective backscattered pressure at the transducer due to a large number of randomly distributed scatterers can be found by integrating over this volume element and using Eq. (2.3) and Eq. (2.7) to give

$$\langle | p_d |^2 \rangle = \int_0^{2\pi} \int_0^{\phi_0} \int_{r - c\frac{\tau}{4}}^{r + c\frac{\tau}{4}} r^2 \sin\phi \, dr \, d\phi \, d\theta \, p_i^2 D^2 \frac{e^{-2\alpha r}}{r^2} F_s^2 n \tag{2.9}$$

Assuming n, the number of particles per unit volume is independent of r, θ and ϕ within the volume element and substituting for the incident pressure p_i from Eq. (2.2) we obtain, assuming the volume element thickness is very small compared to the range,

$$\langle | p_d |^2 \rangle = \left[\pi p_0^2 r_0^2 c \, \tau F_s^2 n \int_0^{\phi_0} \sin\phi \, D^4 \, d\phi \right] \frac{e^{-4\alpha r}}{r^2} \tag{2.10}$$

The rms pressure level is now given by

$$<|p_d|^2>^{1/2} = \left[\pi p_0^2 r_0^2 c\, \tau F_\theta^2 n \int_0^{\phi_0} \sin\phi D^4 d\phi\right]^{1/2} \frac{e^{-2\alpha r}}{r} \qquad (2.11)$$

The quantity given by Eq. (2.11) is proportional to the rms measured voltage.

With the discussion leading to Eq. (2.7) in mind the acoustic data profiles used in this thesis were averaged over 5 consecutive pings and over the pulse length (about 40 cm) in the vertical. The acoustic backscatter signals were corrected for spreading and attenuation by multiplying the measured signal level by the factor $r\exp(2\alpha r)$ according to Eq. (2.11). The signal was then depth-normalized by dividing this corrected signal by the factor $r'\exp(2\alpha r')$. The total corrected signal is then given by $v' = v_{rms}\, F$ where F is given by

$$F = \frac{r}{r'} e^{2\alpha(r - r')} \qquad (2.12)$$

and v_{rms} is the measured backscatter amplitude, r' is one-half the total water depth.

The attenuation of sound in seawater can be attributed to viscous absorption by water molecules and the molecular relaxation of magnesium sulfate and boric acid. The attenuation coefficient can therefore be written as the sum of three terms, neglecting any attenuation due to the scatterers themselves.

$$\alpha = \alpha_F + \alpha_{MgSO_4} + \alpha_{BoricAcid} \qquad (2.13)$$

The attenuation coefficient in m^{-1} in seawater at 0°C and shallow water depths is given by (Clay and Medwin, 1977).

$$\alpha = 5.70 \times 10^{-8} f^2 + 2.34 \times 10^{-6} \frac{S f_{rm} f^2}{(f_{rm}^2 + f^2)} \qquad (2.14)$$

where f is the frequency of the incident sound wave in kHz, S is the salinity in

ppt and f_{rm} is the molecular relaxation frequency of magnesium sulfate (59.2 kHz at 0°C). The pressure dependences and boric acid contributions have been dropped since they are small for the depths and the frequency of interest. The attenuation coefficient at 0.0 °C and 31.0 ppt salinity was calculated to be 5.97×10^{-3} m^{-1} at 192 kHz.

Acoustic data profiles parallel to the descending CTD package were constructed from the data. These profiles were then block averaged over the resolution of the sounder (about 40 cm) and compared directly with the rms fluctuations in temperature and salinity over the same depth interval.

2.6 Wind and current meter data processing

The wind data were obtained from an Aanderaa RWS anemometer mounted on the raised terrace about 75 m above sea level. The position of the anemometer is shown by the open square in Figure 1.2. Recordings were made at 20 minute intervals from August 12 to September 21 1985. These data were translated and edited at the Bedford Institute of Oceanography and supplied on 9 track magnetic tape. The wind data were decomposed into NNE and WNW directions. The NNE component is aligned roughly with the fjord axis. The positive down-inlet or axial component blows towards the 32 degrees true direction and the positive cross-inlet or transverse component blows towards the 302 degrees true direction. A magnetic deviation of -58 degrees was applied to the wind direction. Wind speed and direction were also obtained from the ship's log for September 20 and 21, the period of the experiment.

The ambient currents and water temperatures at the head of the fjord were monitored during the same period by two moored Aanderaa RCM current meters. These instruments were placed at 9 and 48 m depth in about 50 m of water

approximately 500 m from the plume. The position of the current meter mooring is shown in Figure 1.2 as the open circle. The current meters have a threshold of 1.5 cm/sec. Current speed, direction and temperature were sampled at 10 minute intervals. Translation of the Aanderaa data into physical units was also performed at BIO. The data were edited and a magnetic deviation of -58 degrees was added to the direction channel at the time of translation. The current velocity components were resolved in the same direction as the wind data, ie. parallel and perpendicular to the axis of the fjord. The wind and current meter data were low pass filtered using the filter already described.

CHAPTER 3 PLUME AND VENT OBSERVATIONS

3.1 Bathymetry

Figure 3.1 shows a rough bathymetric chart of the vent area centered at about 210 m offshore. This map was constructed from the depths at all position fixes for the survey. The solid squares and circles indicate fixes from transects centered on the different transponders. These depths were then plotted and the contours were drawn by hand. The offshore distance is perpendicular to the beach along the delta face and the alongshore distance is along the beach in a northwestward direction. The bottom slope is about 10 degrees in the general area of the vent. The approximate position of the vent coincides with CTD cast number 2 along the 47 m isobath. The positions of all CTD's obtained during the survey are indicated by the plus signs. The numbers correspond to the sequential CTD cast.

3.2 Acoustic transect images of the plume

The false color images shown in Figure 3.2 constructed from the acoustic data were displayed on a Norpak VDP-11 image processing system. Each digitized ping was displayed as a time series in the horizontal. The images were enhanced by both thresholding and contrast stretching. The images are made up of 430 by 590 pixels. The signal range of 0 to 0.65 volts is first fitted linearly to the 0 to 255 grey scale. A false color is then applied to this grey scale with red

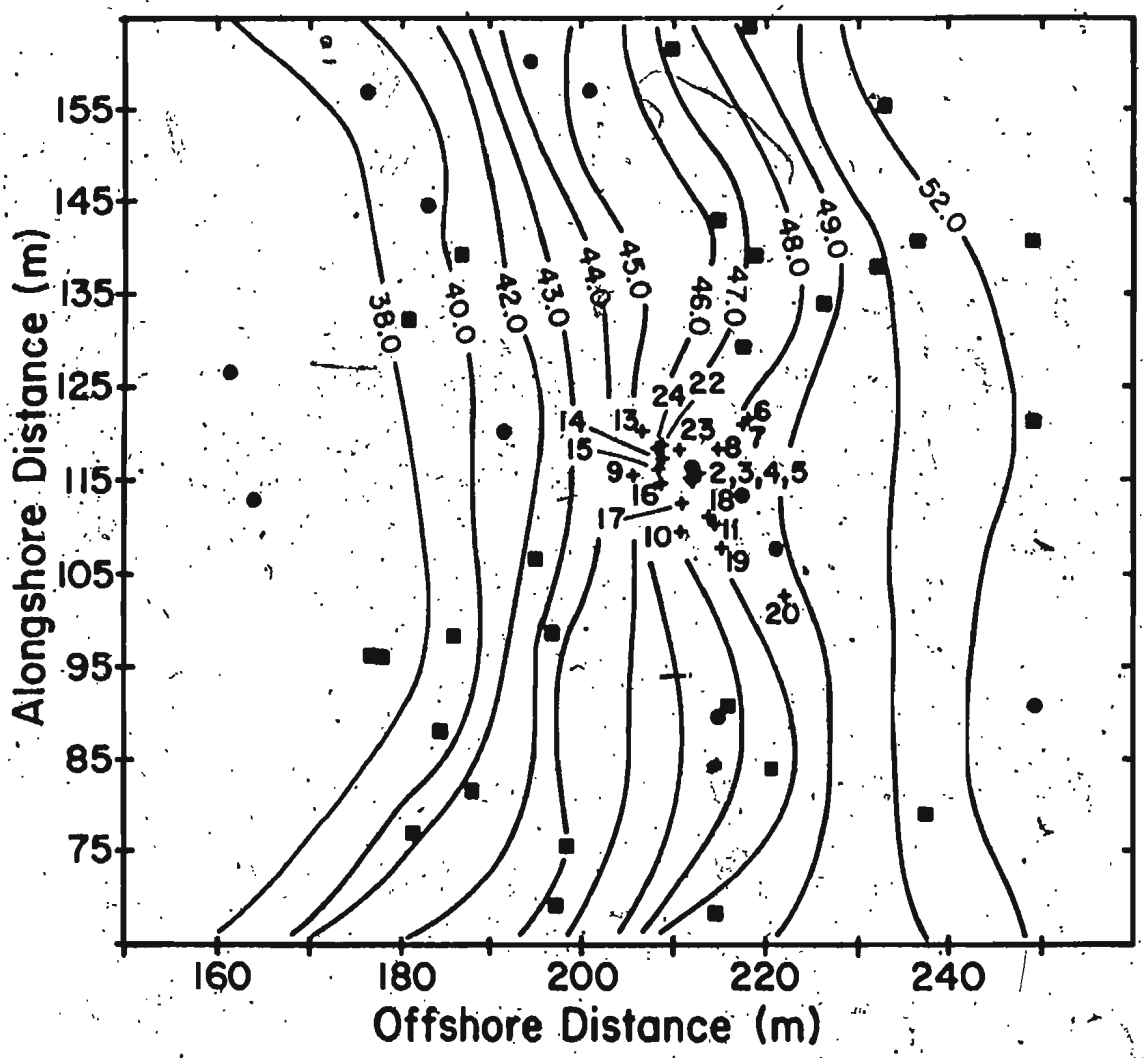

Figure 3.1 Bathymetric chart of vent area produced from depths at position fixes. The position fixes are marked by solid squares and circles, CTD positions are marked by the plus signs and indicated by their cast number.

representing high signal level. The detector saturation level of 0.65 volts is assigned black and the background level is turned white. A typical image consists of 1000 pings or records each 4096 data points in length. Averaging over sets of 6 data points in the vertical by 2 records in the horizontal was necessary to fit this image to the available number of pixels. Any image consisting of less than 600 pings was not averaged in the horizontal.

The horizontal scale of these images is determined by the pulse repetition interval of 0.27 seconds per ping and the minimum speed of the launch of about 2.5 knots. The total length of the transect in panel A is about 188 m giving a horizontal scale of approximately 75 m per minute. Panel A in Figure 3.2 shows a false color image of an acoustic transect acquired while steaming over the vent as described in section 2.3 of Chapter 2. Panel B shows a corresponding image acquired while steaming over the vent around the opposite transponder. The narrow approximately vertical rising plume can be seen to overshoot its height of neutral buoyancy due to its vertical momentum, reach its maximum height of rise at 15 to 17 m depth and then fall back to spread radially outward along isopycnal surfaces at depths of 20 to 30 m. Similar images obtained in 1983 show the plume extending from the bottom up to a minimum depth of 9 m and spreading out horizontally between 12 and 20 m depth. These differences in height of rise are due to different ambient stratification as will be shown in Chapter 5. The amplitude of the acoustic backscatter decreases with radial distance from the plume axis. Large numbers of euphausiids were observed from the submersible and probably caused the near bottom zone of high amplitude backscatter. The periodic nature of this zone, particularly evident in panel A, is due to the launch rolling in about 1 to 2 m seas. The appearance of more than one closely spaced rising plume is probably due to this same wave-induced launch motion, causing the sound beam to swing in and out of the rising plume.

Figure 3.2 False color images of the plume from acoustic transects.

Panel A shows an image obtained while steaming over the vent.

Panel B is the same as A but the sounding transect is centered on the opposite transponder.

Panel C shows an image acquired while steaming over the spreading plume.

Panel D shows an image acquired while steaming over the vent one day later. This image was recorded at a lower receiver gain than Panels A to C.

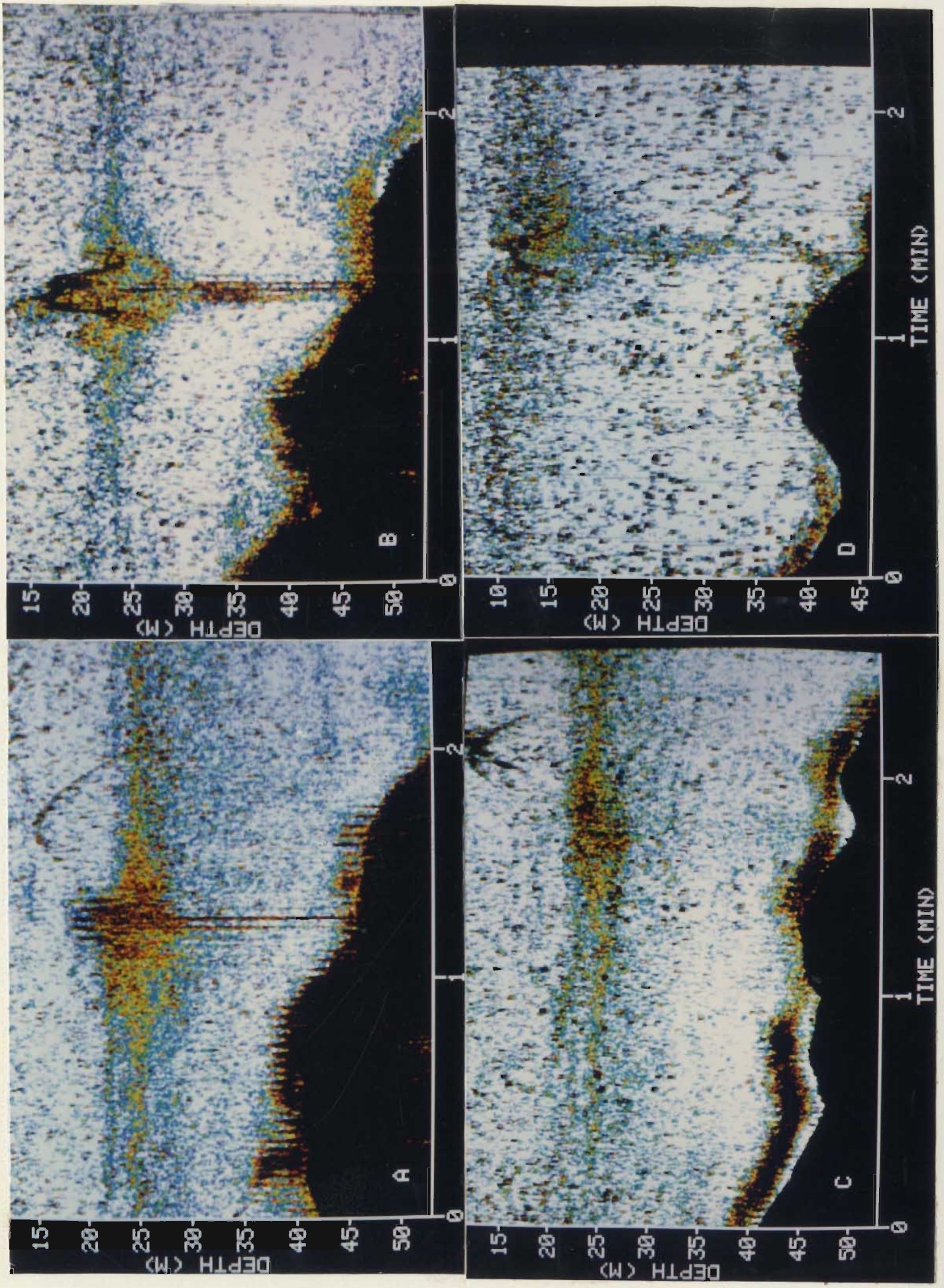
A
B
C
D
DEPTH (M)
TIME (MIN)
0
1
2
15
20
25
30
35
40
45
50
10

The image shown in panel C was acquired while steaming over the spreading plume to one side of the vent or rising plume axis. The plume appears to be spreading out between 20 and 25 m depth. Tongues of plume water are seen to be spreading out along vertically separated surfaces. Again we see the near bottom zones of high backscatter caused by euphausiids and probably other biological organisms. The image shown in panel D in Figure 3.2 was acquired while steaming over the vent one day later. This image was recorded at a lower receiver gain than the first three. An increase in the maximum height of rise of 5 m is seen in this image. This is believed to be related to changes in ambient stratification associated with a reduction in the speed of up-inlet winds. It will be shown in Chapter 5 how wind-induced changes in ambient stratification affects the maximum height of rise.

3.3 Maps of acoustic backscatter amplitude as a function of depth

Figure 3.3 shows typical acoustic maps of the spreading and rising plume in horizontal cross section at selected water depths. These maps were constructed from 9 consecutive acoustic transects by taking horizontal cross sections averaged over one meter in the vertical. The first two maps at 20 and 23 m depth were averaged over 2 m in the horizontal while the last two at 32 and 42 m were averaged over 1.0 m. The contours represent different levels of backscatter signal. The contouring interval is 0.1 volt with the highest level contour at 0.5 volts around the center of the plume, on a scale of 0.0 to 0.65 volts. The average background level of 0.1 volt has been removed. The signal level has been corrected for attenuation and spreading according to Eq. (2.11). The plume width at any depth has been corrected to take into account the width of the main lobe of the transducer beam pattern by reducing the horizontal extent of the plume by a factor

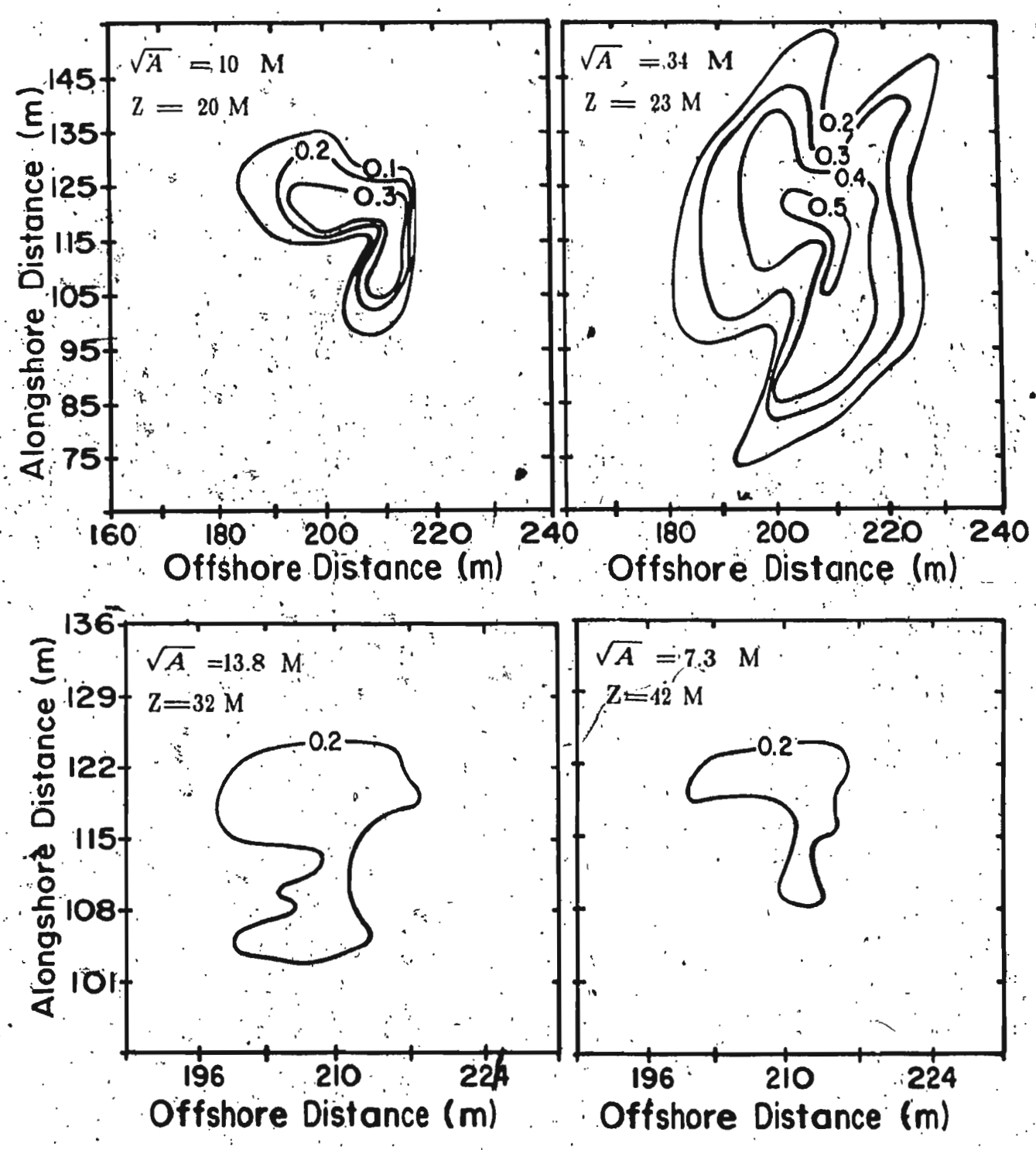

Figure 3.3 Typical horizontal maps of the plume from acoustic backscatter data at selected depths.

equal to the beam width at that particular depth. For example at 40 m depth and a sounder beam width of 2.3° the plume width would be reduced by 1.6 m on each side.

The alongshore extent of the plume at 23 m depth is approximately 80 m and the offshore extent is about 45 m. We define a characteristic width of the plume as the square root of the area enclosed by the 0.2 volt contour. The characteristic width of the plume at 20 m depth is about 10 m and at 23 m depth about 34 m. The characteristic width increases with depth to about 26 m after which it decreases to 15 m at 32 m depth, and to 6.8 m at 42 m depth. No plume widths below 42 m were calculated due to the near bottom scattering zones merging with the signal from the plume itself. Plume widths were determined from the horizontal maps in this way at 1 m intervals from 18 to 42 m depth. A plot of plume width versus height above bottom is shown in Figure 3.4. The plume width is seen to be roughly constant in the first 10 m after which it increases almost linearly up to 30 m depth. Above this point the plume starts to spread horizontally and hence the widths increase very rapidly.

3.4 Detailed bathymetry from interpolated positions

Figure 3.5 and 3.6 show detailed bathymetric charts of the vent area obtained from the acoustic transects around each transponder. As in Figure 3.1 the offshore and alongshore distance is perpendicular and parallel to the beach respectively. Bottom depths were selected from the digitized acoustic records along each transect. The bottom transects were then edited to remove spikes resulting from biological scatterers. Finally the transects were 5-point smoothed and sampled at 1.0 m intervals to produce the bottom contours. The acoustic transects are indicated by the broken lines. These lines were obtained by taking

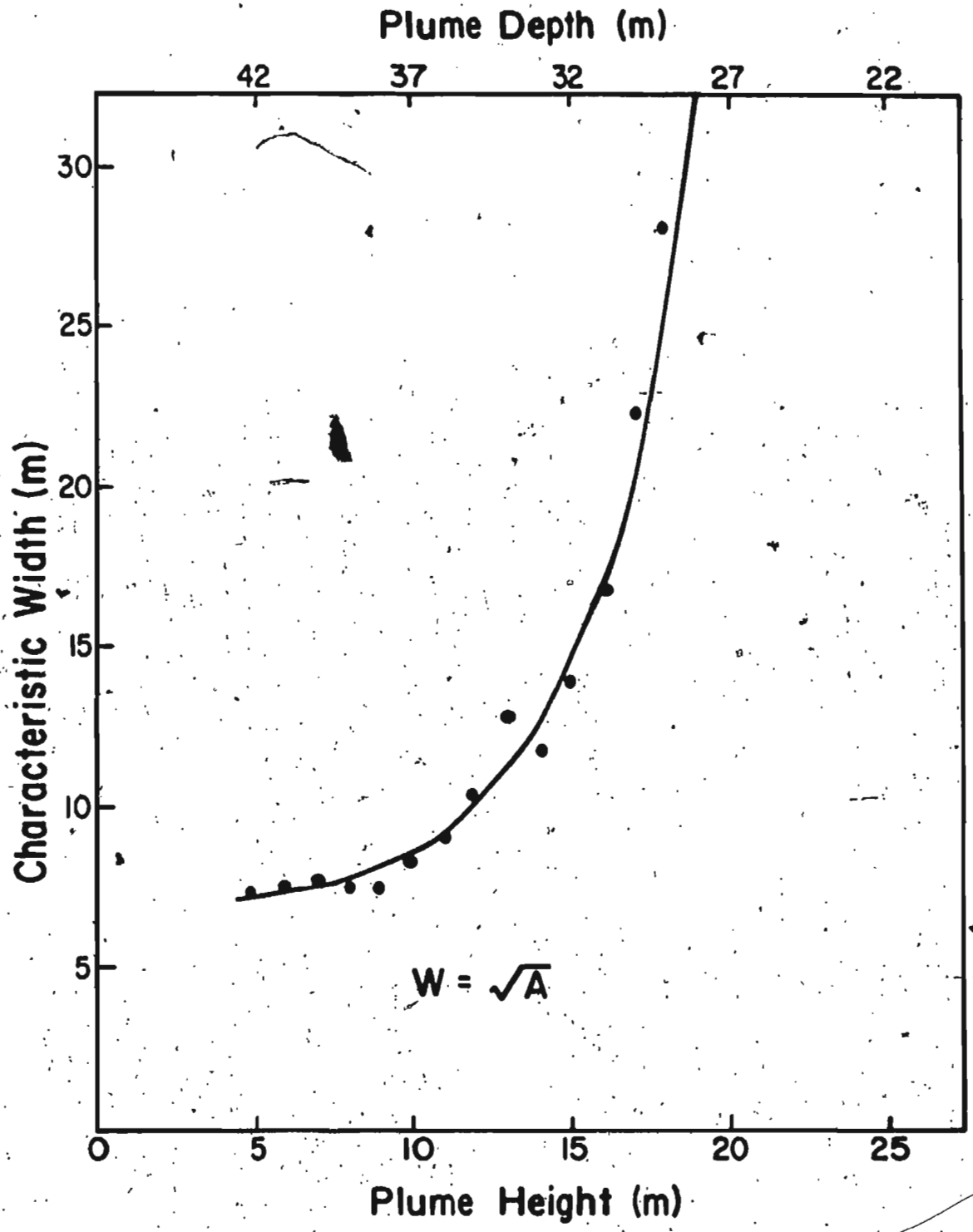

Figure 3.4 Characteristic plume widths versus depth and height determined from the horizontal acoustic maps.

the average radius of all fixes for each transect. Again the approximate position of the vent is marked and coincides with the 47 m isobath.

The differences in the bathymetry seen in Figures 3.1, 3.5 and 3.6 are probably due to the fitting procedure used to map the transects, and it should be noted that this could also introduce artificial structure in the horizontal maps of the acoustic backscatter amplitudes in Figure 3.3. Difficulties were experienced in maintaining the launch at a constant distance from the pivot transponder. This was also partially due to the rough seas. As a result the paths around each pivot transponder were not perfect circular arcs. Another possible source of error could result from side echo especially in regions with steep bottom slopes. The problem would not seriously affect the plume cross-sectional areas and widths inferred from Figure 3.3.

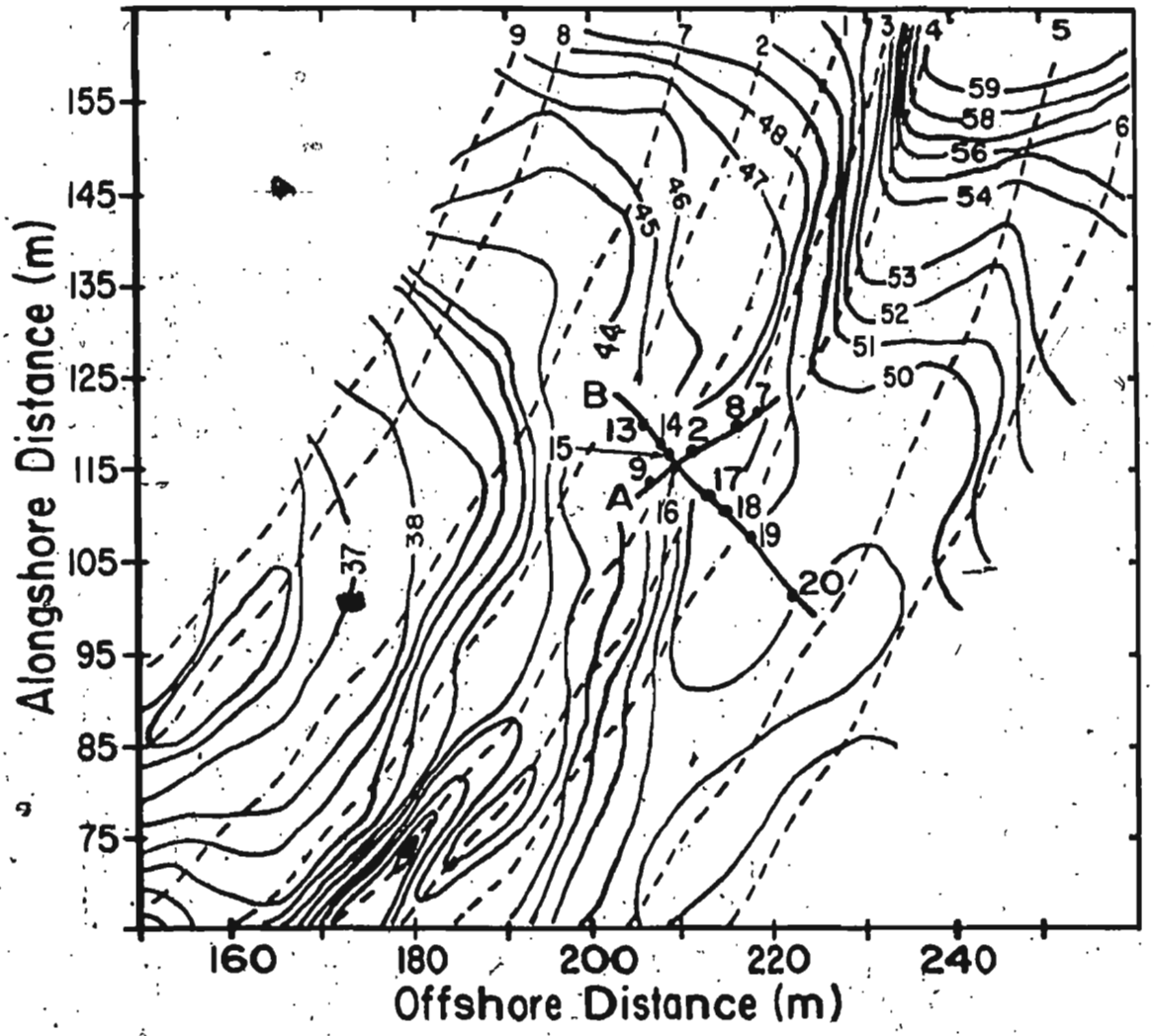

Figure 3.5 Detailed bathymetric chart of the vent area. The acoustic transects tracks are shown as the dotted lines. Two CTD transects labeled A and B are shown with the CTD cast positions.

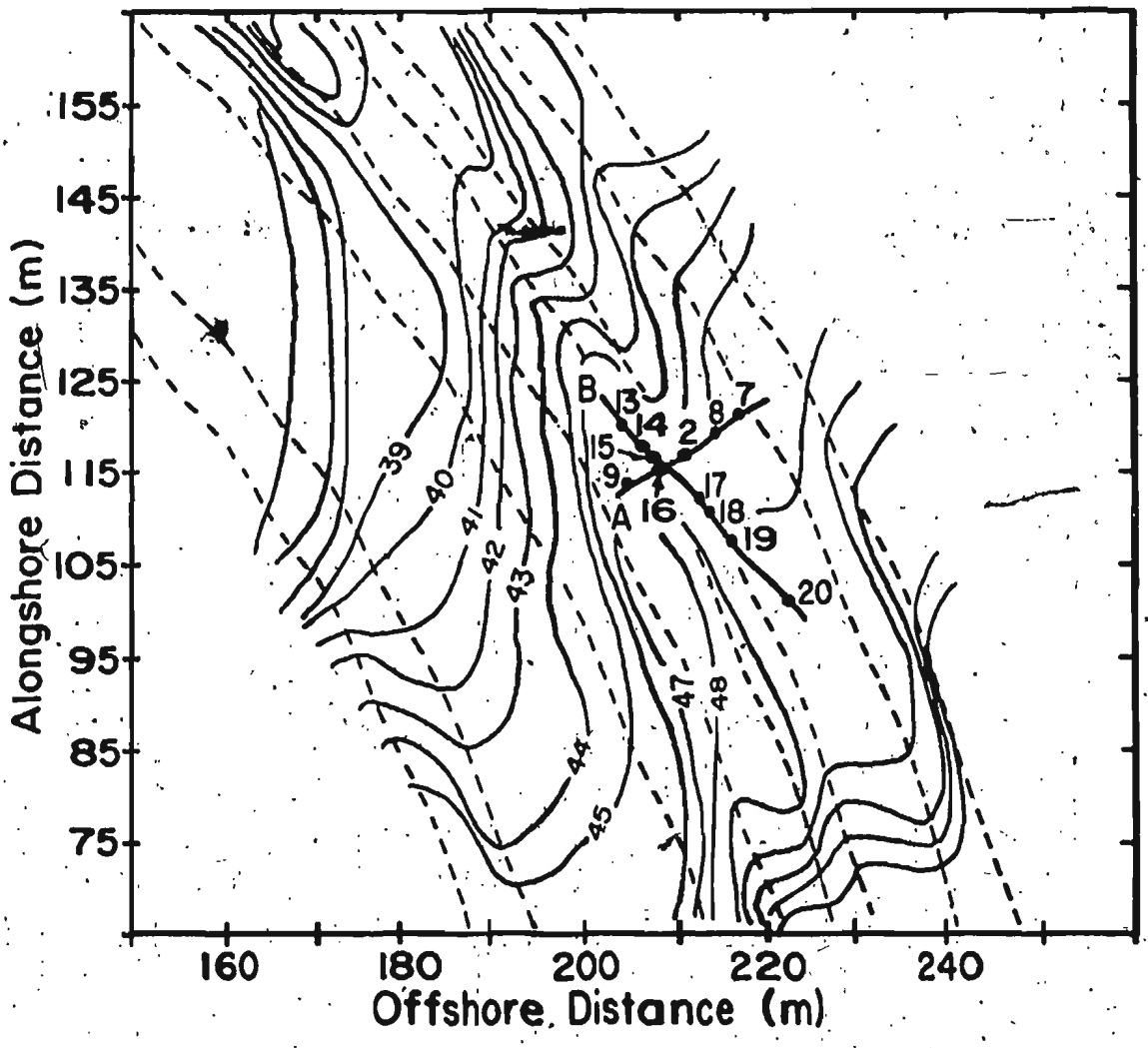

Figure 3.6 Detailed bathymetric chart of the vent area constructed from acoustic transects around the opposite transponder.

3.5 Acoustic images of the plume at fixed points

Figure 3.7 shows depth versus time false color images of the plume obtained while the launch was four-point moored over the vent. The echo from the CTD instrument package can be seen in these images as oblique traces during ascent and descent and a horizontal trace at 42 and 45 m depth in panels E and F where the CTD was held at constant depth for approximately 1 and 5 minutes respectively. Panel E is a depth versus time image of the plume corresponding to CTD number 2 in Figure 3.1. This image shows discrete scattering structures rising from the near bottom zone at approximately constant speed and then decelerating above 20 m depth. Somewhat higher ascent rates are evident below 37 m depth as indicated by the more nearly vertical scattering structures. Maximum ascent rates calculated from the slope of the straight line trajectories of these structures in the 20 to 37 m depth range are about 32 cm/sec. Panel F shows a similar image recorded at a lower receiver gain corresponding to CTD number 23 in Figure 3.1. These images were obtained one day after the ones shown in panels A and B in Figure 3.2. The previously mentioned increase in the maximum height of rise is clearly evident.

The scattering structures are intermittent with an overall near periodicity of about 0.5 minutes. The nature of the scattering structures is not fully understood, and is discussed later. The maximum height of rise is very sensitive to the vertical density gradient in the surrounding fluid. The oscillations in the plume height particularly in the image in panel F have periods of about 3 minutes. These periods are typical of internal waves which could cause changes in ambient stratification and account for the oscillatory behavior of the plume height.

Figure 3.7 Depth versus time false color images of the plume obtained while the launch was four-point moored over or to one side of the vent.

Panel E shows an acoustic image within the rising plume (CTD cast 2 in Figure 3.1).

Panel F shows another similar acoustic image within the rising plume (CTD cast 23 in Figure 3.1).

Panel G is an acoustic image of the spreading part of the plume (CTD cast 8 in Figure 3.1).

Panel H is similar to panel G at a slightly different location (CTD cast 9 in Figure 3.1).

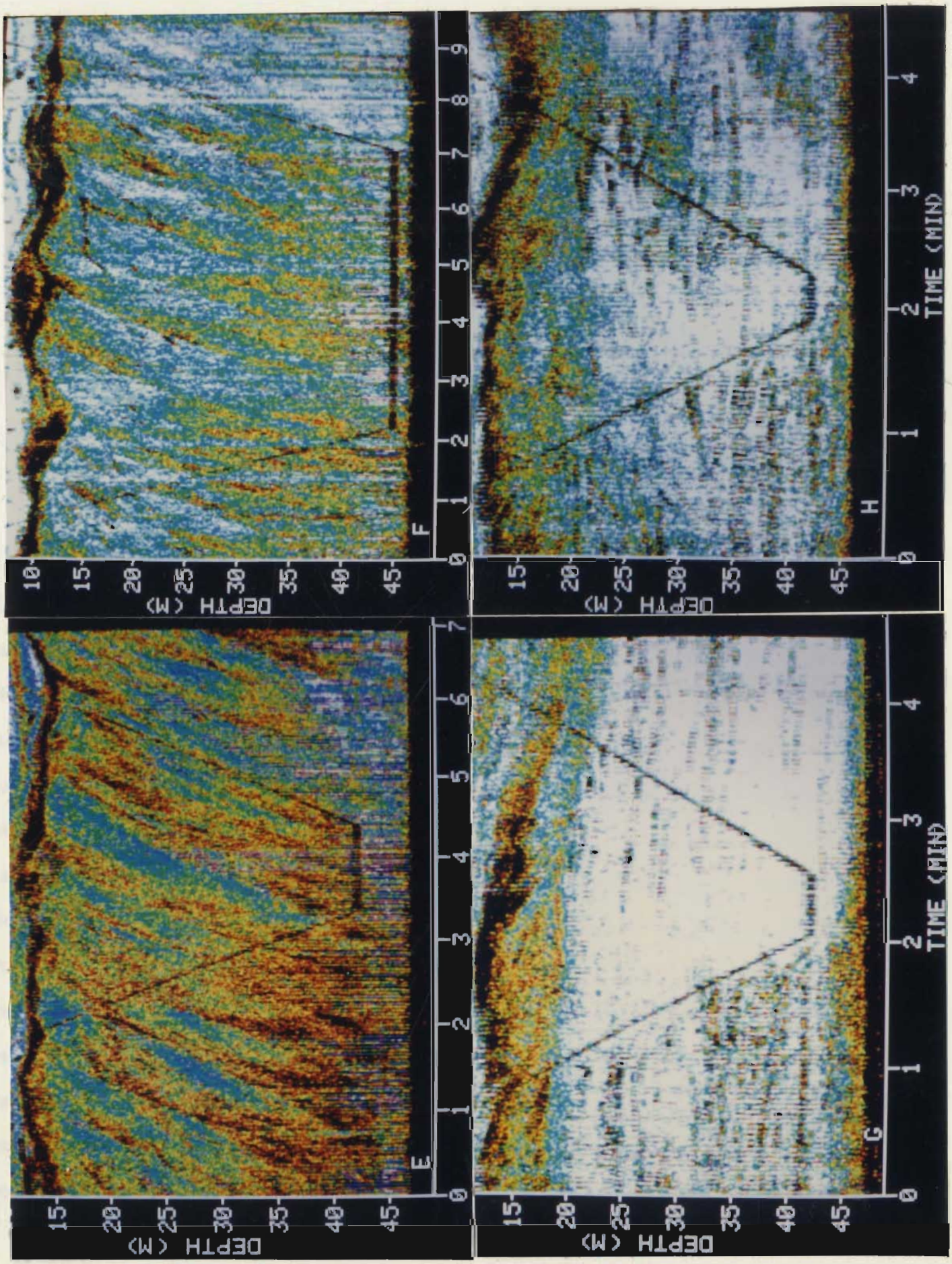
DEPTH (M)
TIME (MIN)
E
F
G
H

The false color acoustic images shown in panels G and H in Figure 3.7 were obtained with the launch four-point moored over the spreading plume. The descending CTD probe entered the top of the plume at about 12 m depth and emerged at about 20 m depth. The horizontally coherent structures typical of biological scatterers seen below 25 m in the first 1.5 minutes of the image in panel G disappear as the CTD descends, producing the relatively scatter free region after the CTD has passed. This is indicative of an avoidance response on the part of the organisms involved.

3.6 CTD measurements

Figures 3.8 to 3.10 are the temperature, salinity and σ_t profiles corresponding to cast numbers 23, 8 and 20, the positions of which are shown in Figure 3.1. The remaining CTD profiles are in Appendix A. Figures 3.8 and 3.9, cast numbers 23 and 8, correspond to the CTD's in acoustic images F and G. Figure 3.10 represents a CTD cast outside the spreading plume. Temperature, salinity and σ_t profiles corresponding to the CTD cast in acoustic image F in Figure 3.8 are typical of those taken in the rising plume. A brackish isothermal layer about 10 m thick with very high salinity and density gradients is present below the surface. Artificial spikes in the salinity and density profiles are seen at about 7.5 m depth. These spikes often occur in high gradient regions and are due to the time constant mismatch of the temperature and conductivity sensors and their physical separation. The top of the rising plume occurs at about 11 m depth and is marked by abrupt changes in all three profiles. The amplitude of fine structure variations increases with depth below this point. This fine structure is clearly associated with the scattering structures in acoustic image F. Minimum salinities are about 29.0 at 42 m depth. The fluctuations in temperature are smaller than

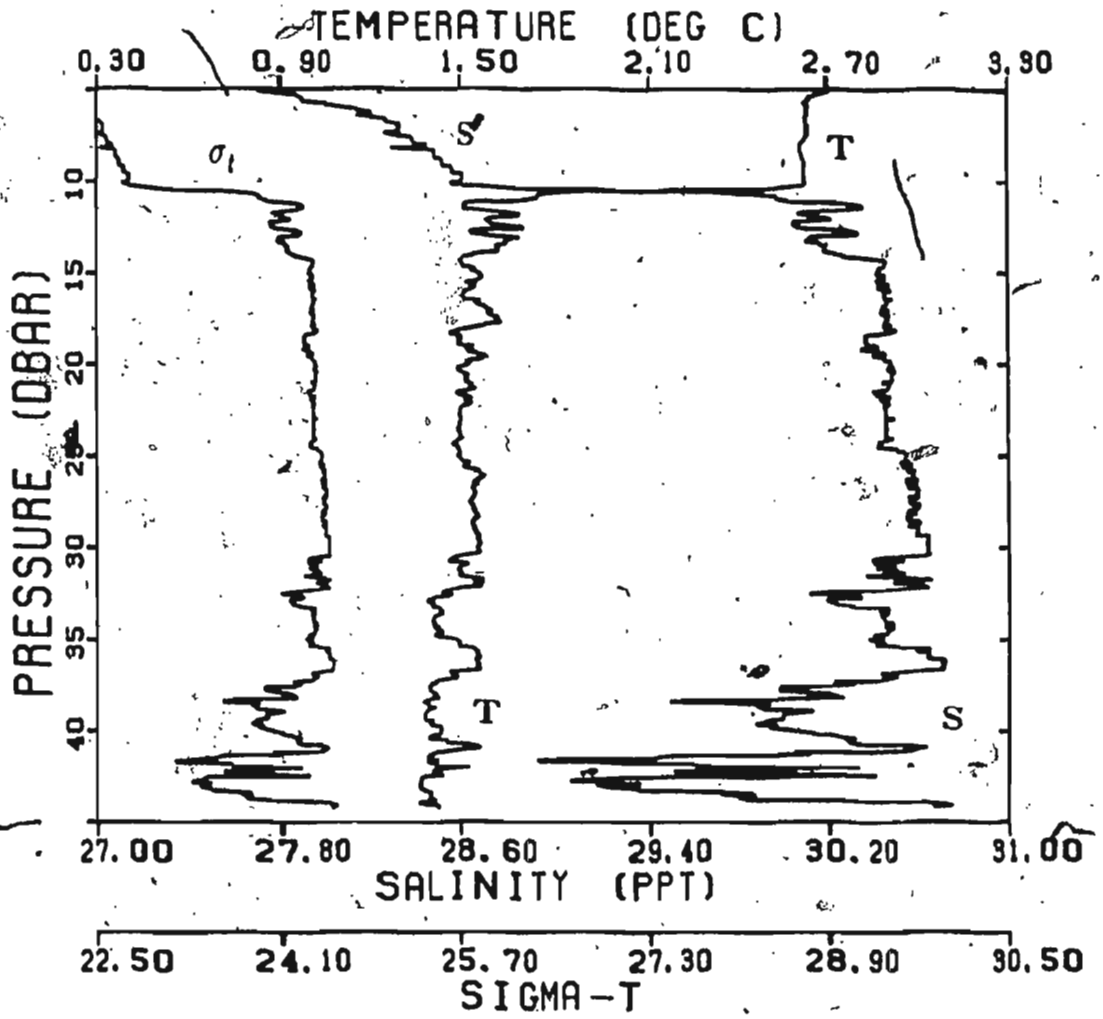

Figure 3.8 CTD profile through the rising plume corresponding to cast number 23 and acoustic image shown in panel F.

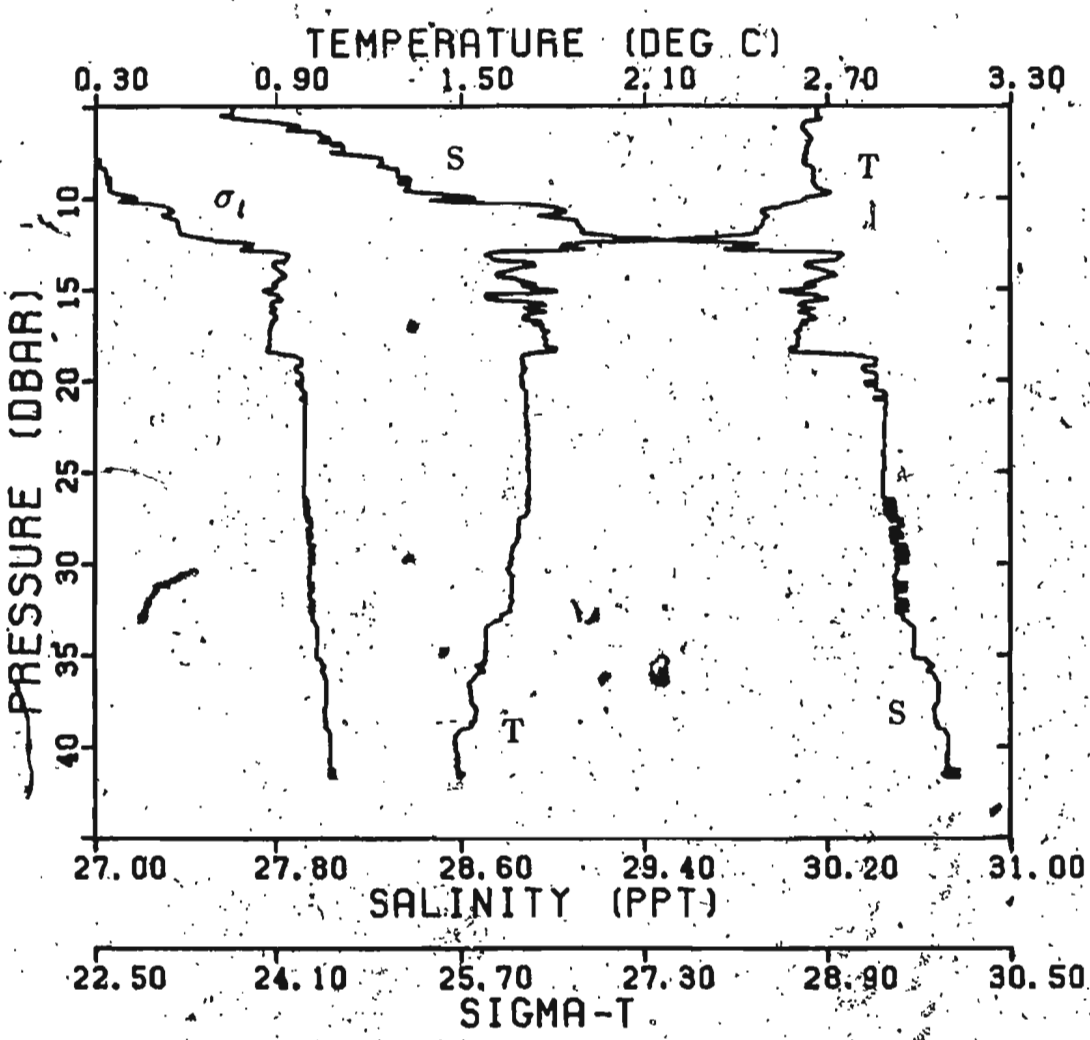

Figure 3.9 CTD profile through the spreading plume corresponding to cast number 8 and the acoustic image shown in panel G.

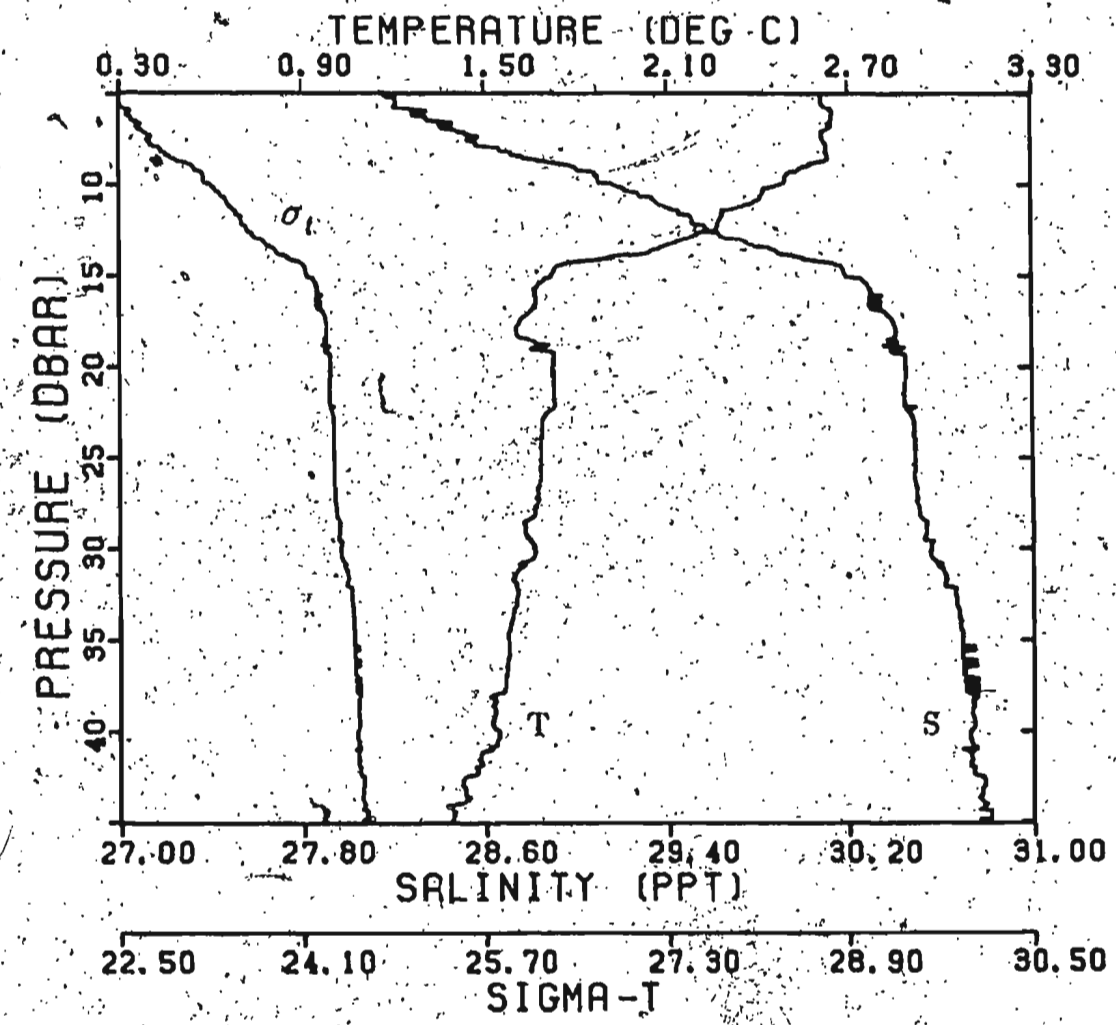

Figure 3.10 Ambient CTD profile obtained outside the spreading plume corresponding to cast number 20.

those in salinity, quite unlike the previous study in 1983 (Hay, 1984), when the reverse was true. This is discussed in Chapter 4.

The temperature, salinity and σ_t profiles corresponding to the CTD cast in acoustic image G are shown in Figure 3.9. These profiles are typical of those taken in the spreading plume. Again we have a brackish upper layer about 12 m thick with high salinity and density gradients. The temperature of this layer remains nearly constant except within the first 2 or 3 m of the surface. Artificial spiking is again evident in this region. Large amplitude variations in temperature and salinity occur where the CTD enters the spreading plume at 12 m depth. Outside the 12 to 20 m depth range the profiles are relatively smooth. The thickness of the spreading plume as indicated by the fluctuations in these profiles compared very well with the thickness observed in acoustic image G, about 8.0 m. Below 20 m depth the water column is relatively well mixed with small gradients in both temperature and salinity.

Figure 3.10 show an ambient CTD profile obtained away from the plume area. These profiles do not show the large amplitude statically unstable features that are evident within the plume.

3.7 Temperature, salinity and sigma-t sections

Twenty-three CTD profiles were obtained around the plume area. Two transects were selected from these CTD profiles. Station numbers 2, 7, 8 and 9 were selected for transect A. CTD station numbers 13 to 20 were selected in a direction roughly perpendicular to transect A across the plume for transect B (see Figures 3.5 and 3.1). Vertical sections of temperature, salinity and sigma-t are presented in Figures 3.11 to 3.13 corresponding to transect B. Transect A is shown in Appendix C. These contours were drawn after block averaging the

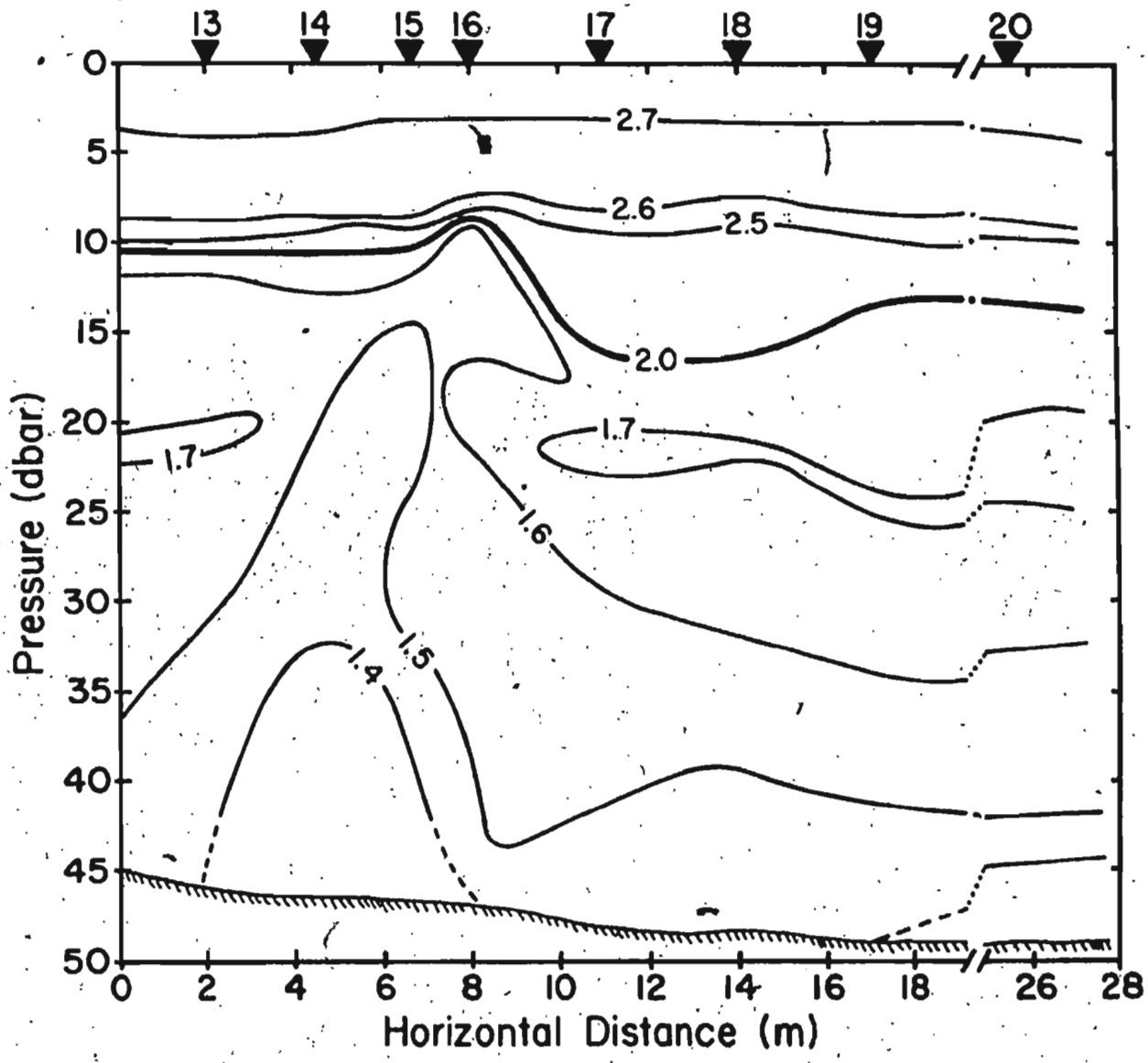

Figure 3.11 Temperature section from CTD transect B.

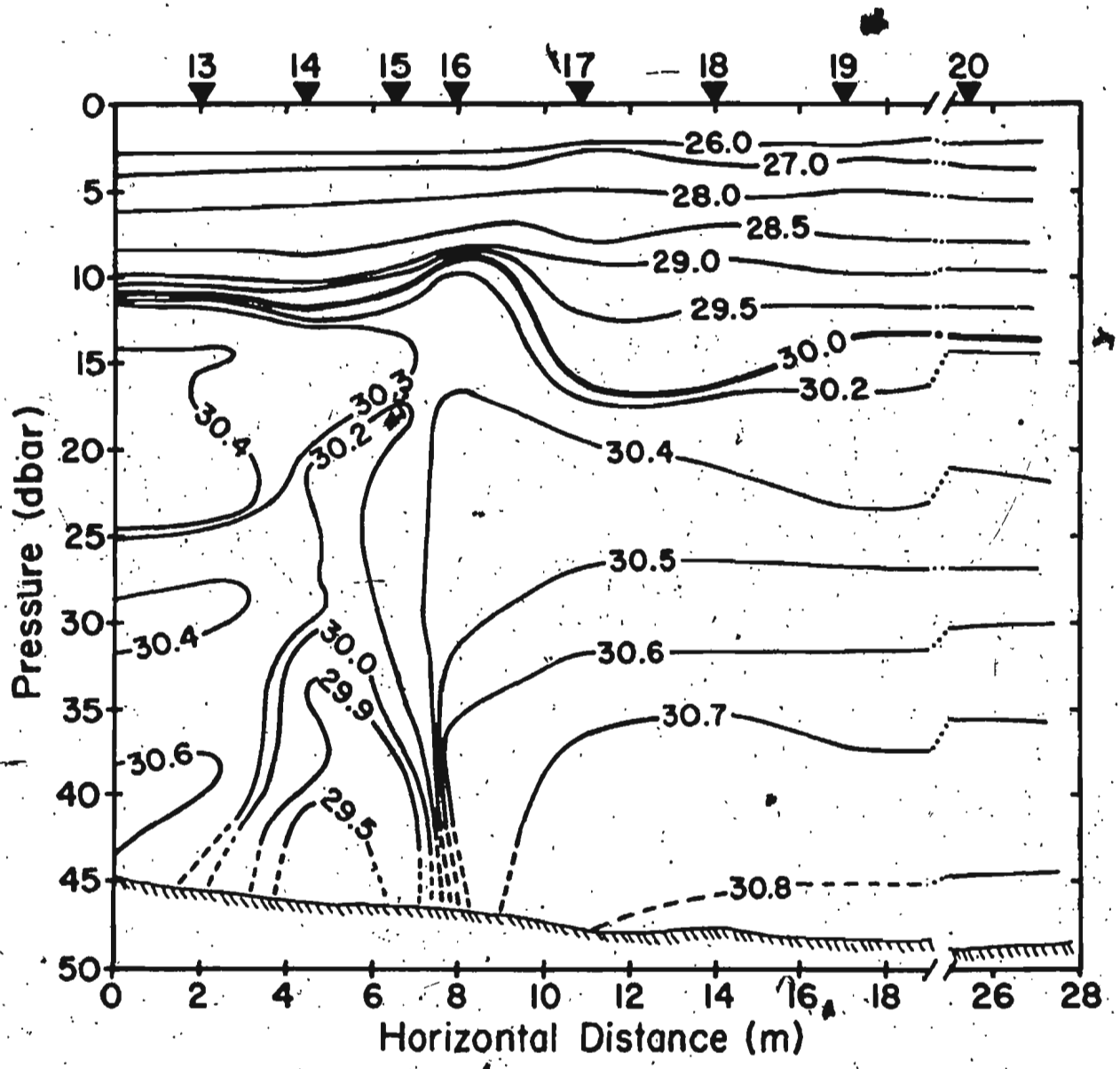

Figure 3.12 Salinity section from CTD transect B.

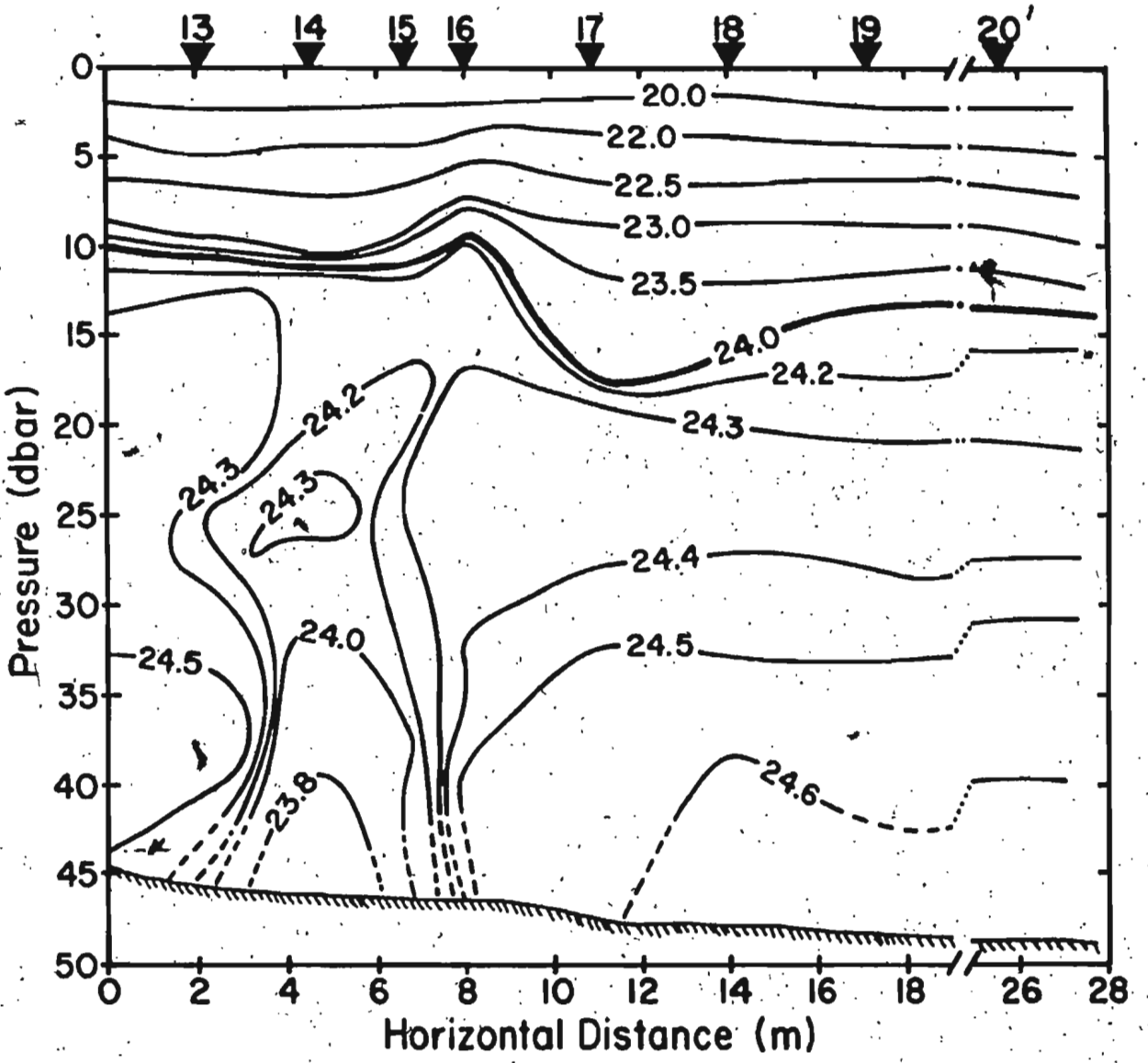

Figure 3.13 Sigma-t section from CTD transect B.

CTD profiles over approximately 0.5 m. The presence of the rising plume is clearly visible: the salinity at 40 m depth near the axis of the plume is less than 30.0 as compared to values greater than 30.7 just outside the plume area; and tongues of lower salinity water less than 30.1 are seen to be advected upwards. The top of the plume coincides with the base of the pycnocline at about 10 to 12 meters depth. Temperature and σ_t contours at 40 m depth are 1.4°C and 23.8 respectively.

These vertical sections indicate that the plume is about 6 to 8 m wide at 40 m depth. A horizontal profile obtained in 1983 through the plume at a depth of 33 m indicated a width of about 8 m (Hay, 1984). The vertical averaging has eliminated the variations in temperature and salinity making the spreading plume difficult to distinguish in these vertical CTD sections. This is quite unlike the acoustic images where the spreading plume is quite visible. This would seem to indicate that the acoustic backscatter is associated more with fluctuations in temperature and salinity than with mean values. This will be investigated further in Chapter 6.

3.8 Horizontal CTD time series

Figure 3.14 shows two time series of temperature, salinity and sigma-t acquired from the launch with the CTD suspended in the rising plume at 44 m and 21.5 m depth. Both show a high degree of intermittency particularly in salinity. Parcels of fresher plume water are seen to be advected past the CTD probe at 44 m depth. The average time interval between these features range from 0.2 to 0.5 minutes at 44 m depth, comparable to the interval between the rising scattering features seen in the acoustic images. The time series at 21.5 m depth exhibit temperature variations which are comparable in size to the salinity

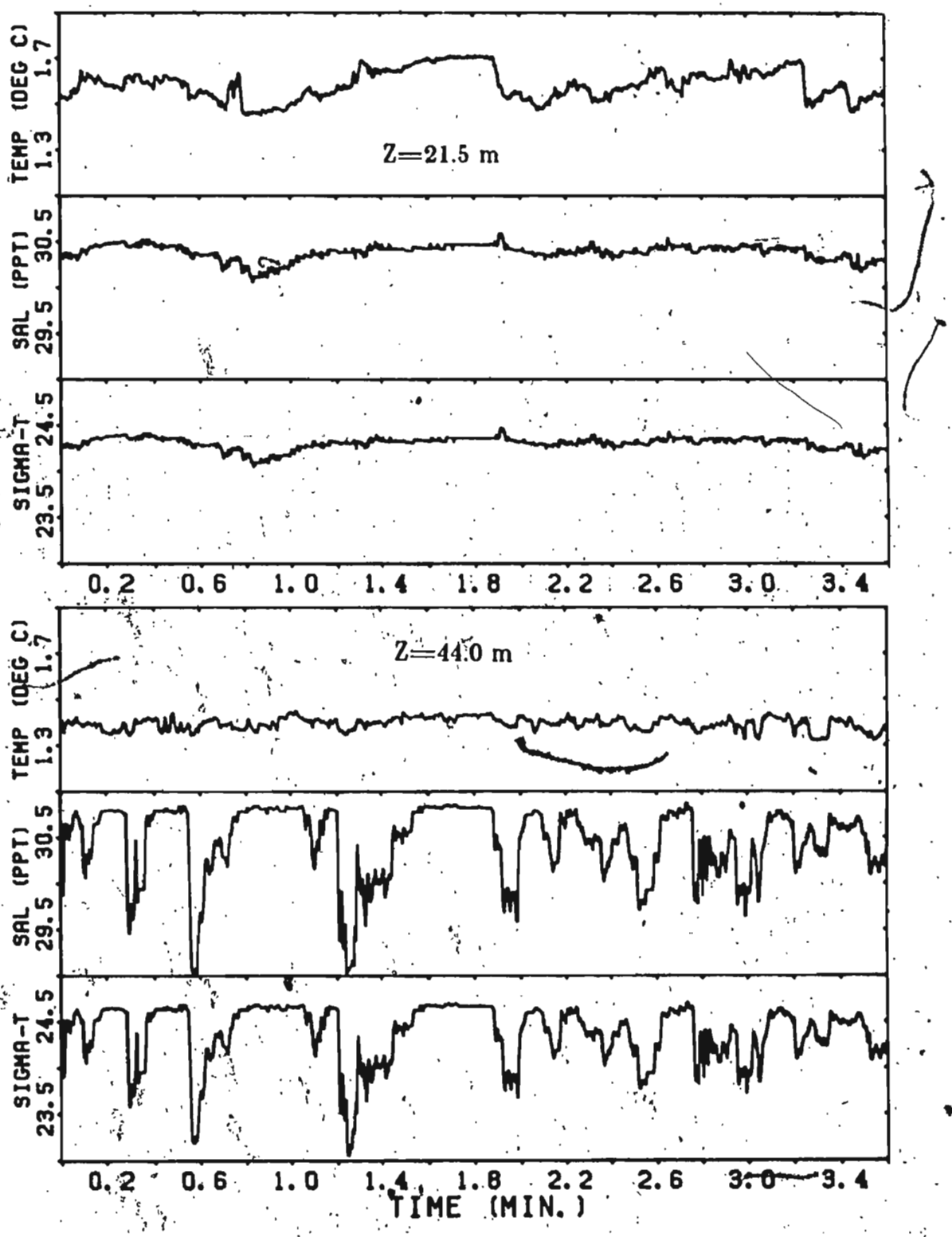

Figure 3.14 CTD time series obtained from the launch at depths of 44.0 and 21.5 m.

fluctuations, quite unlike the time series at the greater depth. This is probably due to the fact that more ambient water has been entrained into the rising plume by the time it reaches the shallower depth. Also in this time series the period of the larger variations are of the order of 2 minutes, much longer than those at 44 m depth. These measurements are different from the ones made in 1983 when the temperature fluctuations were much larger than the salinity fluctuations. It should be noted that CTD measurements made at constant depths are not expected to be as accurate as ones made from descending probes. This is particularly true of salinity since inadequate flushing of the conductivity cell is likely. However this is not expected to be a problem in the rising plume since the flow speed is sufficient to flush the cell.

3.9 Submersible observations

Observations in the vent area from the submersible included water property measurements, water samples, current measurements and photographic, video and visual observations. The panels in Figure 3.15 are 35 mm photographs of the vent area. The photograph in Panel A was taken with the Photosea 2000 camera and shows the vent area. The main source of discharge water flows up around the large rectangular rock which has dimensions of about 1.0 m by 2.0 m. This discharge mixture converges and combines with several other smaller discharge plumes to form one large plume of brackish water approximately 1.0 m above the bottom. The horizontal extent of this plume is between 2.0 and 4.0 m. Panels B, C and D were taken from within the submersible. The blurring effect seen in these three panels is due to the large variations in the optical refractive index caused by the mixing of the freshwater and the ambient water. The plume-like behavior of the flow is evident in these photographs. The freshwater is seen to

Figure 3.15 Thirty-five mm photographs of the vent area taken from the submersible PISCES IV.

Panel A was taken with the Photosea 2000 camera, it shows the large rectangular rock covering the vent area. This rock was about 1.0 m wide by 2.0 m long.

Panel B and C were taken from within the submersible, they show the colored anemones, kelp and other biological organisms found around the vent area. The blurring effect caused by the freshwater discharge is easily seen. These anemones are about 10.0 cm across.

Panel D shows a separate plume of freshwater approximately 2.0 m from the main source.

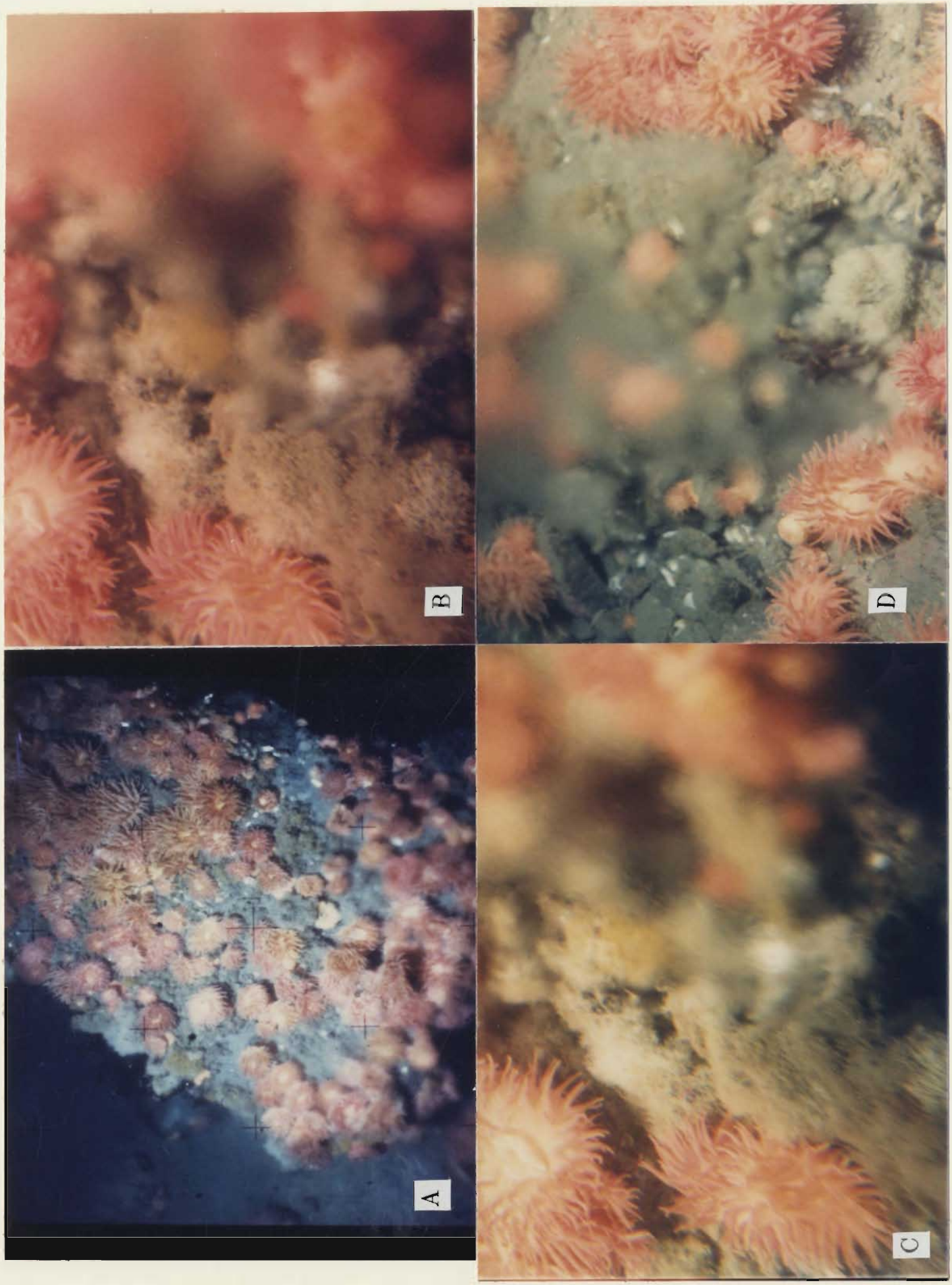
B
D
A
C

seep from the bottom with virtually no initial momentum. All panels show the brilliantly colored anemones, kelp and other biological organisms found on the rocks bathed in the discharge plume water. Elsewhere, away from the vent the benthic fauna are sparse. Panel D shows a separate plume of discharge water flowing from the bottom about 2.0 m from the main source. These observations indicate that the submarine spring system supports a biological community which is highly productive relative to the immediate vicinity.

A total of 15 water samples for chemical analysis were obtained around the vent area. These samples were obtained with a hose attached to the remote manipulator arm of the submersible and connected to a pump. The sample jars were flushed before a sample was retained. The salinities of these samples were determined using a Guildline model 8400 Laboratory Salinometer. Salinities ranged from 17 to 29 for various locations in the discharge water and 30.9 to 31.6 a short distance from the actual discharge, consistent with the CTD measurements made from the launch (Figure 3.10).

Figure 3.16 shows a typical time series of temperature, salinity and sigma-t obtained from PISCES with the probe over the vent at about 1.0 m above the bottom. Appendix B shows additional time series obtained near the vent. The mean temperature and salinity from this time series is 0.8°C and 25.0 respectively. Note the large fluctuations, particularly in salinity. Minimum salinities of less than 20 are present. These minimum salinities are comparable to the value of 17 determined from water samples taken a few centimeters above the bottom. Again we see that the fluctuations in salinity are larger than those in temperature. The mean time interval between these fluctuations is again of the order of 0.5 minutes, comparable to Figure 3.14 at 44 m depth.

Time series of horizontal and vertical velocity components obtained from the

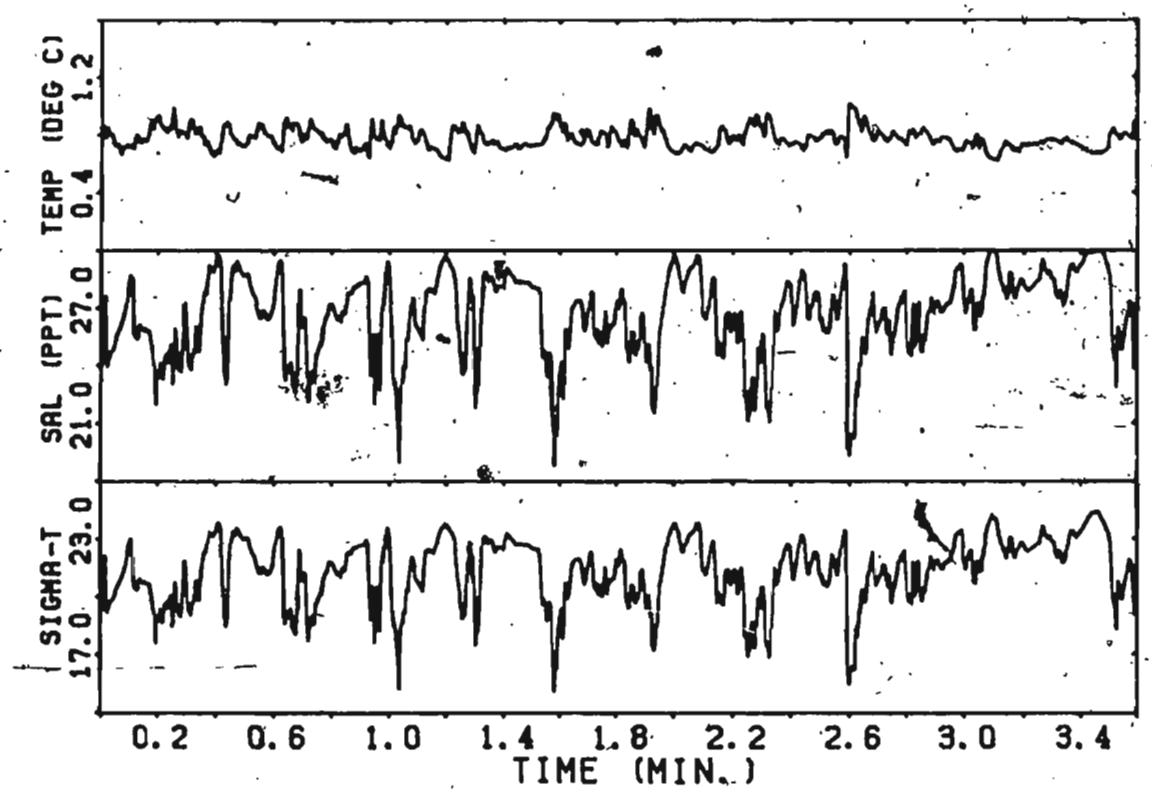

Figure 3.16 Typical CTD time series obtained at the vent from the submersible PISCES IV at a depth of 47.0 m.

submersible are shown in Figure 3.17. Appendix D shows additional time series. The Neil Brown acoustic current meter mounted on the remote manipulator arm of the submersible was oriented to give vertical speeds in the x-component channel and horizontal speeds in the y channel of the current meter. The measurements were made at the vent location about 1.0 m above the bottom. The horizontal components seen in Figure 3.17 fluctuate around zero. Fluctuations of the order of 10 cm/sec are observed, with an average of about 4.0 cm/sec. Any movement of the submersible during the measurements would contribute to these fluctuations. The vertical component fluctuates around 30 cm/sec after the current meter probe was inserted into the rising plume at 0.2 minutes relative time. These measured speeds compare very well to the near bottom value of 32 cm/sec calculated from the acoustic images.

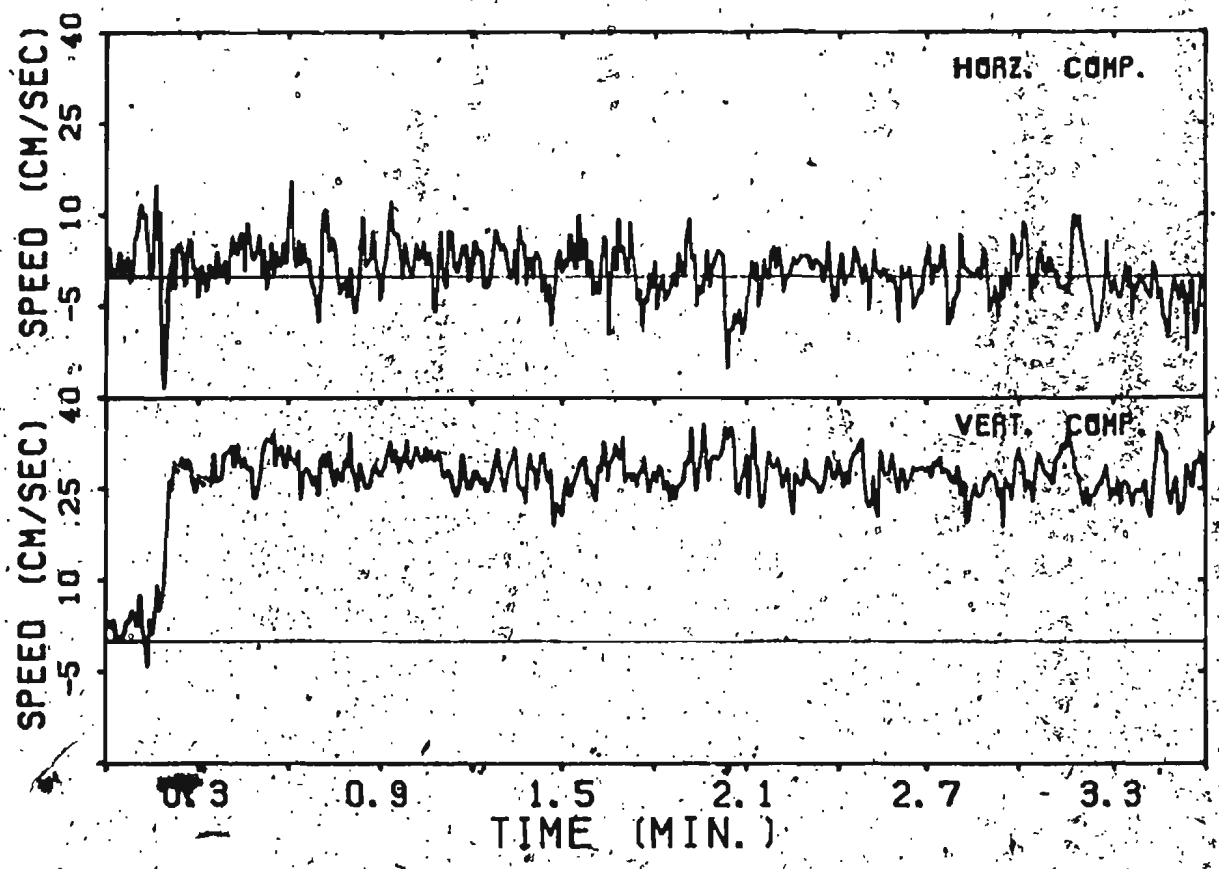

Figure 3:17 Horizontal and vertical velocities in the rising plume obtained from the submersible PISCES IV at the vent about 1 m from the bottom.

CHAPTER 4 OBSERVATIONS OF THE AMBIENT ENVIRONMENT

Measurements of ambient conditions were made with the anemometer and current meter mooring, the locations of which are shown in Figure 1.2. In addition ambient currents, water temperatures and salinities were made during the experiment from the submersible and the launch. The direction conventions for both winds and currents are equivalent for the data presented in this chapter; that is, axial components of wind and current are positive down-fjord along 32 degrees true; transverse components are positive cross-fjord along 302 degrees true.

4.1 Anemometer and moored current meter measurements

Figure 4.1 shows the ambient currents and temperatures for the period of the plume observations. The dominant tidal constituent in this fjord is semidiurnal with a low but unknown range. However these currents do not appear to be tidal. The position of the current meter at the head of the fjord resulted in a measurement of both an axial and transverse component which were approximately equal in magnitude. Current velocities were generally less than 5 cm/sec during the plume observations. Figure 4.2 shows the wind speed, direction and the axial and transverse wind components for the same period. The approxi-

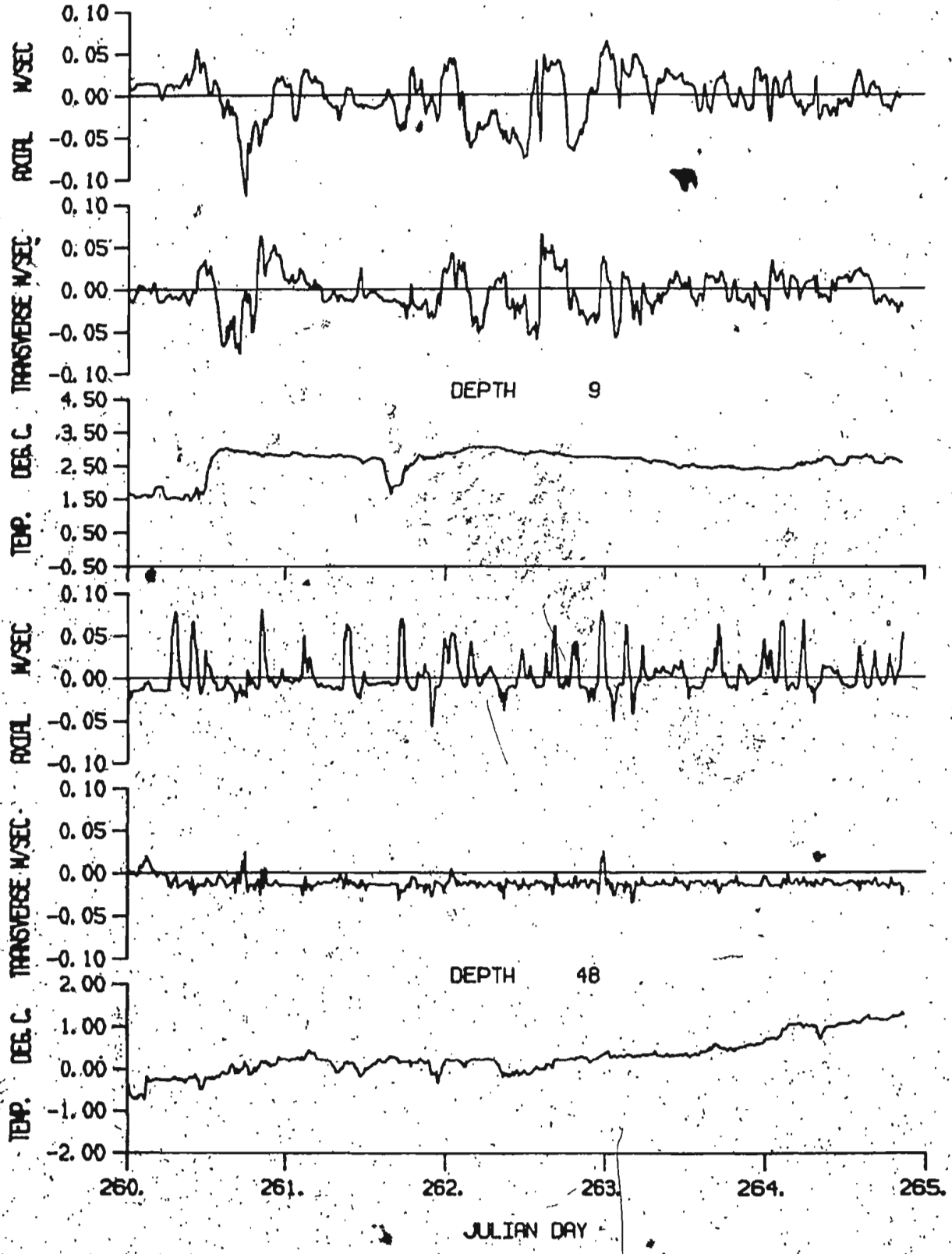

Figure 4.1 Time series of axial and transverse currents and temperature at 9 m and 48 m depth for the period of the plume survey.

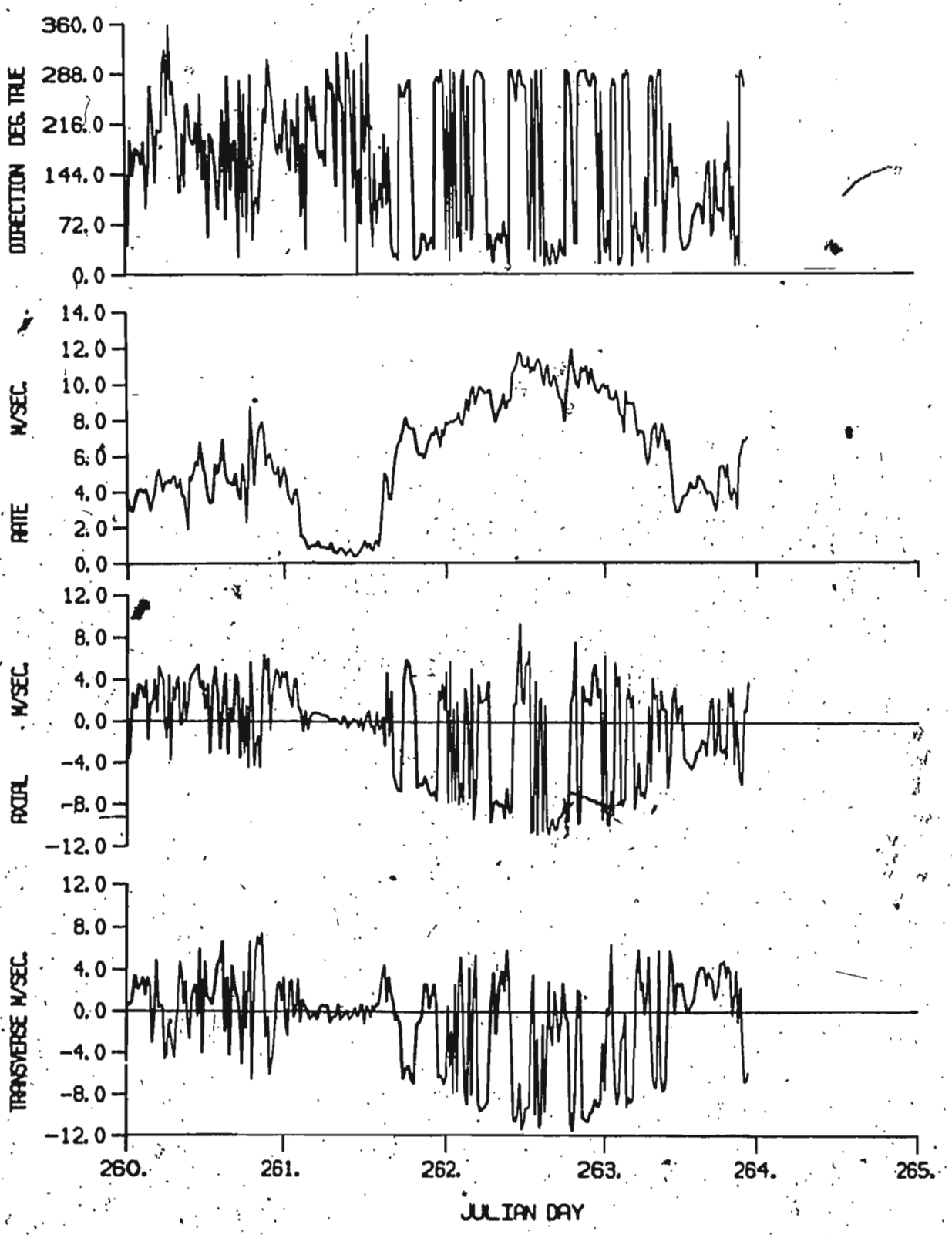

Figure 4.2 Wind speed, direction and the axial and transverse wind components for the period of the plume observations.

mately 270 degree fluctuations in the direction occur at about 2.0 hour intervals while the winds from the ship's log for this period were from a NNE direction. The ship observations and experience on site place the direction record in doubt. The intermittency in the direction of these winds is probably due to either a malfunctioning compass or topographic effects on the wind near the anemometer location. Some confidence however can be put in the measured wind speeds. The maximum wind speed measured by the anemometer was approximately 12.0 m/sec compared to a speed of 12 to 18 m/sec obtained from the ship's log. By Julian day 264 the up-inlet wind speed had dropped off considerably, which is consistent with what was actually observed. These strong up-inlet winds during the plume experiment did not appear to have initiated any strong currents, at least not during the same period.

Figure 4.3 shows the axial and transverse currents and temperatures for the period of September 1 to 22 1985 at 9 and 48 m depth. Filtered axial and transverse components for this period are shown in Appendix D. The filter had a cutoff period of 4.0 hours. There are two prominent features in these records. One is the warming trend in the latter part of the record from the deep instrument, the other is the several abrupt 0.0 to 3.0°C decreases in near surface temperature which persisted for about a day and then abruptly reverted to previous values.

Figure 4.4 shows the axial and transverse, unfiltered and filtered wind data for the same period. While it is tempting and probably reasonable to ascribe the observed temperature changes to wind forcing, such a relationship is not obvious in the data. This is likely due to the apparent problem with the anemometer. However the strong up-inlet winds experienced from day 262 to 264 clearly did result in a further increase in the bottom water temperature from 0.0 to 1.0°C This wind-induced change in the water temperatures particularly at depth

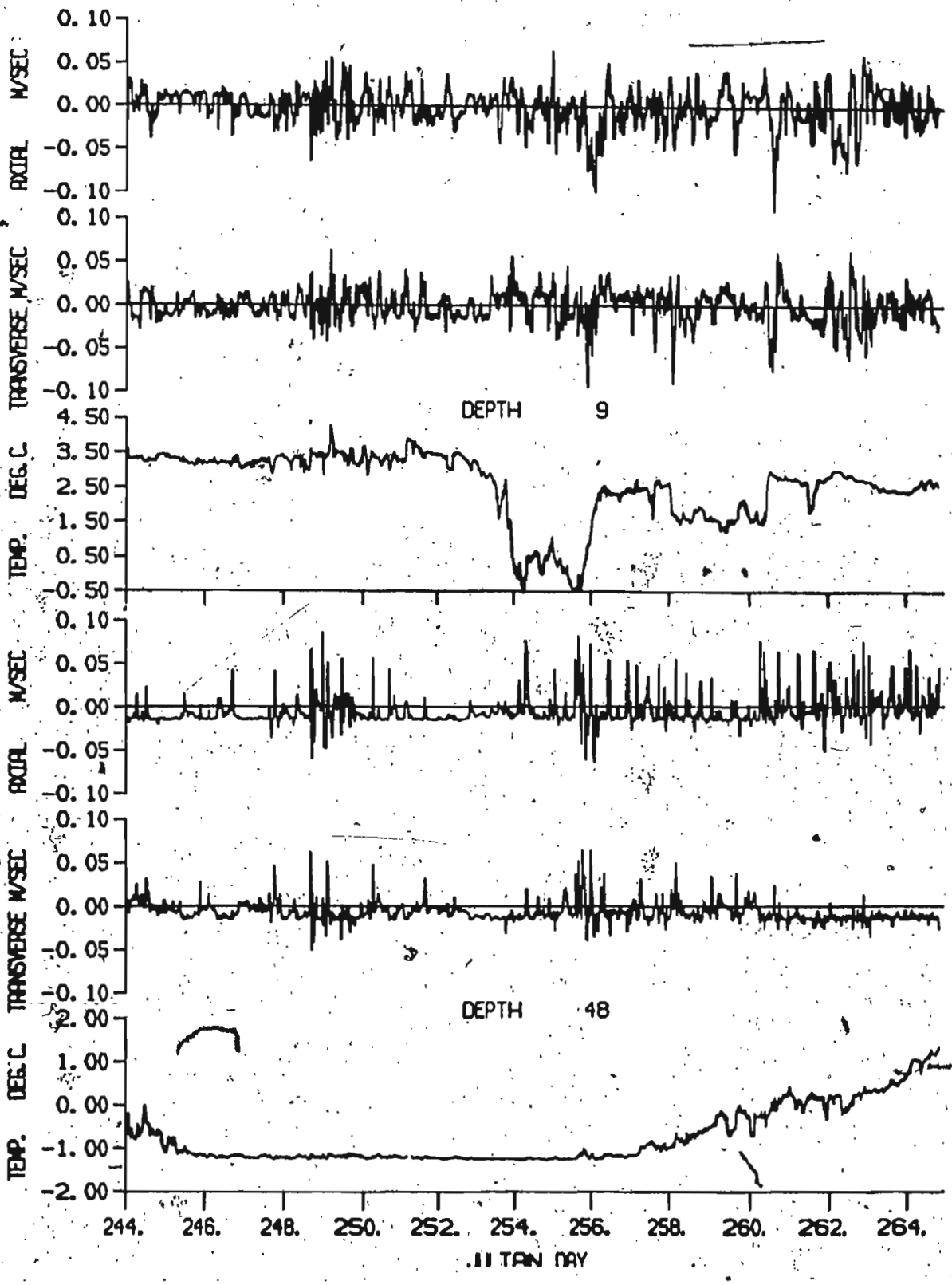

Figure 4.3 Time series of axial and transverse currents and temperature at 9 m and 48 m depth for September 1985.

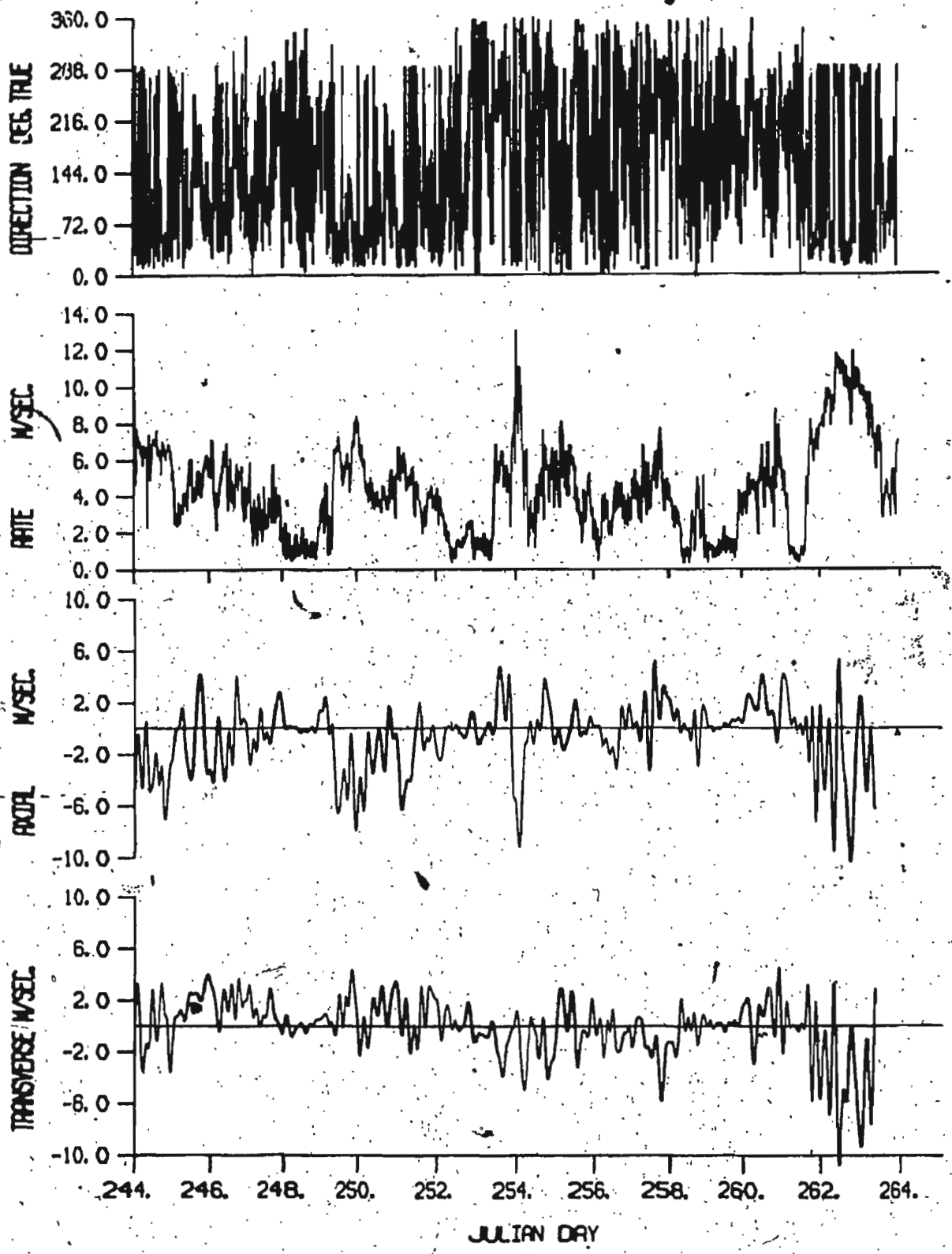

Figure 4.4 Unfiltered and filtered wind data for September 1985.

resulted in a decrease in the temperature difference between the ambient and plume water. In 1983 when conditions were calm the ambient water was about one-half a degree cooler than the discharge water. As a result the fluctuations in temperature in 1983 were much larger than in 1985.

4.2 Submersible and launch observations

The ambient currents, temperatures and salinities were also measured from the submersible near the vent location at about 47 m depth. Ambient CTD profiles were obtained from the launch a short distance from the plume. The current and CTD measurements were obtained with the DRCM-2 acoustic current meter and the Guildline CTD as discussed previously.

The ambient currents obtained near the vent were very small during the plume observations. Time series of horizontal and vertical currents shown in Appendix D has fluctuations of the order of 1 to 5 cm/sec. These measurements were made on September 21 at 1115 and 1149 local time, about 8 hours before the acoustic images in Figure 3.2 were obtained.

Time series of temperature and salinity also obtained near the vent from the submersible range from 31.2 to 31.7 and 0.4 to 0.7 °C respectively. These temperature measurements agree quite well with those made at 48 m depth by the moored current meter. The CTD profile shown in Figure 3.10 was obtained from the launch about 30 m from the plume on September 22 one day after the acoustic sounding transects were conducted. The strong up-inlet winds had subsided somewhat by this time. The fresh upper layer seen in this profile was probably thicker by about 5 m on September 21 as indicated by the differences in the maximum height of rise of the plume on the two days.

CHAPTER 5 PLUME MODELS

5.1 Background

A simple jet is the turbulent flow generated by a continuous source of momentum. A simple plume is the turbulent flow generated by a continuous source of buoyancy such as caused by a steady release of heat. A turbulent flow that is generated by a continuous source of buoyancy and also of initial momentum is referred to as a buoyant jet or forced plume (Fan, 1967). A simple plume has no initial momentum, but due to the action of buoyancy the momentum increases with height. Plumes increase in width with height through the process of entrainment of ambient fluid by large scale eddies of the turbulence. In a stably stratified fluid plumes will not rise indefinitely since they will eventually become as dense as the ambient fluid. In this case the plume reaches a maximum height of rise after which the turbulence decays rapidly as it spreads horizontally.

There are three basic methods which have been used to obtain solutions for the behavior of jets and plumes. One method consists of specifying relations for the turbulent transport terms in the conservation equations for mass, momentum and tracers. Another approach has been to solve for the mean flow properties from dimensional asymptotic analysis (Fischer et al., 1979). This method tries to reduce the number of independent variables characterizing the flow. The third method is the so-called integral method of Morton, Taylor and Turner (1956). This approach consists of specifying the shape of the concentration, density and

velocity profiles and integrating the conservation equations across a section normal to the plume trajectory. Several other simplifying assumptions are needed to find the solutions. This has been the most widely used and accepted method. A number of numerical models have been written to solve the general conservation equations for buoyant jets and plumes in density stratified ambients using the integral method.

5.2 Dimensional analysis without stratification

The number of independent variables that must be considered can be reduced by considering the effects of momentum and buoyancy separately. The analysis here considers vertically discharged flows in a linearly stratified ambient fluid. The flow is considered to be fully turbulent so molecular viscosity can be neglected. The Boussinesq approximation is used, that is the density differences are important only in combination with gravity.

Close to the source plumes are usually controlled entirely by the initial conditions: exit geometry, velocity, density differences and the ambient flow. The three most important parameters governing the plume motion can be defined as follows (Fischer et al., 1979):

$$Q = \frac{1}{4}\pi D^2 U_0 \tag{5.1}$$

$$M = \frac{1}{4}\pi D^2 U_0^2 \tag{5.2}$$

$$B = g\frac{\Delta\rho}{\rho_0}Q \tag{5.3}$$

Where Q, M and B are the volume, momentum and buoyancy flux, D is the plume diameter, U_0 the outflow velocity and $\Delta\rho$ is the density difference between

the ambient and discharge fluids. The dimensions of these three variables are

$$[Q] = \frac{L^3}{T} \tag{5.4}$$

$$[M] = \frac{L^4}{T^2} \tag{5.5}$$

$$[B] = \frac{L^4}{T^3} \tag{5.6}$$

Where L and T denote length and time dimensions respectively. These variables can be combined into various length scales that characterize a particular aspect of the flow.

The buoyant plume under study here is surrounded by a stratified ambient fluid. We therefore consider length scales associated with the buoyant plume variables and the square of the buoyancy frequency,

$$N^2 = \frac{-g}{\rho_0}\frac{d\rho}{dz} \tag{5.7}$$

The quantity $\left[\frac{1}{\rho_0}\frac{d\rho}{dz}\right]^{-1}$ is the characteristic length scale associated with the stratification.

We will now consider a point source of specific buoyancy flux B, directed vertically upwards. The effect of this buoyancy flux and associated momentum flux will be to carry buoyant water upwards where the density difference and hence buoyancy becomes smaller. Therefore a terminal height of rise must exist in the fluid provided of course the total fluid depth is sufficiently large. In the asymptotic limit, that is as $M \to 0$, the buoyant jet can be considered as behaving like a simple plume with specific buoyancy flux B. In this case the terminal height of rise will depend only on N^2 and B, and is given by

$$h_B = C_1 \frac{B^{1/4}}{(N^2)^{3/8}} \tag{5.8}$$

the coefficient of proportionality C_1 was determined from experimental data by Morton et al. (1956) to be about 3.8. The length scale h_B is the total distance required for the density stratification to remove the initial buoyancy from the plume.

Similarly if we consider the other asymptotic limit as $B \to 0$ the flow will approximate a simple momentum jet and the terminal height of rise in this case is given by

$$h_M = C_1 \left[\frac{M}{(N^2}\right]^{1/4} \tag{5.9}$$

and has a similar interpretation to h_B. The ratio of these two length scales $\frac{h_M}{h_B}$ raised to the eighth power can be considered to be the defining parameter for buoyant jets with density stratification. It is given by

$$S = \frac{M^2 N^2}{B^2} \tag{5.10}$$

5.3 Buoyant plume calculations

5.3.1 Discharge Conditions

Observations from the submersible indicate a large irregular discharge region at least 2 m in horizontal extent with very little initial momentum. Obviously this is not a good candidate to be modeled by simple round jet dynamics in the initial region. This suggests that the flow will be plume-like a short distance from the actual discharge point.

The volume rate of discharge will be calculated as the sum of the freshwater discharge and the salt water entrained into the discharge in the prodelta and near the bottom. Both types of entrainment must exist given the porous nature of the delta sediments and the cobbly material and large rocks around the vent area. Furthermore we were not able to obtained a bottle sample of salinity less than 17 even at a few centimeters from the bottom. The initial salinity of the discharge mixture can then be expressed in the form

$$S_0 = \frac{S_e \rho_e Q_e}{\rho_f Q_f + \rho_e Q_e} \tag{5.11}$$

where S_e, ρ_e and Q_e are the salinity, density and discharge rate of the entrained water, and ρ_f and Q_f are the density and discharge rate of the freshwater. To a very good approximation $\rho_f \approx \rho_e$ therefore

$$S_0 = \frac{S_e Q_e}{Q_f + Q_e} \tag{5.12}$$

The total discharge rate can now be written as

$$Q = Q_f + \frac{S_0 Q_f}{[S_e - S_0]} \tag{5.13}$$

The effective diameter of the discharge region was calculated from the total discharge rate given by Eq. (5.13) and the initial discharge velocity. The discharge rate from any round source is given by

$$Q = \pi \left[\frac{D}{2}\right]^2 U_0 \tag{5.14}$$

Figure 5.1 shows total discharge rate Q and diameter versus initial salinity as calculated from Eq. (5.13) and (5.14). The freshwater discharge rate was fixed at 0.10 m^3/sec, within the range estimated from the drop in the water level of the lake. The entrained salinity used was 31.6 which represents the mean salinity

obtained close to the bottom a short distance from the plume. The initial velocity was set equal to 30 cm/sec from Figure 3.17. Choosing a discharge salinity of 28.0 as an overall average from Figure 3.16 of section 3.0 we see from Figure 5.1 a calculated diameter of approximately 2.0 m, roughly corresponding to the observed horizontal extent of the discharge region. This corresponds to a total combined discharge of entrained and freshwater of approximately 1.02 m^3/sec.

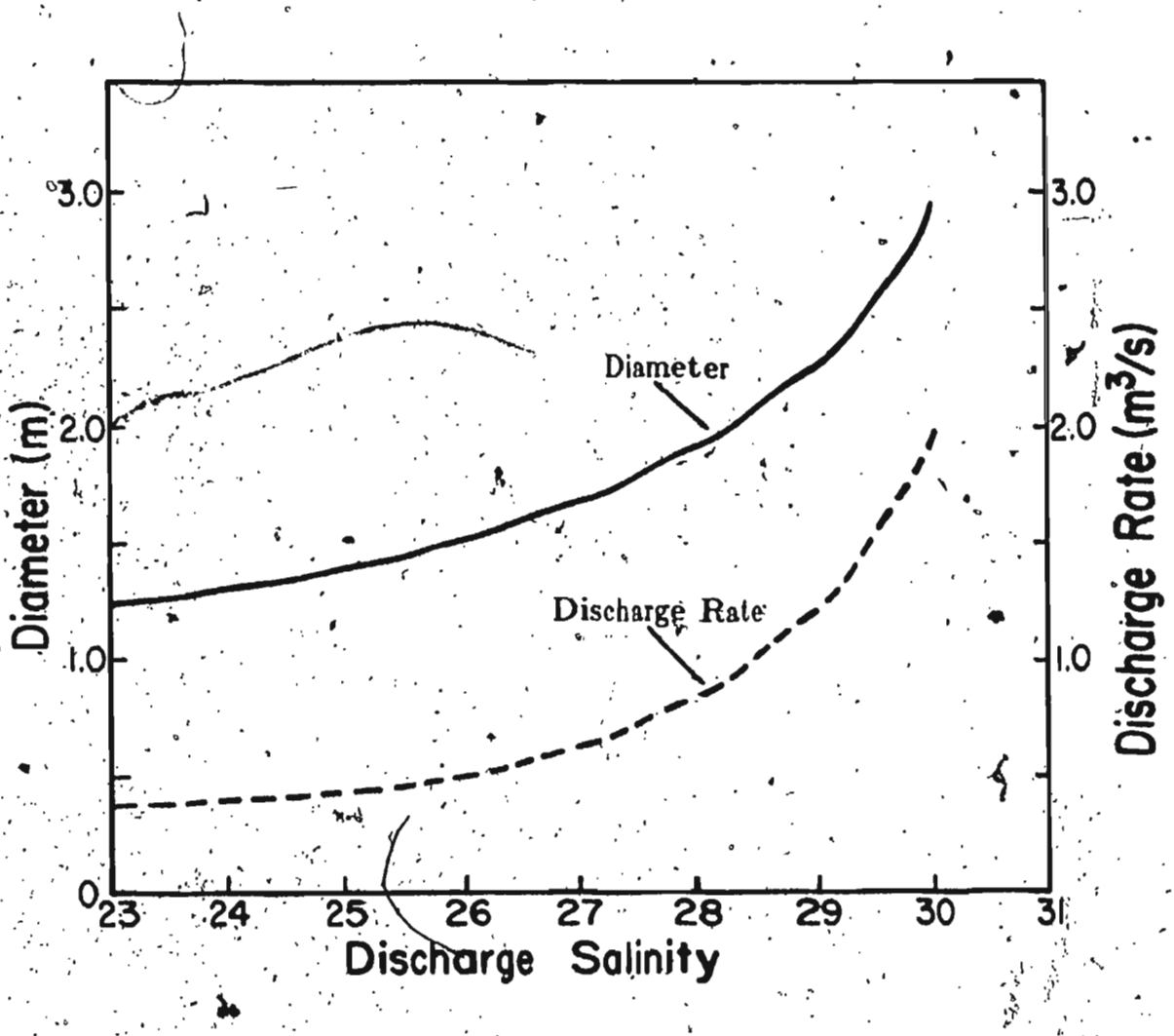

Figure 5.1 Discharge rate and diameter versus initial salinity

Ambient density profiles measured in 1983 and 1985 are shown in Figure 5.2. The profile labeled a corresponds to 1983, and profile b represents a linear fit. This linear fit also approximates the 1985 profile labeled c below the pycnoline. The buoyancy frequency of the linear density profile is 9.79×10^{-3}sec^{-1}. The ambient density at 46 m depth from this linear fit is 1025.28 kg/m^3. From Eq (5.10) the stratification parameter can be written as

$$\hat{S} = \frac{\rho_0^2 U_0^2 N^2}{(g\,\Delta\rho)^2} \tag{5.15}$$

Taking a typical discharge salinity of 28 and an initial discharge velocity of 30 cm/sec and using N from the linear ambient density profile we get $\hat{S}$ equal to 0.012. Since $\hat{S} \ll 1$ we conclude that the plume is dominated by buoyancy at about one meter above bottom. This confirms the visual observations made from the submersible.

5.3.2. Terminal heights of rise

The terminal height of rise for a buoyant plume, Eq. (5.8), can be expressed in the form

$$h_B = 3.8\left[\pi g \frac{U_0}{4}\frac{\Delta\rho}{\rho_0}\right]^{1/4} D^{1/2} N^{-3/4} \tag{5.16}$$

Terminal heights of rise h_B for a range of salinities from 24 to 30 are summarized in Table 3. The density gradient used in these calculations was the linear fit to the 1983 ambient density profile. The initial discharge velocity and diameter were 0.3 m/sec and 2.0 m as above. We see that the terminal heights of rise increase from 38.6 to 59.4 m. As the initial salinity decreases the buoyancy flux increases and hence the increase in the maximum height of rise. The maximum heights of rise from the sounder records of 1983 range from 37 to 41 m and 34 to 36 m for

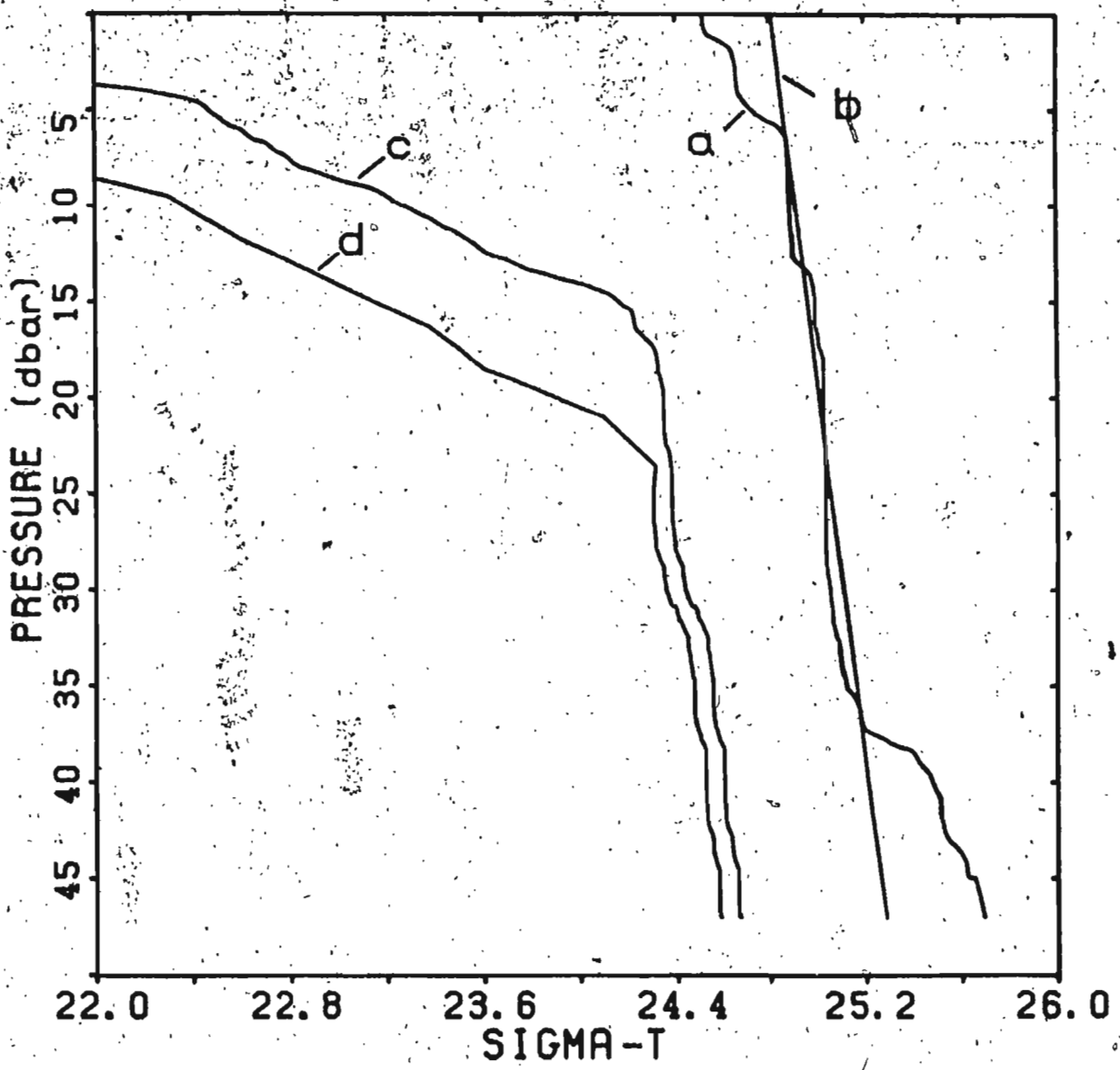

Figure 5.2 Ambient density profiles: (a) 1983; (b) linear fit to 1983 density profile; (c) 1985; (d) modified 1985 density profile.

the 1985 records. Some of the difference between these calculations and the observations are probably due to the linear approximation to the ambient density profile, in particular the absence of the fresh upper layer.

Table 3 Terminal heights of rise calculated from Eq. (5.16).

S_0	ρ_A kg/m^3	$\Delta\rho$ kg/m^3	$\hat{S}$	h_B m
30.0	1024.25	1.23	0.062	36.8
29.5	1023.65	1.63	0.035	41.4
29.0	1023.25	2.03	0.023	43.8
28.5	1022.84	2.44	0.016	45.6
28.0	1022.44	2.84	0.012	47.6
27.5	1022.04	3.24	0.0089	49.2
27.0	1021.64	3.64	0.0071	50.7
26.5	1021.24	4.04	0.0057	52.0
26.0	1020.83	4.45	0.0047	53.3
25.5	1020.43	4.85	0.0040	54.4
25.0	1020.03	5.25	0.0032	55.6
24.5	1019.63	5.65	0.0029	56.6
24.0	1019.23	6.05	0.0025	57.6

5.4 Numerical model for stratified ambients

In this section we will consider the solutions to the conservation equations by using the integral technique of Morton, Tayler and Turner (1956). For an arbitrary density profile the equations must be solved numerically. We will use the numerical model developed by Ditmars (1969) for a round buoyant jet in a stagnant stratified fluid to determine the gross behavior of the plume under study here. Ambient cross currents are not considered in this model. This is probably a valid assumption since the currents are small in Cambridge Fiord, less than 5 cm/sec as shown in Figure 4.1. The model is applicable to horizontal, vertical, and inclined buoyant jets with initially positive or negative buoyancies in stratified or uniform ambient environment. First we will consider the equations of motion and basic assumptions employed in the model.

5.4.1 General assumptions and equations of motion

Figure 5.3 shows a schematic diagram of a buoyant plume in a stagnant environment with an arbitrary density gradient. The flow is assumed axisymmetric about the z-axis with radial coordinate r. This is partially confirmed by acoustic images A and B in Figure 3.2.

The general assumptions underlying the analysis of buoyant jets are now given. The fluids are incompressible and the flow is steady in the mean. The flow is fully turbulent, all terms in the equations of motion are written as the sum of a mean and a fluctuating component (e.g. $U_r = \bar{U}_r + u'_r$). Also the molecular transport terms can be neglected with respect to the turbulent transport terms. The Boussinesq approximation is used, ie. the density difference between the ambient fluid and the buoyant fluid will be neglected except in the buoyancy term, where they occur in the combination $g \frac{\Delta\rho}{\rho_0}$. A linear relationship between

density, temperature and salinity is assumed. This assumption is necessary to write the conservation of buoyancy or density deficiency equation. Justification of this assumption is presented in the next section. Finally the velocity, concentration, and buoyancy profiles are similar at all cross-sections normal to the plume trajectory. Thus the analysis applies only to the zone of established flow where the profiles are fully developed. In general therefore the initial conditions must be adjusted to take into account the zone of flow establishment (Fan and Brooks, 1969).

Considering the above assumptions the stream-wise and cross-stream components of the Navier Stokes equations in cylindrical coordinates can be greatly simplified. We use the same dimensional analysis as Tennekes and Lumley (1972, p. 196), that is, the width of the plume is small compared to its vertical length scale. The integrated cross-stream momentum equation is then used to substitute for the pressure gradient term, the stream-wise or vertical momentum equation then reduces to

$$\left\{ U_z \frac{\partial U_z}{\partial z} + U_r \frac{\partial U_z}{\partial r} \right\} = g \frac{\rho_a - \rho}{\rho_0} - \frac{1}{r} \frac{\partial}{\partial r} (r \overline{U'_z U'_r}) \qquad (5.17)$$

where ρ_a is the ambient density, the primes denote fluctuating quantities and the overbar a time average. The continuity equation is

$$\frac{\partial U_z}{\partial z} + \frac{1}{r} \frac{\partial}{\partial r} (r U_r) = 0 \qquad (5.18)$$

Similarly the equations for conservation of salt and heat are

$$U_z \frac{\partial S}{\partial z} + U_r \frac{\partial S}{\partial r} = -\frac{1}{r} \frac{\partial}{\partial r} (r \overline{U'_r S'}) \qquad (5.19)$$

$$U_z \frac{\partial T}{\partial z} + U_r \frac{\partial T}{\partial r} = -\frac{1}{r} \frac{\partial}{\partial r} (r \overline{U'_r T'}) \qquad (5.20)$$

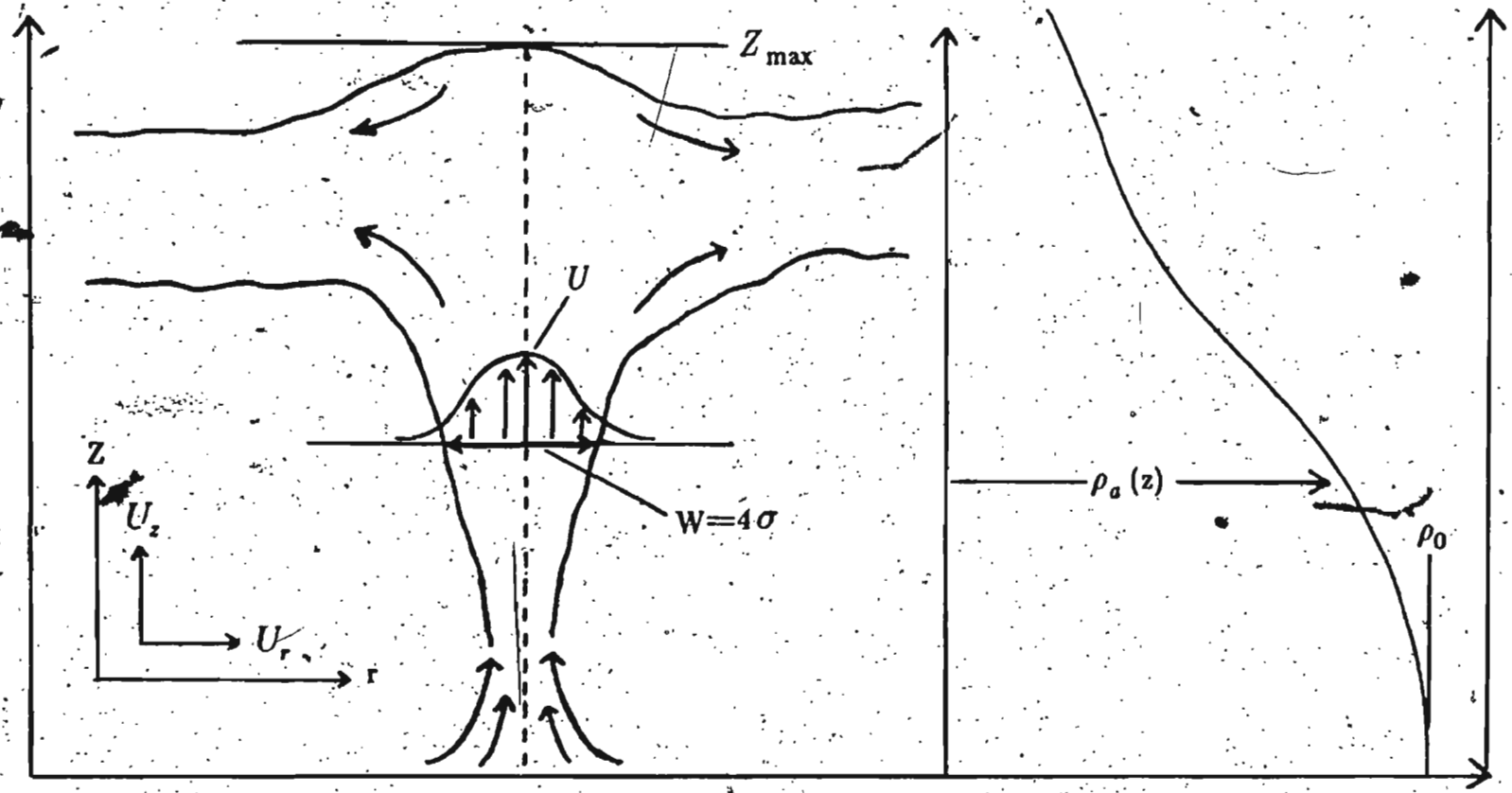

Figure 5.3 Schematic diagram of a round buoyant plume in a stagnant, arbitrary density-stratified fluid.

Assuming density variations are caused by linear changes in temperature and salt concentration

$$\frac{\rho - \rho_a}{\rho_0} = a_1(S - S_a) + a_2(T - T_a) \qquad (5.21)$$

and combining this with Equations (5.19) and (5.20) we can write the conservation of buoyancy or density deficiency equation as

$$U_z \frac{\partial}{\partial z}\left[g\frac{(\rho - \rho_a)}{\rho_0}\right] + U_r \frac{\partial}{\partial r}\left[g\frac{(\rho - \rho_a)}{\rho_0}\right] = -\frac{1}{r}\frac{\partial}{\partial r}\left[\frac{gr}{\rho_0}\overline{U'_r(\rho - \rho_a)'}\right] \qquad (5.22)$$

The solutions to Equations (5.17), (5.18) and (5.22) cannot be found without specifying some of the terms since there are too many unknowns for the number of equations. One approach would be to specify constitutive relations for the turbulent transport terms $\overline{U'_z U'_r}$, $\overline{U'_r T'}$ and $\overline{U'_r S'}$. We will consider the integrated conservation equations across the plume trajectory and assume the turbulent transport terms vanish at large distances from the plume axis.

5.4.2 Equation of state

As mentioned previously density variations are assumed to be linearly related to changes in temperature and salinity. An analysis of the equation of state at low temperatures is made here to determine the importance of the non-linear terms.

The UNESCO equation of state expresses the density of seawater as a function of temperature, practical salinity and pressure in the form

$$\rho(S,T,P) = \rho(S,T,0)\left[1 - \frac{P}{K(S,T,P)}\right]^{-1} \qquad (5.23)$$

where $K(S,T,P)$ is the secant bulk modulus. This equation is valid for $S = 0$

to 42, T = -2 to 40°C and P = 0 to 1000 bars (Millero et al., 1980; Millero and Poisson, 1981). In Cambridge Fiord where we have a water depth of 50 m the non-hydrostatic effects of pressure on density are negligible. The water density at $T = 0$ and $S = 30$ can then be written as (Gill, 1982)

$$\rho(S',T',0) = 1021.07 + 0.81S' - 3.81\times10^{-2}T' - 7.07\times10^{-3}T'^2 - 3.25\times10^{-3}T'S' + 10^{-4}S'^2 + 10^{-5}S'T'^2 \qquad (5.24)$$

where T' and S' are temperature and salinity changes relative to 0°C and 30 respectively. For temperature and salinity changes of the order of 1.0°C and 1.0, all non-linear terms in Eq. (5.24) except the T'^2 term are at least an order of magnitude smaller than the linear terms. Also the linear salinity term is more important than the linear temperature term. We can therefore conclude that the linear assumption used to derive Eq. (5.22) is acceptable.

5.4.3 Specific assumptions

Consider a vertical buoyant plume issuing from the origin. The local velocity and density U_z' and ρ' are functions of r and z while U and ρ are the characteristic velocity and density at the center-line or z-axis. The ambient density ρ_a is a function of z only for vertical plumes.

Further assumptions regarding the entrainment of ambient fluid into the plume and also the shape of the velocity, density and concentration profiles are required to close the set of equations. The profiles are assumed to be Gaussian in shape: that is the center-line values are related to the local values by a Gaussian function. Top hat profiles can also be used: that is, the values of the plume variables are assumed to be equal to the ambient values for radial distances greater than the radius of the plume and are equal to a constant across the width of the plume.

The classical entrainment assumption of Taylor (1958) is used to describe the flow of ambient fluid into the plume. The entrainment rate, which is equal to the rate of change of the volume flux with respect to z, is assumed proportional to the mean center-line velocity. This is found by integrating Eq. (5.18) over the plume to a radius $b(z)$ and assuming $U_z \to 0$ as $b(z)$ becomes large.

$$\frac{dQ}{dz} = - \lim_{r \to b(z)} 2\pi r U_r \tag{5.25a}$$

Taylor's entrainment hypothesis then implies that

$$\frac{dQ}{dz} = - \lim_{r \to b(z)} 2\pi r U_r = 2\pi \alpha b U \tag{5.25b}$$

where Q is the volume flux across the plume cross-section, α is the entrainment coefficient and b is a characteristic length scale defined by the Gaussian velocity profile in Eq. (5.26) below. Experimental studies by Fan (1967) have shown that α is equal to 0.082 for buoyant jets and plumes and 0.057 for simple momentum jets. The nominal half-width of the plume is commonly defined as two standard deviations from the mean of the Gaussian distribution or $\sqrt{2}b$.

The velocity profiles are assumed to be self similar and Gaussian with no angular dependence.

$$U_z(z,r) = U(z) e^{\frac{-r^2}{b^2}} \tag{5.26}$$

Also the profiles of density deficiency or buoyancy are assumed to be similar at all cross-sections with no angular dependence. In a density stratified environment they are given by

$$\frac{\rho_a(z) - \rho^*(z,r)}{\rho_0} = \frac{\rho_a(z) - \rho(z)}{\rho_0} e^{\frac{-r^2}{(\lambda b)^2}} \tag{5.27}$$

The reference density ρ_0 is taken as the value of the ambient density at $z = 0$.

The turbulent Schmidt number λ_s^2 in Eq. (5.27) is defined as the ratio of the width of the density profile to the width of the velocity profile. It is a measure of the plume's ability to disperse density relative to momentum. Studies by Morton (1959) suggested that λ_s be set equal to 1.16.

Equations (5.25) to (5.27) are substituted into Eqs. (5.17), (5.18) and (5.22) and integrated with respect to r to give the following set of equations for continuity, momentum and buoyancy.

$$\frac{d}{dz}(U\, b^2) = 2\alpha U b \tag{5.28}$$

$$\frac{d}{dz}\left[\frac{U^2 b^2}{2}\right] = g\lambda_s^2 b^2 \frac{(\rho_a - \rho)}{\rho_0} \tag{5.29}$$

$$\frac{d}{dz}\left[U b^2(\rho_a - \rho)\right] = \frac{1+\lambda_s^2}{\lambda_s^2} b^2 U \frac{d\rho_a}{dz} \tag{5.30}$$

We now have three equations in three unknowns namely U, b, and $\rho_a - \rho$, which are functions of the vertical center-line coordinate z only. Equations (5.28) to (5.30) can be simplified and combined to give the following set of first-order ordinary differential equations.

$$\frac{dU}{dz} = \frac{2g\lambda_s^2}{U}\frac{(\rho_a - \rho)}{\rho_0} - \frac{2U\alpha}{b} \tag{5.31}$$

$$\frac{db}{dz} = 2\alpha - \frac{bg\lambda_s^2}{U^2}\frac{(\rho_a - \rho)}{\rho_0} \tag{5.32}$$

$$\frac{d}{dz}(\rho_a - \rho) = \frac{1+\lambda_s^2}{\lambda_s^2}\frac{d\rho_a}{dz} - \frac{2\alpha}{b}(\rho_a - \rho) \tag{5.33}$$

These equations are then integrated numerically by Runge - Kutta - Gill methods until the maximum height of rise has been reached or, in the case of vertical

plumes, until the vertical velocity vanishes or becomes very small.

The diameter D as calculated from Eq. (5.14) is the top hat value determined from volume flux considerations. The numerical model calculations assume fully developed Gaussian profiles of velocity. The nominal plume width is then defined as four standard deviations of the Gaussian profile. It is therefore necessary to convert the initial top hat plume diameter to an initial plume width based on this definition. Using the Gaussian velocity profile defined by Eq. (5.26) the initial volume flux is given by

$$Q' = 2\pi U_0 \int_0^\infty r \, e^{-\frac{r^2}{b_0^2}} dr \tag{5.34}$$

Equating the above equation to the top hat volume flux Eq. (5.1), we obtain, $b_0 = D/2$. From the definition of a Gaussian profile and comparison to Eq. (5.34) we obtain $\sigma = b_0/\sqrt{2}$. Therefore the initial plume width (4σ) is equal to $\sqrt{2}D$.

5.4.4 Numerical results

The model described above has been used to calculate the gross behavior of the submarine spring plume using the data collected in 1983 and 1985. The model was run for a range of initial discharge salinities and freshwater discharge rates. The initial velocity used in the model was 30 cm/sec representing the average measured value at one meter above the bottom from the submersible. A range of initial velocities from 15 to 40 cm/sec was tried but it was found that the model results were insensitive to this range of discharge velocities except in the initial few meters of the trajectory.

The numerical model was first checked against the dimensional asymptotic model used in section 5.3. Figure 5.4 shows a plot of the asymptotic results of Table 3 and numerical calculations for the same linear density gradient shown in Figure 5.2. All other input variables (initial velocity, diameter and discharge rate) were the same. Both the asymptotic and the numerical results for the maximum height of rise decrease with increasing initial discharge salinity. For an initial discharge salinity of 28 there is about a 4 m or 10 percent difference in the maximum height of rise between the two models. The agreement between the models increases with decreasing initial discharge salinity. However even for initial salinities above 28 the agreement is acceptable.

Figure 5.5a shows the model results for a range of discharge salinities from 26 to 30. The 1985 ambient density profile was used in these calculations The numerical calculations start at 1.0 m above the bottom and extend up to the maximum height of rise. The initial plume widths calculated by the model are of the same order as observed from the submersible. Plume widths increase linearly up to a height of 18 to 30 m for initial discharge salinities of 30 to 26 after which they increase very rapidly as the plume spreads horizontally. At the maximum

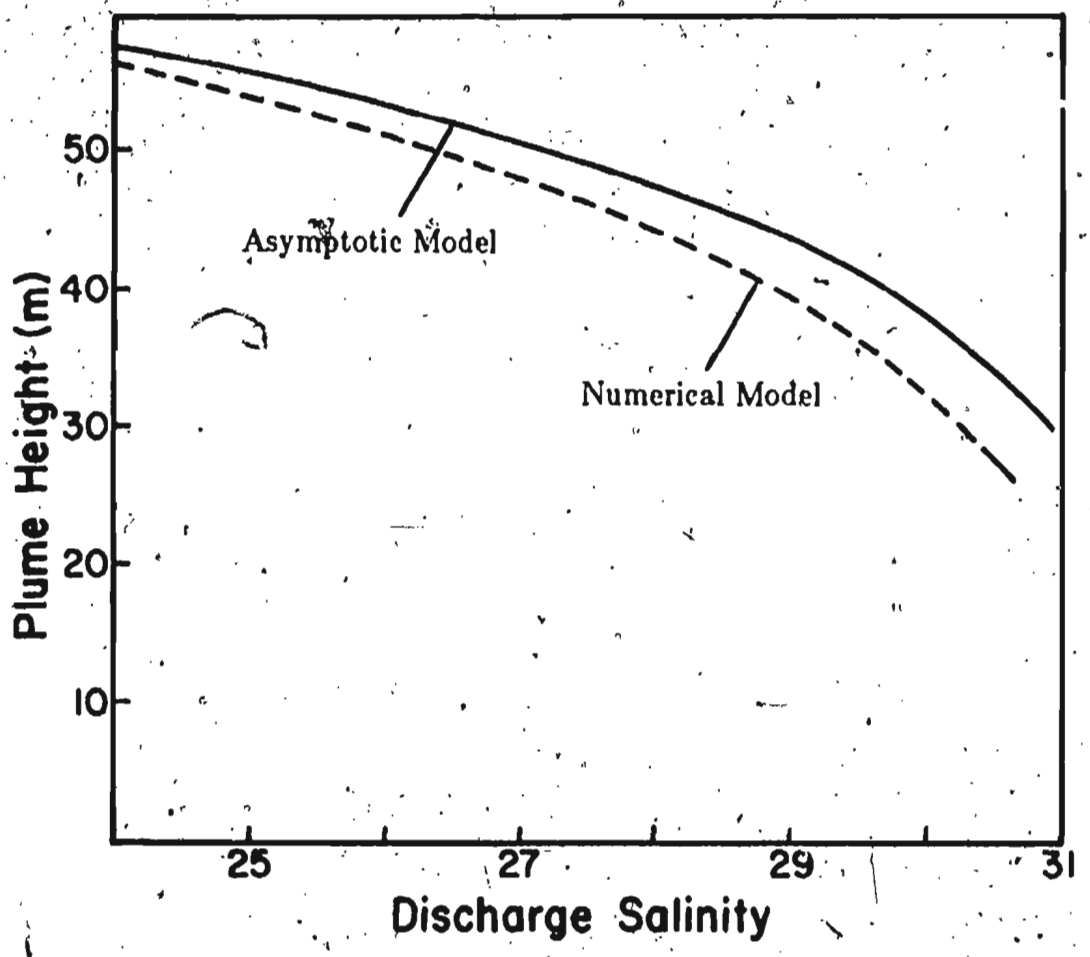

Figure 5.4 Asymptotic and model calculations for the maximum height of rise versus initial discharge salinity.

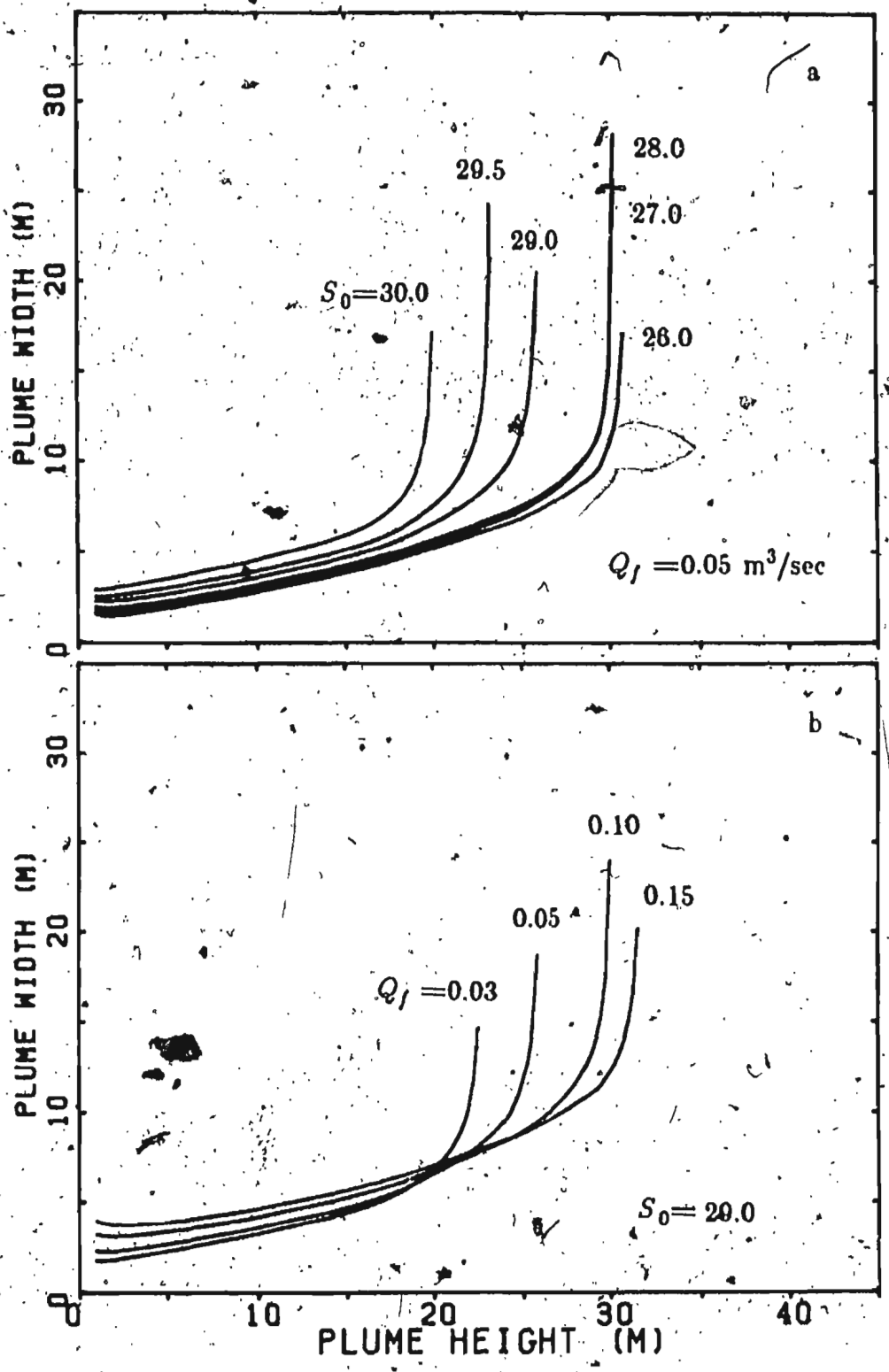

Figure 5.5 (a) Plume width versus height for different S_0
(b) Plume width versus height for different Q_f

height of rise the fluid will have negative buoyancy and the flow is no longer plume-like. At this point the equations are no longer valid and the calculated widths are meaningless. We see that the initial plume width increases with increasing discharge salinity. This is expected since the discharge diameter increases with discharge salinity as seen in Figure 5.1. The height of maximum width appears to approach an asymptotic limit with increasing buoyancy flux. This is due to the presence of the fresh upper layer, which essentially caps the vertical flow.

Presented in Figure 5.5b are model results for an initial discharge salinity of 29.0 and a range of freshwater discharge rates from 0.03 to 0.15 m^3/sec. Again the width increases linearly up to 20 to 30 m for these discharge rates. The initial widths and also the heights of maximum width decrease with decreasing freshwater discharge.

Figure 5.6 shows comparisons between the experimentally determined plume widths from the acoustic maps and the model results for an initial discharge salinity of 29.5 and a freshwater discharge rate of 0.10 and 0.05 m^3/sec. The results of the acoustic survey were obtained one day before the ambient density profile was measured. The acoustic images A and D show a difference in maximum height of rise of about 5.0 m. This is believed to be related to changes in ambient stratification as outlined in section 3.2. Based on this analysis the ambient density profile was artificially modified as shown by trace d in Figure 5.2. Essentially the profile was lowered approximately 5 m.

The experimentally determined curve for plume widths in Figure 5.6a show similar variations with vertical distance to those predicted by the model. The increase in width is approximately linear up until the plume spreads out horizontally, after which it increases very rapidly. The height at which this occurs is

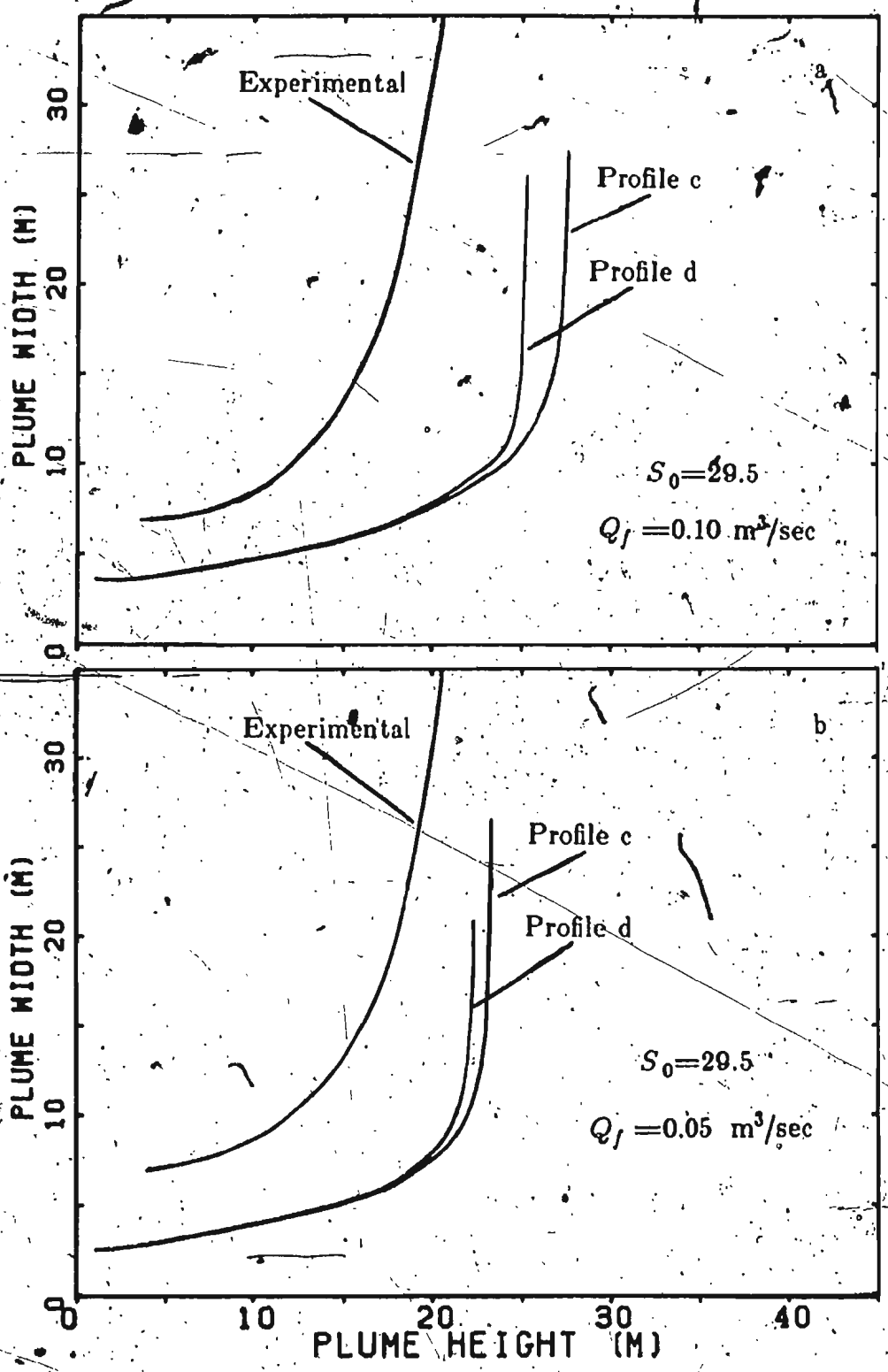

Figure 5.6 (a) Comparisons of plume width for different ambient density profiles and the experimental widths for S_0=29.5 and Q_f =0.10 m ^{3}/sec, (b) S_0=29.5 and Q_f =0.05 m^3/sec.

about 25 percent higher for the model results. If however, we use the modified ambient density profile this difference decreases to approximately 18 percent. The model tends to approximate the experimental results more closely with decreasing freshwater discharge as shown in Figure 5.6b. Here the discharge salinity is the same but the freshwater discharge rate was decreased to 0.05 m^3/sec. The differences in the widths for the two density profiles are decreased, but the height at which the plume spreads out horizontally approximates the experimental result more closely, to within 12 to 15 percent in this case. This leads us to conclude that the freshwater discharge rate is somewhat less than that estimated by Sadler and Serson, probably between 0.05 and 0.10 m^3/sec. Also the agreement between the experimental widths and the model results increase with increasing discharge salinities. The average salinities measured from the submersible approximately 1.0 m from the bottom were in the range of 27 to 29.5 for different time series.

Figure 5.7a shows the maximum height of rise as calculated from the model for the 1983 and 1985 data. The maximum heights of rise of the plume in 1983 as determined from the Ross sounder records were between 37 to 41 m and 34 to 36 m in 1985. The maximum heights of rise predicted by the model for a discharge salinity of 29.0 were 33.3 and 30.0 m for 1983 and 1985 respectively. This is within 15 percent of the heights measured acoustically. The plume heights were lower in 1985 due to the fresh upper layer as opposed to the relatively less stratified water column in 1983. We see in Figure 5.7a that the maximum height occurs at approximately the same depth as the break in the density profile at 12 m depth. Figure 5.7b are the model predictions for maximum height of rise as a function of freshwater discharge for 1985. The maximum height decreases below $Q_f = 0.05$ m^3/sec, but does not approach zero until Q_f becomes less than 0.01 m^3/sec.

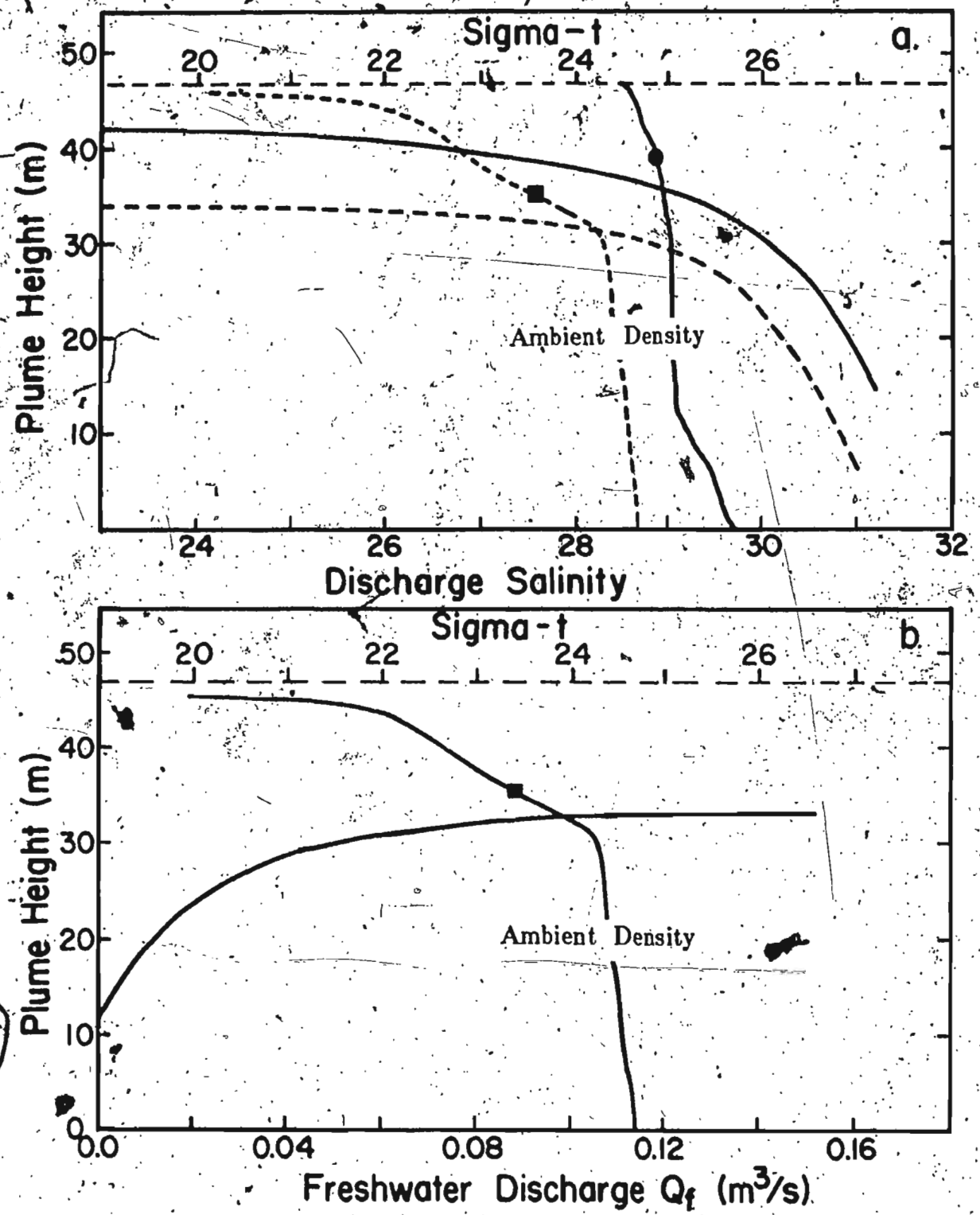

Figure 5.7 (a) Maximum height of rise for 1985 (broken lines) and 1983 (solid lines), versus discharge salinity. The solid square and circle indicate average observed height. (b) Maximum height versus freshwater discharge rate for 1985 data.

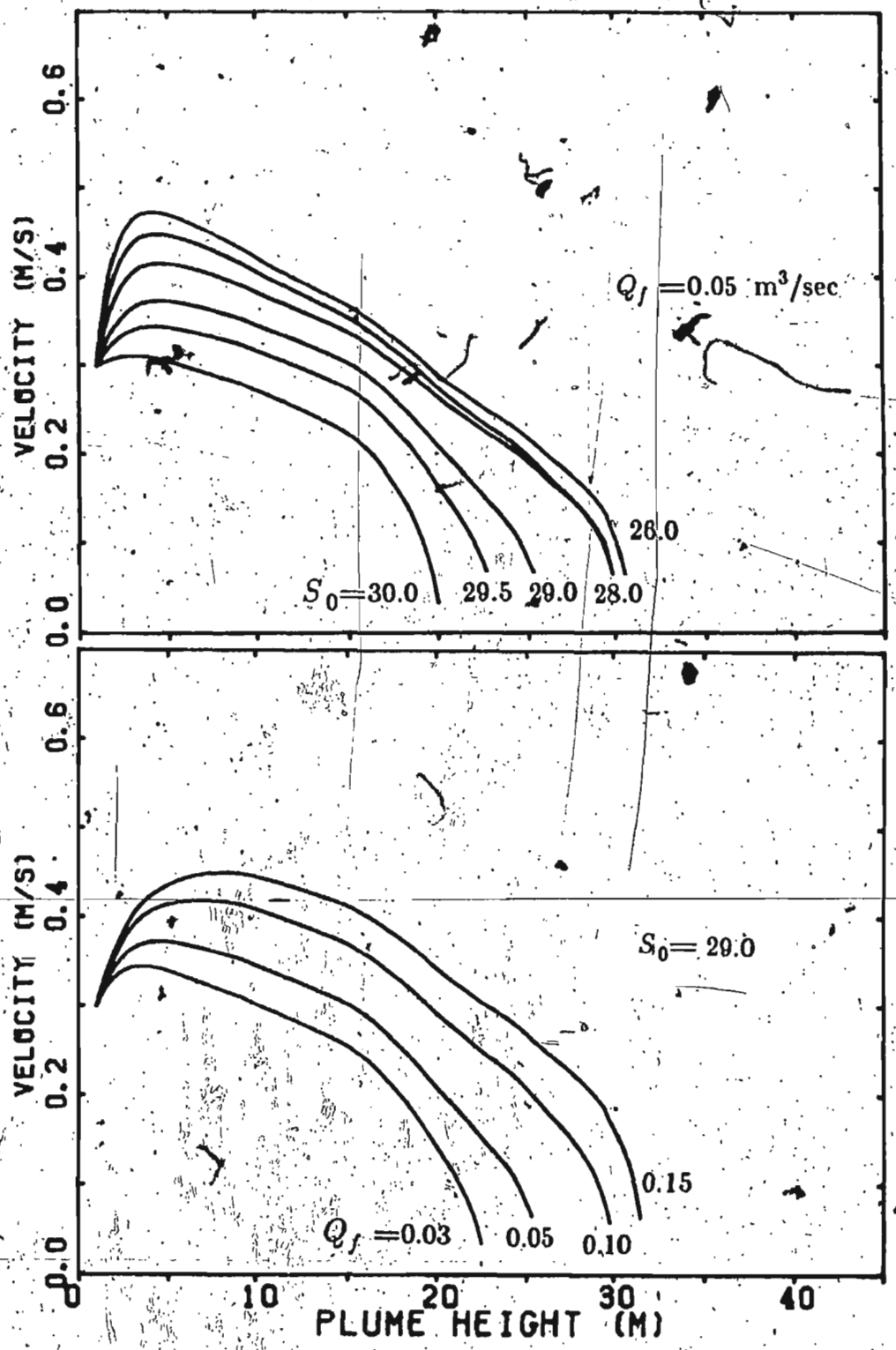

Figure 5.8 Vertical velocity in the rising plume for a range of initial discharge salinities and freshwater discharge rates.

Figure 5.8 shows vertical velocity profiles predicted by the model for a range of initial salinities and discharge rates. Initially the flow accelerates in the first 2 - 4 meters of the trajectory and then decreases approximately linearly. There is some evidence of this higher velocity in acoustic image E on page 36 near the bottom as seen by the almost vertical scattering structures. The vertical velocities obtained from this acoustic image in the 20 to 40 m depth interval appear to remain almost constant at around 30 cm/sec, and then decreases above 20 m depth. However the model results decrease almost linearly in this depth range. These results indicate the vertical velocities predicted by the model are of the same order as those inferred from the acoustic images but there are discrepancies between the predicted and observed variations of velocity with height.

CHAPTER 6 ACOUSTIC BACKSCATTER

6.1 Sound scattering by turbulence

The scattering of sound by turbulence has been studied extensively in the atmosphere (Tatarski, 1961; Ottersten, 1973). In the ocean, acoustic images of internal waves have been attributed to scattering either from biological scatterers often found in association with thermocline or pycnocline zones, or from turbulent fluctuations in the acoustic refractive index associated with temperature and density microstructure (Munk and Garrett, 1973; Haury et al., 1979; Farmer and Smith, 1980).

Several theoretical studies (Batchelor, 1957; Tatarski, 1961; Goodman and Kemp, 1981) have produced expressions for the acoustic scattering cross-section σ, both for atmospheric and oceanic scattering. Goodman and Kemp suggest that in the ocean temperature fluctuations are capable of generating backscatter at detectable levels. The usual expression obtained for the oceanic scattering cross-section for index of refraction fluctuations caused by turbulent microstructure is given by

$$\sigma = 2\pi k^4 \phi(\vec{K}) \tag{6.1}$$

where $|\vec{K}| = 2k \sin\frac{\theta}{2}$, $\phi(\vec{K})$ is the wavenumber spectrum of refractive index fluctuations, $k = \frac{2\pi}{\lambda}$ the wavenumber of the incident sound wave and θ is the

scattering angle. Equation (6.1) can be written in different forms depending on the spectral model used. Sound speed fluctuations arise primarily from temperature fluctuations so we can write (Goodman and Kemp, 1981)

$$\phi(\vec{K}) = \frac{1}{c_0^2}\left(\frac{\partial c}{\partial T}\right)^2 \phi_T(\vec{K}) \tag{6.2}$$

Eq. (6.1) can now be written as

$$\sigma = 2\pi k^4 \frac{1}{c_0^2}\left(\frac{\partial c}{\partial z}\right)^2 \left(\frac{\partial T}{\partial z}\right)^{-2} \phi_T(\vec{K}) \tag{6.3}$$

We see from this expression that the effective cross-section for scattering at the angle θ depends only on spectral components of the turbulence with wave number $K = 2k\sin\frac{\theta}{2}$. That is, the contributions to the backscatter intensity for example, come from the variability in the $\vec{K}$ direction of scale size $\frac{2\pi}{K}$ or $\lambda/2$. Similar expressions for scattering cross-section due to temperature fluctuations in the atmosphere include a $\cos^2\theta$ factor as the only basic difference.

Proni and Apel (1975) calculated acoustic cross-sections using the above expressions for scattering from layered temperature fluctuations. They obtained $\sigma = 2.8\times10^{-7}$ m $^{-1}$ or -66 dB for backscatter at 20 kHz. Goodman and Kemp (1981) similarly obtained a value of 5.46×10^{-7} m $^{-1}$ or -63 dB for σ. Munk and Garrett (1972) calculated cross-sections for vertical narrow-beam scattering of -60 to -40 dB. Typical observed biological cross-sections are about -90 dB daytime and about -70 dB at night.

The turbulence generated by a self-propelled object was clearly observed acoustically by Thorpe and Brubaker (1983) and also by Pelech et al. (1983). A 75 kHz sounder operating with a pulse length of 0.1 ms yielded scattering intensities well above the background for extended periods of time. They calculated a

cross-section of -44 dB, which compared very well to their maximum measured value of -39 dB. Cross-sections of these magnitudes are comparable to cross-sections from natural biological scatterers and are detectable with present day acoustic systems.

There are a number of reasons to suggest that turbulent fluctuations are an important backscatter mechanism in the plume from the submarine spring in Cambridge Fiord. The visual and photographic observations at the vent show the water escaping from the bottom to be very clear and free of gas bubbles and suspended sediments. In 1983 when the plume reached the surface, no suspended sediments or bubbles were observed. The intensity of backscatter from the spreading plume falls off rapidly with radial distance from the plume axis as seen in acoustic images A and B in Chapter 3. This is to be expected since this region is removed from the zone of turbulent kinetic energy production. This is also consistent with the observed radial decay of temperature and salinity fine structure in the CTD profiles.

6.2 Turbulence scales

Turbulence originates when a laminar flow becomes unstable as the Reynolds number increases. These instabilities are a complex interaction of the viscous and nonlinear terms in the equations of motion. A buoyant jet becomes turbulent for Reynolds numbers greater than 5000. The Reynolds number for the buoyant plume under investigation here is calculated to be $UL/\nu \approx 1.0 \times 10^6$ using a mean velocity of 30 cm/sec and a typical plume width of 5.0 m.

A turbulent flow field consists of a spectrum of eddies ranging in size from the width of the flow down to the Kolmogorov microscale, to be defined below. Kinetic energy from the main flow is transferred from the largest eddies to the

smallest where it is dissipated by viscosity. The main parameters governing the small scale motions in turbulent flows are the dissipation rate ϵ and the kinematic viscosity ν, from which we can form length and velocity scales as

$$\eta = (\frac{\nu^3}{\epsilon})^{1/4} \quad , \quad v = (\nu\epsilon)^{1/4} \tag{6.4}$$

These scales are referred to as the Kolmogorov microscales of turbulence. The Reynolds number formed with these scales is 1.0 indicating the viscous nature of the small scale motion. The Kolmogorov microscales are a measure of the smallest size fluctuations that exist in a turbulent flow. In the steady state the supply rate of energy from large to small scale eddies is equal to the dissipation rate ϵ. In the steady state this can be estimated from the mean flow to be

$$\rho\epsilon = \rho\frac{U^2}{2}\frac{U}{L} \tag{6.5}$$

where U is the mean flow speed and L is the scale size of the largest eddies, U/L is proportional to the rate of supply of kinetic energy to the smallest eddies (Tennekes and Lumley, 1972). The value of $\rho\epsilon$ can therefore be estimated for any statistically steady turbulent flow by considering the length and velocity scales of the largest eddies in the flow and using Eq. (6.5). If we take the length scale of the largest eddies in the rising plume to be about 5 m, and a measured velocity of 30 cm/sec we find that $\rho\epsilon$ is approximately 3 W/m^3.

Acoustic backscatter as mentioned before is due to fluctuations with spatial scales of the order of $\lambda/2\sin\frac{\theta}{2}$. For our echo sounder operating at 192 kHz and for scattering at 180° then these spatial scales are about 0.38 cm. This condition is true provided the turbulent fluctuations do not decorrelate during the passage of the acoustic pulse. If we invoke Taylors frozen field hypothesis of turbulence, this means in our case that the turbulent field within each range cell moves only

a small fraction of the wavelength λ during the passage of the incident sound pulse. For vertical plume velocities of 30 cm/sec and a pulse length of 0.5 ms the fluid moves 0.015 cm, which is small compared to the sounder wavelength of 0.76 cm.

The refractive index fluctuations are associated with changes in the salinity and temperature field. The ratio of the sound speed fluctuation c' to the mean speed c_0 at 0°C and a salinity of 30 is given by

$$\frac{c'}{c_0} \approx 3.2\times10^{-3}T' + 9.2\times10^{-4}S' - 3.7\times10^{-5}T'^2 \qquad (6.6)$$

where T' and S' are the temperature and salinity fluctuations (Mackenzie, 1981). We see that the salinity contribution is somewhat smaller than that of temperature and the T'^2 terms are negligibly small. Batchelor (1957) also concluded that fluctuations in sound speed arise mainly from fluctuations in temperature rather than salt concentration. Furthermore he showed that c will be more influenced than density by changes in temperature, while changes in salinity affects c and ρ equally. However in the rising plume the salinity fluctuations are much larger than the temperature fluctuations. With this in mind we will consider the microscales for scalar contaminants in analogy with the Kolmogorov length scale. The scalar microscale for $\gamma_c < \nu$, that is the diffusivity of the contaminant less than the kinematic viscosity, is given by (Tennekes and Lumley 1972).

$$\frac{\eta_c}{\eta} = \left(\frac{\gamma_c}{\nu}\right)^{1/2} \qquad (6.7)$$

where η_c and γ_c are respectively the microscale and diffusivity for the scalar contaminant. For seawater the diffusivities of heat and salt are $\gamma_T = 1.0\times10^{-7}$ m^2/sec and $\gamma_S = 1.0\times10^{-9}$ m^2/sec respectively. Using these values in Eq. (6.7) we get

$$\eta_T = 0.3\eta \tag{6.8}$$

$$\eta_S = 0.03\eta \tag{6.9}$$

Now the temperature and salinity microscales can be expressed in terms of the dissipation rate and the kinematic viscosity:

$$\eta_T = 0.3\left[\frac{\nu^3}{\epsilon}\right]^{1/4} \tag{6.10}$$

$$\eta_S = 0.03\left[\frac{\nu^3}{\epsilon}\right]^{1/4} \tag{6.11}$$

Considering a minimum microscale of one-half the acoustic wavelength ($\lambda/2 =$ 0.38 cm), we find that $\rho\epsilon$ has to be of order 10^{-7} W/m^3 for temperature and 10^{-11} W/m^3 for salinity. However we found that $\rho\epsilon$ is of order 3 W/m^3 for the rising plume, a factor of 10^7 to 10^{11} greater than the required minimum.

We can therefore conclude that the estimates of the temperature and salinity microscales satisfy the scale-to-wavelength condition for acoustic backscatter to occur. The presence of these small scales is confirmed by the visual observations made from the submersible.

6.3 Backscatter versus temperature and salinity fine structure

A plot of relative acoustic backscatter versus depth through the spreading plume is shown in Figure 6.1. This trace is the average of the backscatter signal from 5 successive acoustic transmissions. The large amplitude signal in the first 4 m is nearfield clutter. The high signal level between 8 to 20 m is from the spreading plume. The echo from the descending CTD probe is seen at about 39 m depth. The bottom echo is seen at 47 m with some near bottom scattering from 44 to 47 m depth.

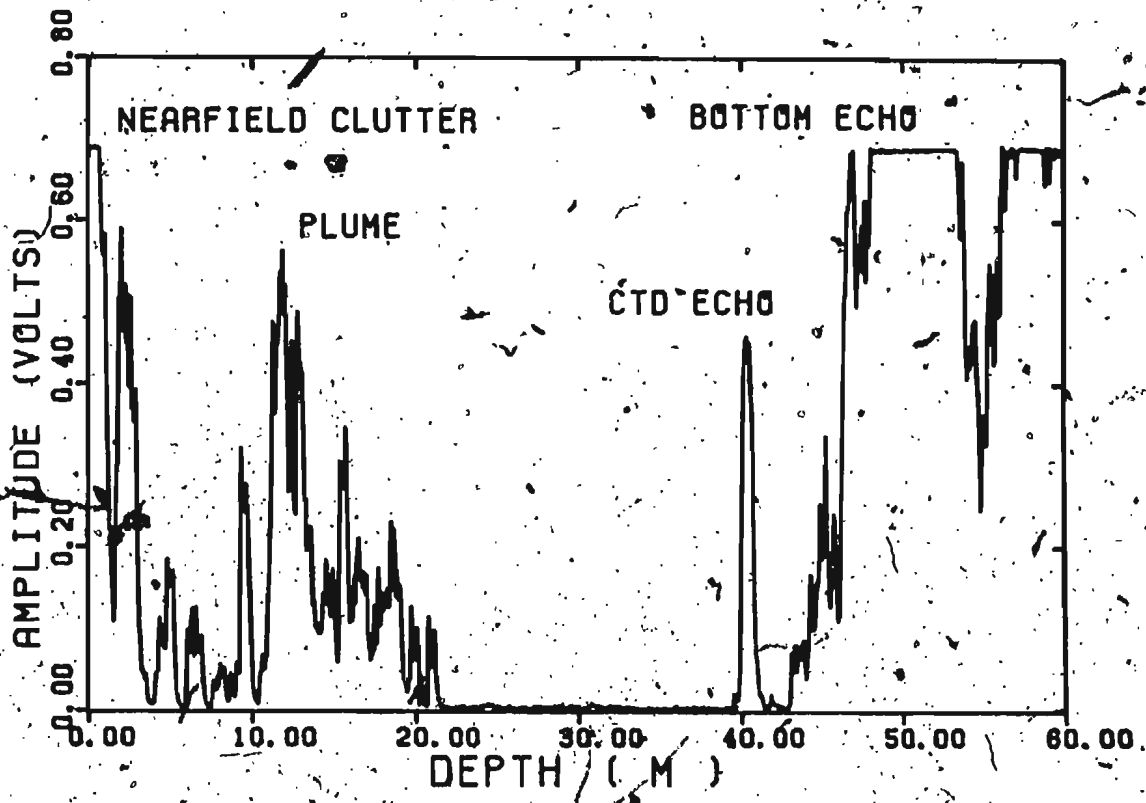

Figure 6.1 A typical 5-ping average of acoustic backscatter amplitude through the spreading plume. Typical scattering features are indicated.

In this section we will compare the relative acoustic backscatter amplitudes to the fine scale fluctuations in temperature and salinity for the acoustic images and corresponding CTD's shown in Figure 3.7. The time interval between successive temperature and salinity measurements with our portable CTD system was 190 ms. The rated response time of the temperature and conductivity sensors is about 60 ms. The speed of the descending CTD probe was approximately 30 cm/sec, the plume was rising at about the same rate, this gives a spatial resolution of approximately 15 cm in the rising plume. However as discussed above acoustic backscatter results from spatial scales of less than 1 cm. Therefore the CTD probe was unable to resolve the microstructure at the scale of interest. Instead we look for associations between high amplitude turbulent fluctuations in the fine scale measurements of temperature and salinity and the backscatter

amplitudes.

The temperature and salinity data examined below were high-pass filtered as discussed in Chapter 2. The filter had a cutoff at about 1.0 m and a length of 1.5 m. This means that all spatial fluctuations of 1.0 m and larger were filtered out. The rms values were then computed by block averaging the square of the high frequency temperature and salinity data over a time interval of approximately 1.3 seconds or about 40 cm in the vertical.

The acoustic profiles shown in Figures 6.2 to 6.5 were selected by averaging 5 acoustic transmissions from the digitized data parallel to the descending CTD probe seen in acoustic images E to H. After being corrected for attenuation and spreading the data were block averaged over a depth interval of 40 cm, which corresponds to the vertical resolution of the sounder ($c\,\tau/2 \approx 40$ cm). The data below also show the percentage of acoustic returns that saturated the detector for each block average, indicating those regions where the backscatter is too strong to be measured at that particular gain. Hence the actual signal level in these regions can be expected to be somewhat higher than that measured. The standard deviation of each block average was also calculated, providing an estimate of the degree of scatter in the measurements.

The rms fluctuations in temperature and salinity are shown in Figure 6.2a and 6.2b for the CTD cast shown in acoustic image E of Figure 3.7 through the rising plume. The corresponding block averaged acoustic backscatter signal is shown in Figure 6.2d and signal saturation level in Figure 6.2c. The increased rms fluctuations in salinity below 27 meters depth are associated with a large increase in the backscatter. In this region of the rising plume the salinity fluctuations are much larger than those of temperature. This is clearly seen in the CTD profile shown in Figure 3.8. As a result the acoustic backscatter seems to

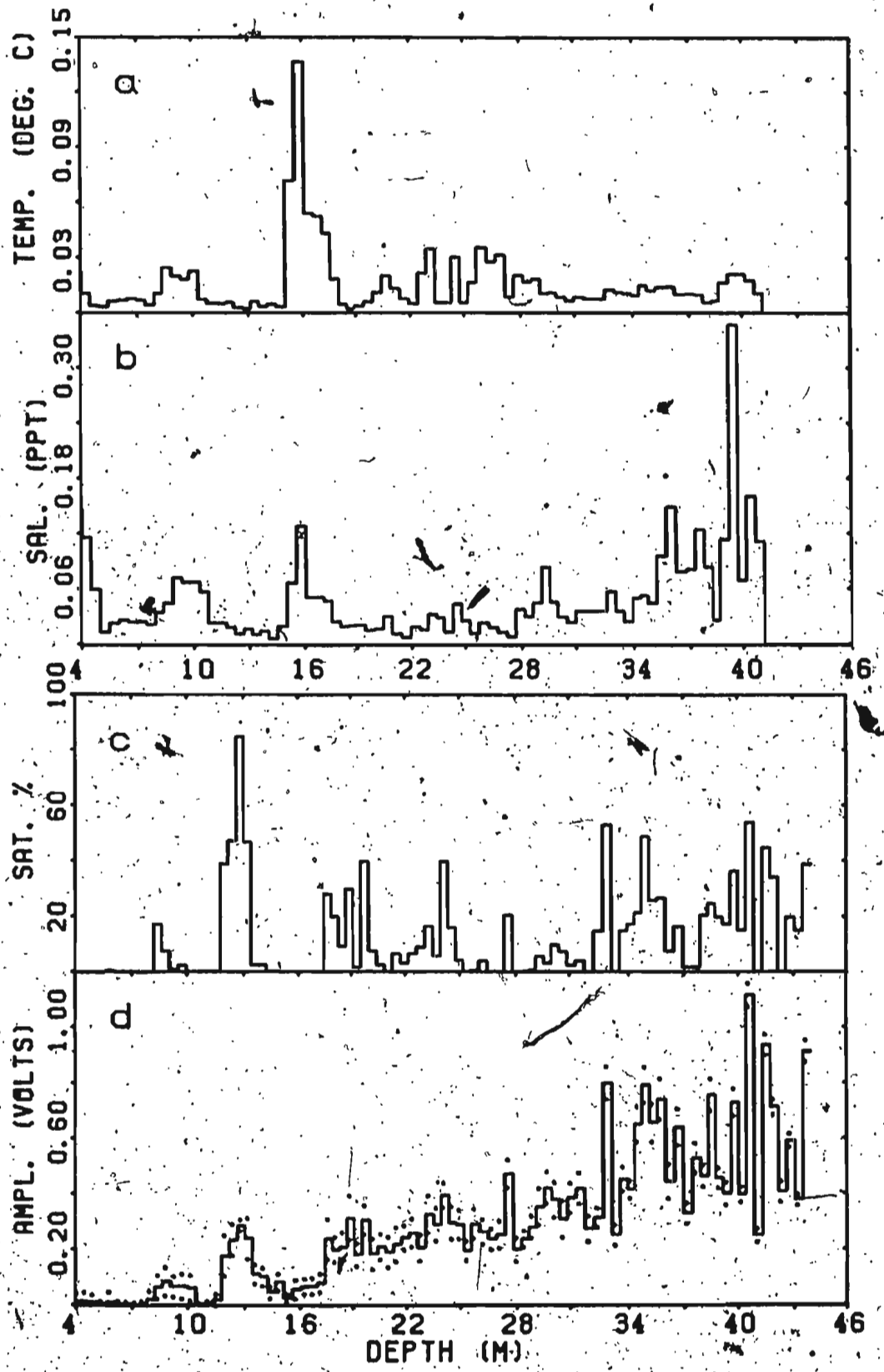

Figure 6.2 Profiles through the rising plume of temperature, salinity and acoustic backscatter corresponding to the acoustic image shown in panel E of Figure 3.7: (a) rms fluctuations in temperature; (b) rms fluctuations in salinity; (c) percentage of acoustic transmissions that saturated the detector; (d) block averaged acoustic backscatter and standard deviations obtained from each block average.

correspond more closely to salinity fluctuations than to temperature fluctuations. Cross correlation coefficients of 0.29 and 0.14 were obtained between the acoustic backscatter and the rms fluctuations in temperature and salinity respectivly.

Figure 6.3 shows the corresponding results for the CTD cast through the rising plume in acoustic image F of Figure 3.7. The high amplitude rms fluctuations in temperature and salinity at approximately 9 m depth correspond to an increase in the acoustic backscatter at that depth. In this region of the plume the fluctuations in temperature are of the same order as those in salinity. We also have as before increasing rms fluctuations in salinity below 24 m depth corresponding to increasing acoustic backscatter. In this profile the rms values of temperature fluctuations also increase with depth below 30 m, although not as significantly as salinity. In this case the cross correlation coefficients are close to zero. This could possibly be due to the spatial separation of the acoustic backscatter profile with respect to the temperature and salinity profiles.

The rms fluctuations shown in Figure 6.4 are for the CTD cast through the spreading plume in acoustic image G in Figure 3.7. The increased acoustic backscatter beginning at approximately 12 m depth is clearly associated with the large increase in the rms values of temperature and salinity at the same depth. Cross correlation coefficients of 0.76 and 0.45 were calculated in this case between temperature, salinity and acoustic backscatter.

The results for the CTD cast in acoustic image H in Figure 3.7 through the spreading plume are shown in Figure 6.5. Again we see a large increase in the rms values of temperature and salinity and corresponding increase in acoustic backscatter occurring at a depth of 11 m where the CTD probe first enters the spreading plume. Again the cross correlation coefficients between temperature, salinity and backscatter were high, 0.70 and 0.65 respectivly.

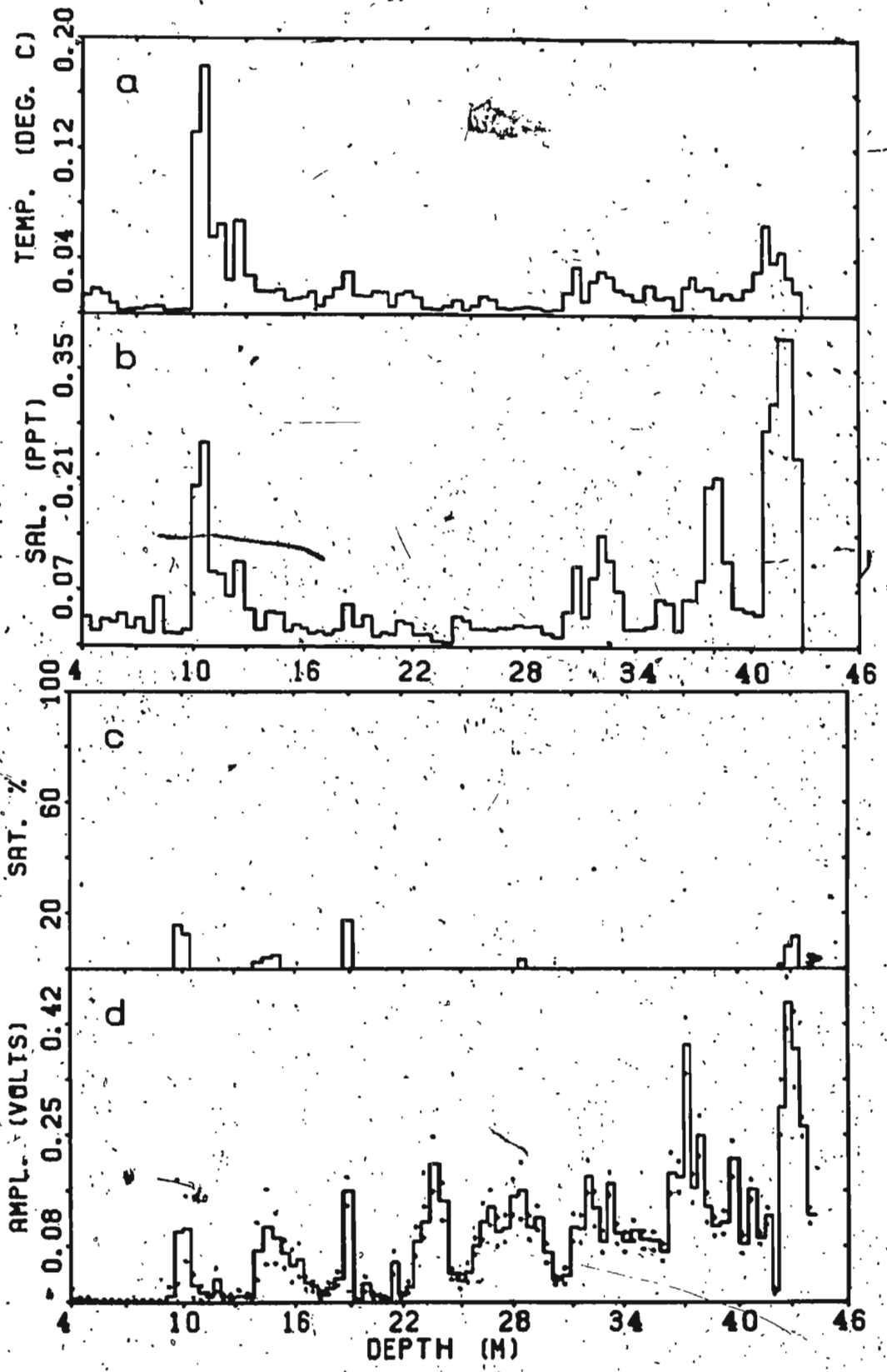

Figure 6.3 Profiles in the rising plume of temperature, salinity and acoustic backscatter corresponding to the acoustic image shown in panel F of Figure 3.7. See also Figure 6.2.

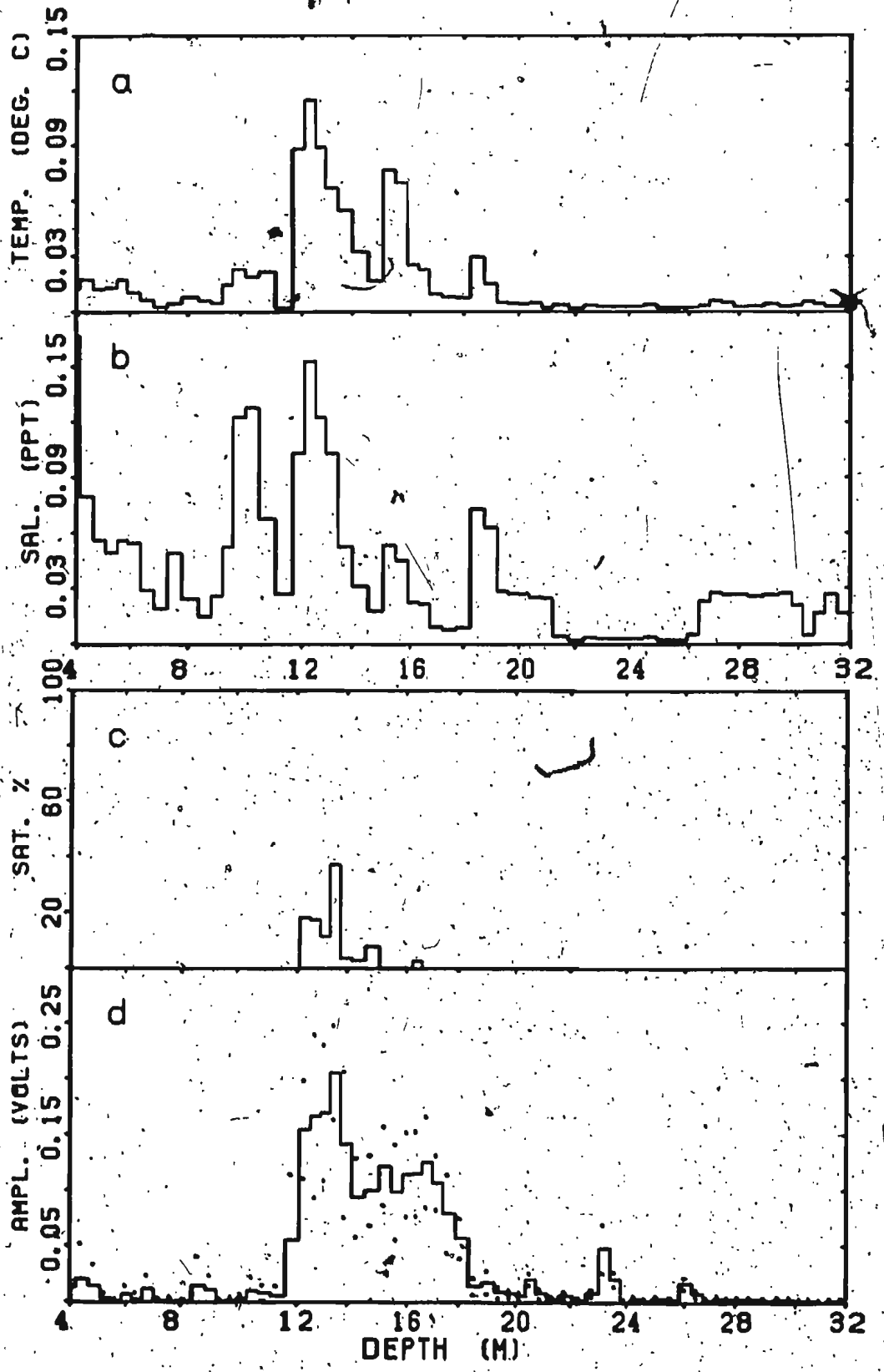

Figure 6.4 Similar results in the spreading plume to those in Figure 6.3 but corresponding to the acoustic image in panel G of Figure 3.7.

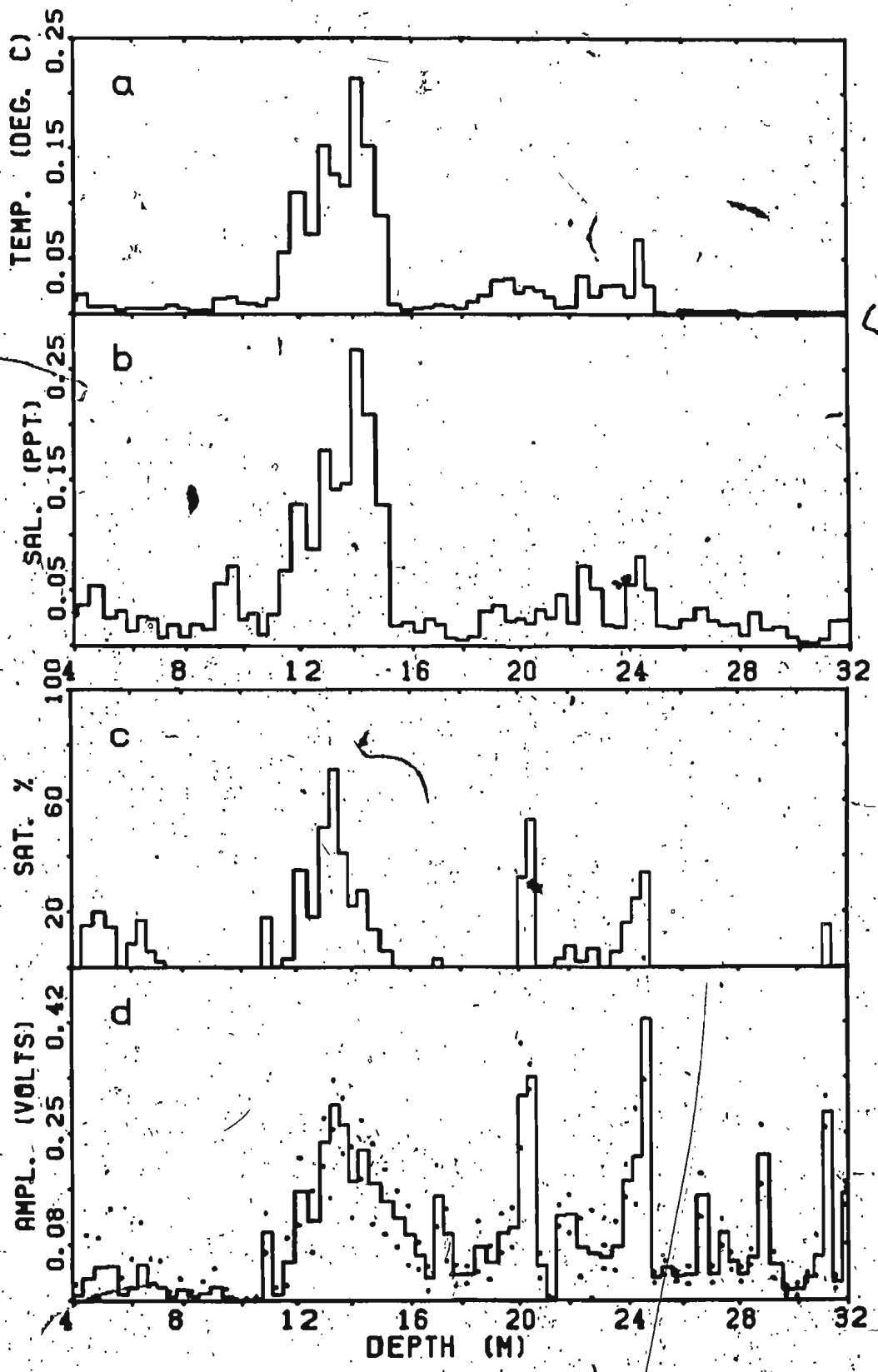

Figure 6.5 Similar to Figure 6.4 but corresponding to acoustic image H of Figure 3.7.

The acoustic backscatter data versus rms temperature, salinity, sound speed and acoustic impedance in the spreading plume are plotted in Figure 6.6 for CTD 8 and 9 corresponding to acoustic images G and H of Figure 3.7. These data were obtained over a depth range of 6.0 to 20 m. These plots indicate a general increase in the backscatter amplitude with increasing rms fluctuations particularly for temperature and sound speed, although there is a high degree of scatter for all four quantities. Some of this scatter is probably due to the high amplitude backscatter from biological scatterers, which was not removed from the data.

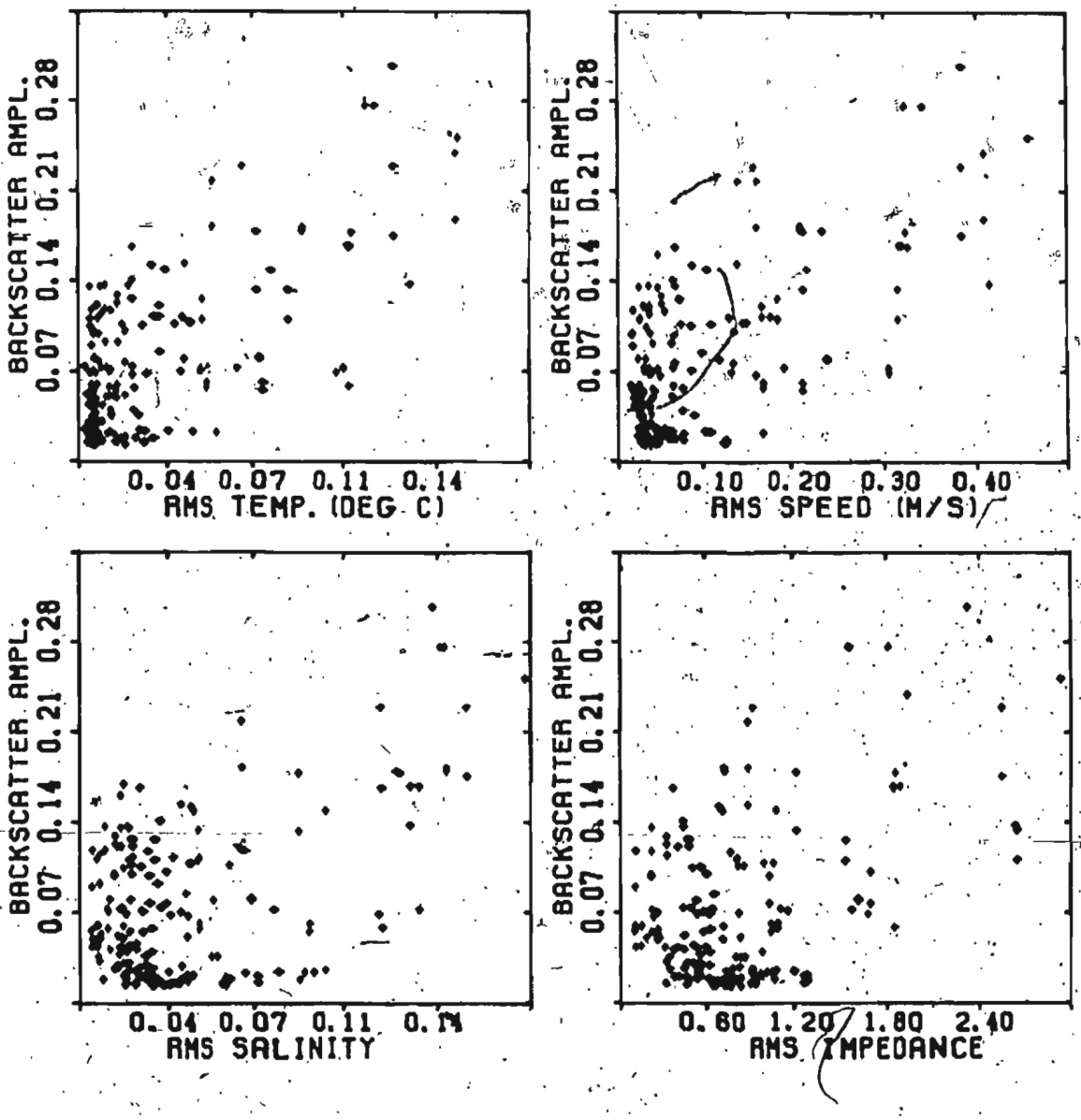

Figure 6.6 Block averaged acoustic backscatter versus the rms fluctuations in temperature, salinity, sound speed and acoustic impedance for CTD's 8 and 9 corresponding to acoustic images G and H of Figure 3.7 in the spreading plume.

6.4 Radial decay of fine structure and backscatter in the spreading plume

6.4.1 Observations

The decay of acoustic backscatter and rms temperature and salinity fine structure with radial distance from the plume axis is shown in Figure 6.7a. This plot was obtained by taking averages over the vertical extent of the spreading plume of all three quantities for CTD transect B through the plume center. CTD's 15 and 16 are at the center of the plume. The dashed curve is the backscatter amplitude, the error bars represent one standard deviation from the amplitude means. We see a rapid drop off in the acoustic backscatter with distance from the plume center. The rms temperature and salinity fine structure also decrease with radial distance.

Figure 6.7b is a plot of acoustic backscatter amplitude versus radial distance from the plume axis at a depth of 26 m in the spreading plume, it was constructed from three acoustic transects through the plume. One of these transects corresponds to acoustic image A in Figure 3.2. The radial distance from the plume center was calculated for each position along the transect. The backscatter amplitudes were then averaged in the vertical over 1 m intervals centered at a depth of 26.0 m and finally block averaged over 15 points or about 4 m in the horizontal. Again the error bars represent one standard deviation from the amplitude means. The rms backscatter falls off rapidly with radial distance from the plume axis for distances greater than 10.0 m.

6.4.2 Production and dissipation in the spreading plume

In a shear flow such as a horizontally spreading plume, it has been shown

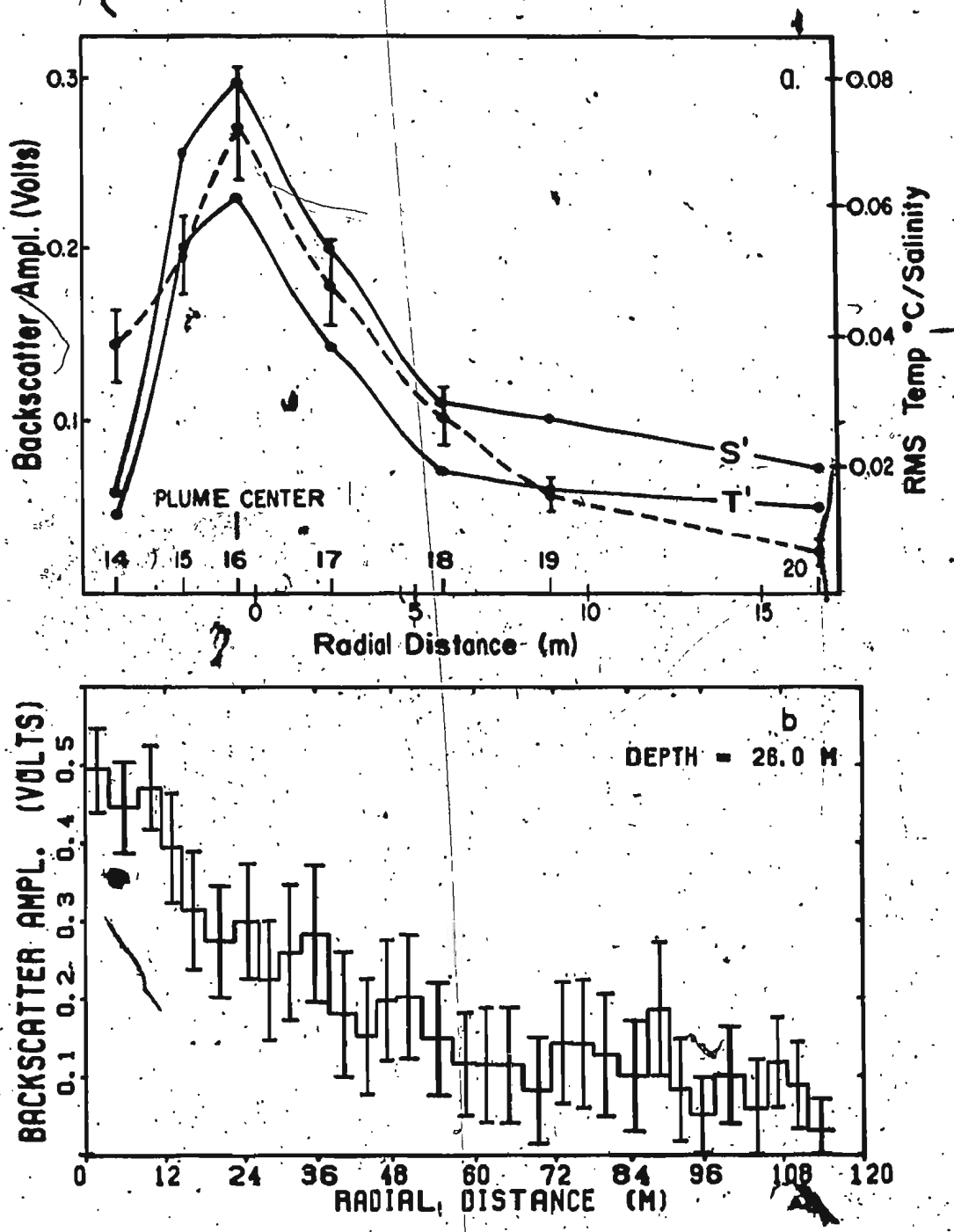

Figure 6.7 (a) Acoustic backscatter and rms fluctuations in temperature and salinity versus radial distance from the plume axis corresponding to CTD transect B. (b) Average acoustic backscatter versus radial distance from the plume axis.

that in order for turbulence to be maintained the gradient Richardson number has to be less than 0.25 (Turner, 1973, p. 97). The gradient Richardson number is given by

$$Ri = \frac{-g}{\rho_0}\left(\frac{\partial \rho}{\partial z}\right) / \left(\frac{\partial U}{\partial z}\right)^2 \qquad (6.12)$$

where U is the horizontal velocity. As shown by the sketch in Figure 6.8, the horizontal velocity in the spreading plume can be estimated by considering the total volume flux at a plume height above which further entrainment is unlikely. Vertical density gradients at both the upper and lower boundaries of the spreading plume were obtained from the CTD profiles. The gradient Richardson number can then be estimated as

$$Ri = \frac{-g}{\rho_0}\frac{\Delta \rho \Delta z}{U^2} \qquad (6.13)$$

assuming uniform flow in the spreading plume and zero horizontal velocity above and below.

For a vertical velocity of 30 cm/sec and a plume width of 13.0 m at approximately 20 m above bottom we get a total volume transport Q of 40 m^3/sec. The horizontal velocity is then $U = Q/2\pi rh$, where r is the radial distance from the plume axis and h is the plume thickness. Horizontal velocities of 20 and 15 cm/sec were calculated for radial distances of 6 and 9 m and plume thicknesses of 6 and 5 m respectively which are the values corresponding to CTD's 8 and 7. Typical values for $\Delta\rho$ and Δz obtained from CTD profiles at the plume boundaries were 0.83 kg/m^3 and 0.92 m for a radial distance of 6.0 m and 0.26 kg/m^3 and 0.77 m for a distance of 9.0 m, giving gradient Richardson numbers of 0.18 and 0.08. Richardson numbers were calculated in this way for several CTD profiles using both the up-cast and the down-cast and gradients at both the top

and bottom of the spreading plume. The estimates range from 0.03 to 0.18 with an overall average of 0.09, for a range of radial distances between 4 to 9 m corresponding to CTD's 7, 8, 9 and 17. The Reynolds number (Uh/ν) at radial distances of 6.0 and 9.0 m are 8.6×10^5 and 5.4×10^5 respectively. These results indicate that turbulence production occurs in the spreading plume for radial distances up to at least 10.0 m. The CTD profiles at radial distances greater than 10.0 m did not exhibit a sharp gradient at the plume boundaries. The mean speed U decreases inversely with radial distance, implying that the gradient Richardson number increases as radial distance squared, so for large distances turbulent production will likely cease.

Finally we consider the time scale for temperature fluctuations at scales of the order of one-half the acoustic wavelength to be dissipated by molecular diffusion. This time scale is given by $t_m = (\Delta z)^2/\gamma_T$ which is approximately 1000 seconds for $\Delta z = 1.0$ cm in seawater. The maximum horizontal distance these fluctuations can travel is found by integrating the radial velocity for 1000 seconds. A maximum radius of 48.0 m was calculated. This indicates that it is possible for turbulent fluctuations of 1.0 cm scale to exist in the absence of production for radial distances up to 48.0 m before being dissipated by viscosity. This is consistent with the maximum horizontal extent of the spreading plume observed acoustically.

6.4.3 Conservation equations in the spreading plume

The conservation of volume in the absence of entrainment is obtained by considering the volume flux through a small cylindrical annulus of thickness Δr and height h and dropping terms of order $(\Delta r)^2$ and higher, we obtain

$$\frac{\partial}{\partial r}(Uhr) = 0 \qquad (6.14)$$

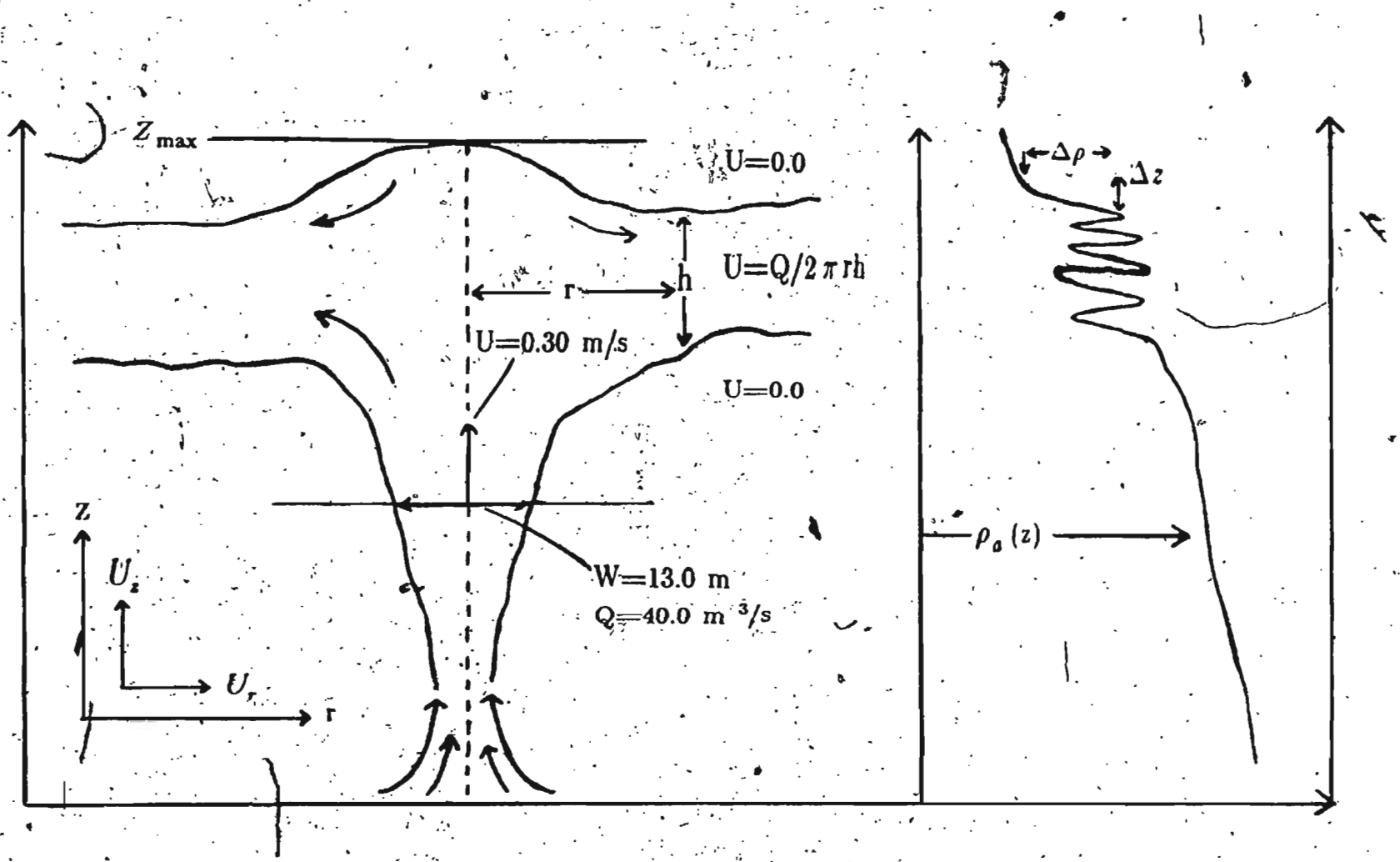

Figure 6.8 Schematic diagram of a buoyant plume showing the parameters used for the gradient Richardson number calculation.

where the variables U, r and h are defined in Figure 6.8. In analogy with Eq. (6.14) we can write down the equation of conservation of point scatterers as

$$\frac{\partial}{\partial r}(CUh) = -\frac{CUh}{r} \tag{6.15}$$

where $C(r)$ represents the scatterer concentration. By combining Eqs. (6.14) and (6.15) we obtain

$$\frac{\partial C}{\partial r} = 0 \tag{6.16}$$

and therefore conclude that the observed radial decay of acoustic backscatter cannot be explained by the spreading of conservative point scatterers at least in the absence of entrainment.

We now consider the conservation of scatterers with entrainment in the spreading plume. For an entrainment velocity W_e at the top and bottom of the spreading plume the equation for conservation of volume becomes

$$\frac{\partial}{\partial r}(Uh) = -\frac{Uh}{r} + 2W_e \tag{6.17}$$

And the equation for conservation of scatterers analagous to Eq. (6.16) is given by

$$\frac{\partial C}{\partial r} = \frac{-2W_e\, C}{Uh} \tag{6.18}$$

If we now assume that the entrainment velocity is proportional to the radial velocity of the spreading plume, $W_e = \beta U$, where β is an entrainment coefficient, and that h is constant then the solution of Eq. (6.18) is given by

$$C = C_0 e^{\frac{-2\beta}{h} r} \tag{6.19}$$

where C_0 is the initial concentration of point scatterers.

We now need to estimate the importance of entrainment by estimating β from the overall Richardson number of the spreading plume. The overall Richardson number R_0 is simply Eq. (6.13) with $\Delta z = h$, the thickness of the plume. With h about 5.0 m at 10 m radial distance, $\Delta\rho = 0.26$ kg/m^3, and a discharge rate of 40 m^3/sec we obtain $R_0 \approx 1.0$. From experimental observations of horizontal surface jets by Ellison and Turner (1959), the entrainment coefficient β is approximately 2.0×10^{-3} for $R_0 \approx 1.0$. From Eq. (6.19) the e-folding radius $h/2\beta$ for the decay of point scatterers would then be about 1000 m for a plume thickness of 5.0 m. So it appears from this analysis that entrainment is not significant at values of $r > 10.0$ m, particularly since R_0 must increase as r increases. Therefore it seems unlikely that the observed decay of acoustic backscatter is due to simple cylindrical spreading of conservative point scatterers.

We will now consider the conservation of turbulent kinetic energy in the absence of dissipation. Using Taylors frozen field hypothesis of turbulence we consider the transport of turbulent velocity fluctuations through a small cylindrical annulus and obtain

$$\frac{\partial}{\partial r}(q^2 Uh) = \frac{-q^2 Uh}{r} \tag{6.20}$$

which has the same form as Eq. (6.15) and therefore becomes using Eq. (6.14)

$$\frac{\partial q^2}{\partial r} = 0 \tag{6.21}$$

Therefore in the absence of dissipation the turbulent kinetic energy behaves like a conservative scalar in the spreading plume. If however we introduce dissipation, which we expect to be important on the basis of the estimates in section 6.4.2 and since production is not expected to be important, there must be a balance between advection and dissipation for the turbulence at a point to be statistically

steady. That is:

$$U\frac{\partial q^2}{\partial r} = \epsilon \qquad (6.22)$$

This has the same form as the energy budget for turbulence decaying downstream of a grid (Tennekes and Lumley, 1972, p. 72), with the downstream distance being replaced by r. Experiments in wind tunnels have indicated that velocity fluctuations decay as one over the downstream distance behind a grid.

When we have an isotropic scalar field superimposed upon the isotropic turbulent velocity field which decays as one over the down stream distance, then from self-preservation arguments the decay of the mean square scalar concentration fluctuations such as temperature and salinity follow a $1/r^{3/2}$ law (Hinze, 1975, p. 301,). Therefore the acoustic backscatter amplitude resulting from these fluctuations should drop-off as $1/r^{3/4}$, since backscatter amplitude is proportional to the square root of the mean square fluctuation amplitude.

Figures 6.9 and 6.10 show plots at 1.0 m intervals of acoustic backscatter amplitude versus radial distance from the plume axis for depths of 24 to 26 m in the spreading plume. These plots are of the same type as Figure 6.7b plotted on a log-log scale. Figure 6.10a for example is a log-log plot of Figure 6.7b. The rms backscatter falls off rapidly with radial distance from the plume axis for distances greater than 10.0 m. The high amplitude backscatter beyond 50.0 m range is due to biological scatterers that were not removed from the data. The dashed lines on these plots are $1/r^{3/4}$ and the solid lines are $1/r$ drop-off rates. All four plots show a reasonable agreement between the acoustic backscatter amplitude decay rates and the $1/r^{3/4}$ law.

Figure 6.11a shows a log-log plot of the backscatter amplitude in Figure 6.7a. The solid and dashed lines are again $1/r$ and $1/r^{3/4}$ respectively. The back-

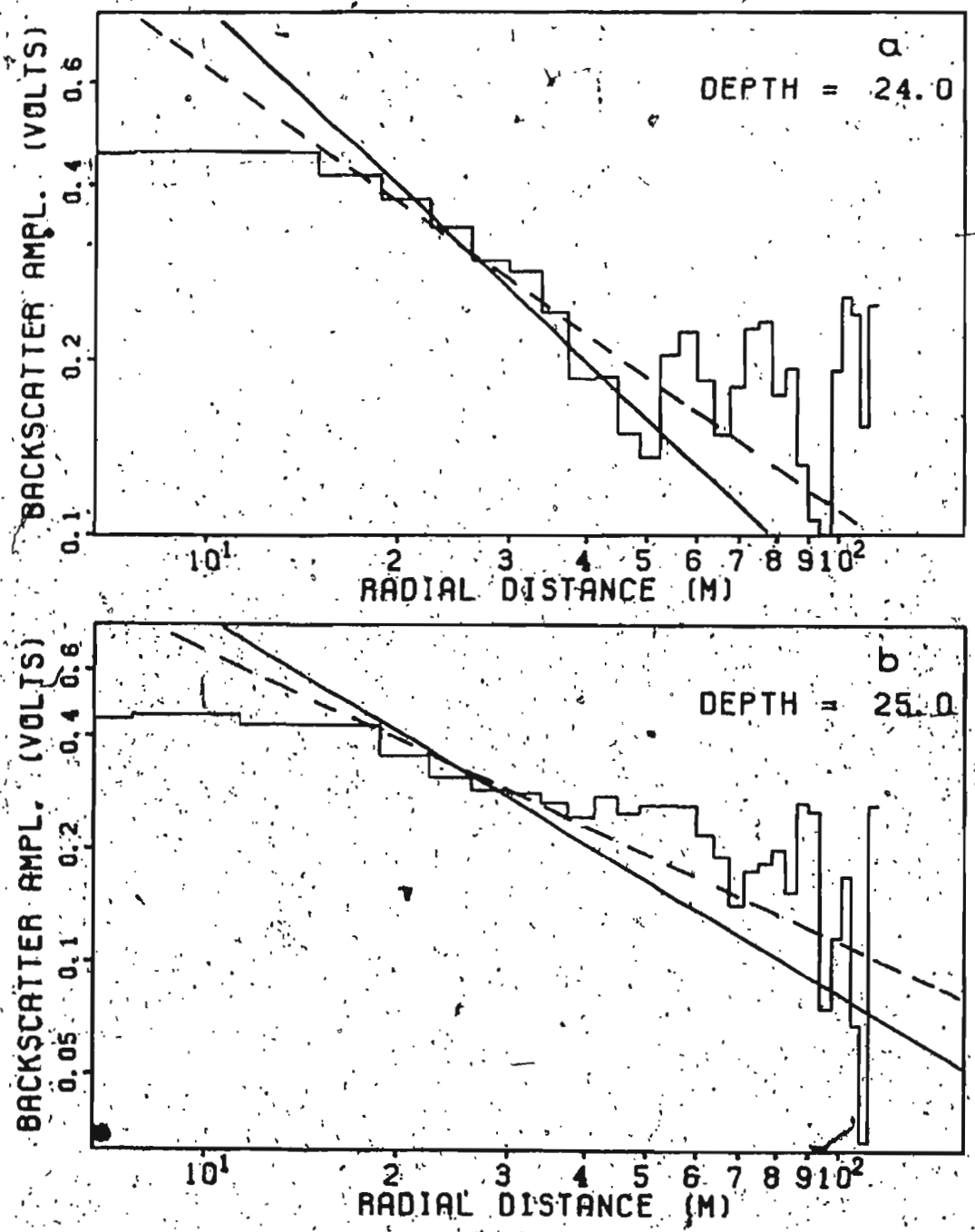

Figure 6.9 (a) Log-log plots of the radial decay of acoustic backscatter amplitudes through the spreading plume at 24.0 m depth. The solid and dashed lines are $1/r$ and $1/r^{3/4}$ drop-off rates. (b) Similar to (a) at 25.0 m.

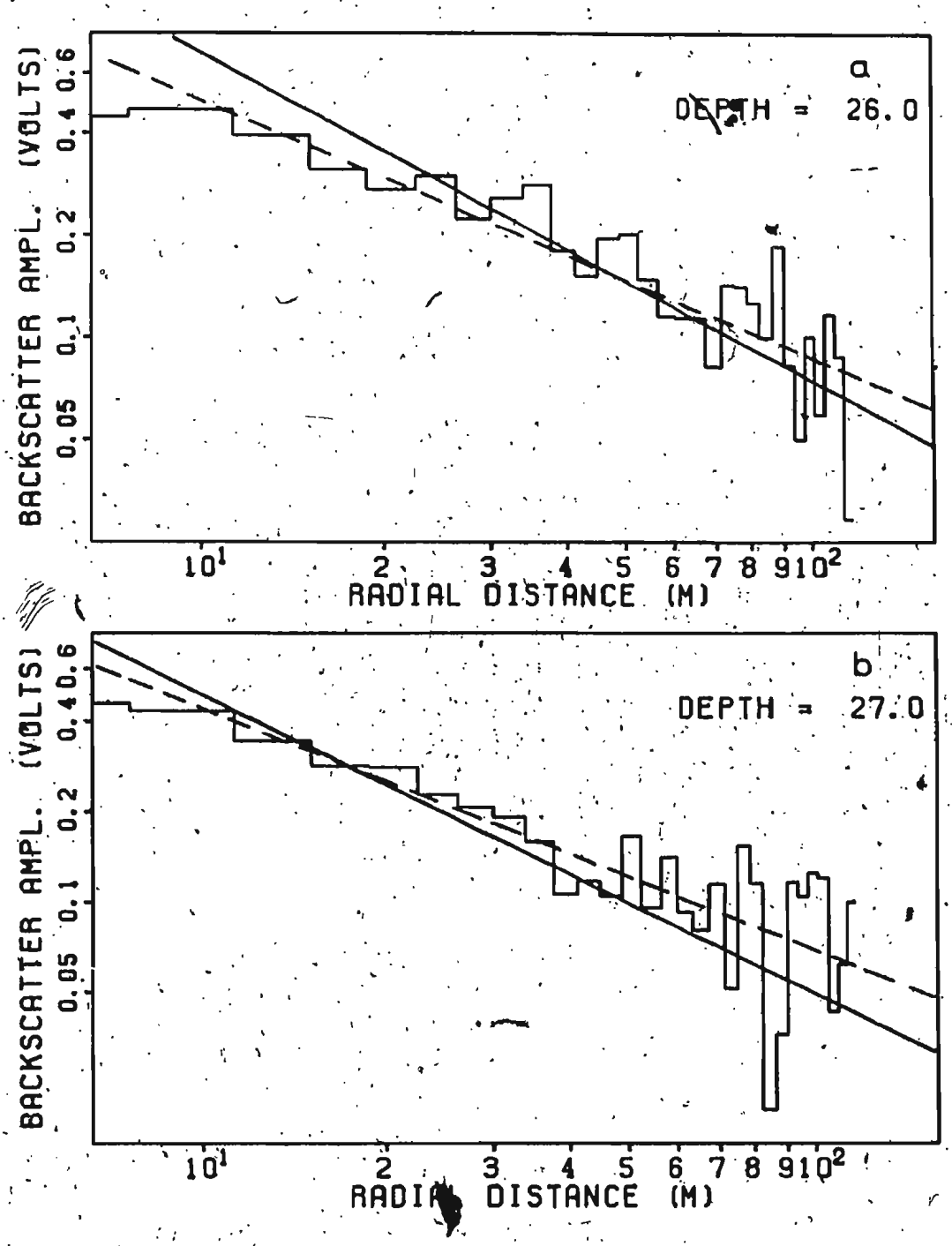

Figure 6.10 (a) Log-log plots of the radial decay of acoustic backscatter amplitudes through the spreading plume at 26.0 m depth. The solid and dashed lines are $1/r$ and $1/r^{3/4}$ drop-off rates. (b) Similar to (a) at 27.0 m.

scatter seems to fit the $1/r^{3/4}$ drop-off rate reasonably well even though these data are close to the plume axis. Figure 6.11b and 6.11c shows log-log plots of the rms temperature and salinity fluctuations shown in Figure 6.7a. Again the $1/r^{3/4}$ drop-off rate fits the data reasonably well. These results support the argument that turbulence is an important mechanism in causing the observed acoustic backscatter.

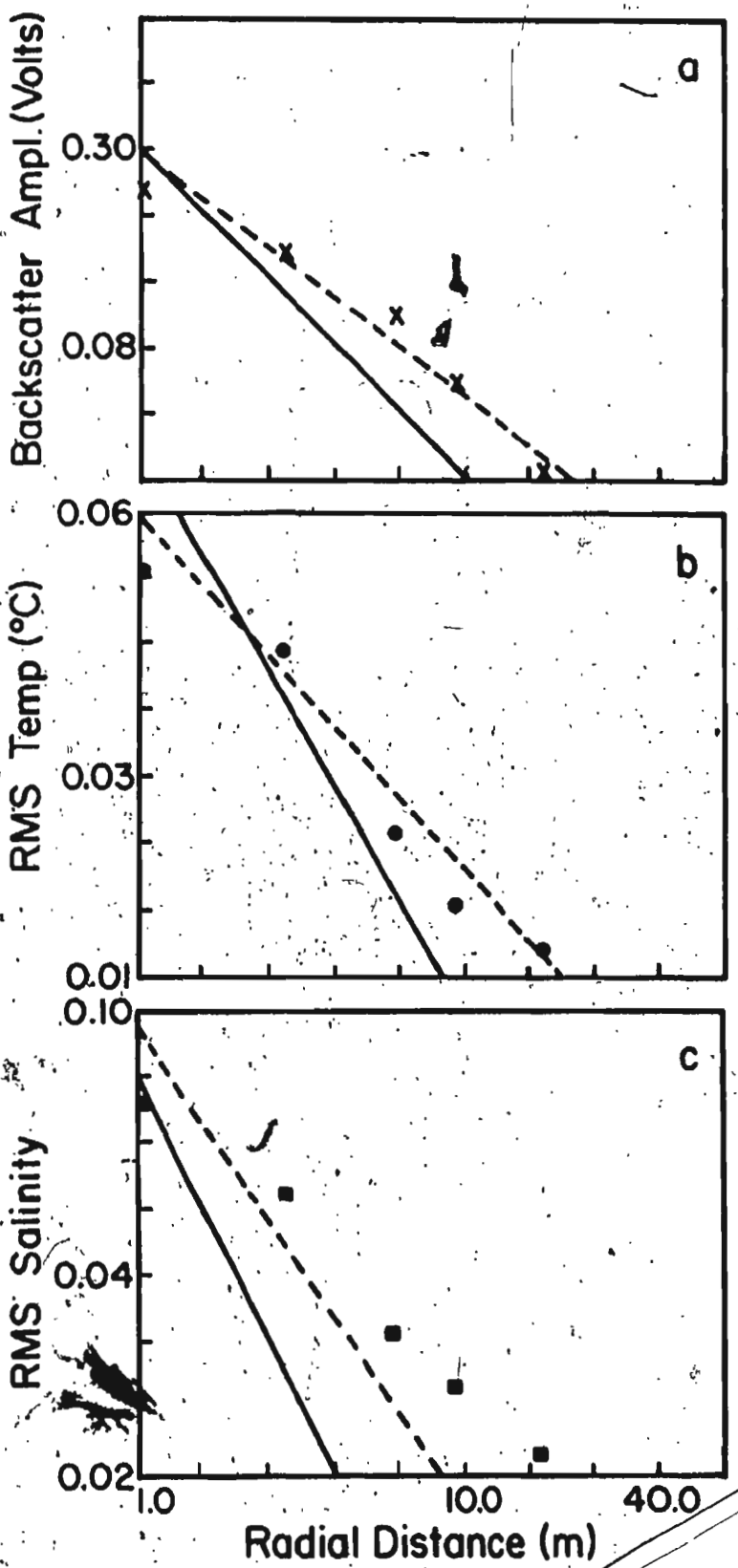

Figure 6.11 (a) Log-log plot of the backscatter amplitude shown in Figure 6.7a (b) and (c) Log-log plots of the temperature and salinity fluctuations shown in Figure 6.7a. Again the solid and dashed lines are $1/r$ and $1/r^{3/4}$ drop-off rates.

CHAPTER 7. SUMMARY AND CONCLUSIONS

This thesis consists of three main parts: (1) analysis of the observations of the buoyant plume and ambient environment from the CTD, current meter and acoustic backscatter data, (2) comparisons of numerical model results of the plume geometry and vertical velocities with the acoustic backscatter observations, (3) investigation of the acoustic backscatter amplitudes versus the fine structure in the temperature and salinity fields.

The buoyant plume was mapped by an acoustic sounder at 192 kHz and a microwave positioning system. The acoustic sounding transects were spaced at approximately 10 m intervals over the plume area. A second mapping of the plume was made in conjunction with a grid of CTD stations while the launch was four-point moored. In addition, visual observations together with CTD and current meter measurements were made at the vent location using the submersible PISCES IV. From these observations the geometry of the rising and spreading plume was determined. Also the vertical velocities of the rising plume can be estimated directly from the scattering structures in the acoustic images. The results demonstrate the advantages of using acoustic remote sensing techniques to detect and characterize buoyant plumes in the ocean.

Two separate models were employed. The first was a dimensional asymptotic model, the second was a numerical model for buoyant jets and plumes. The buoyant plume under study here has very little initial momentum. The main discharge region is 2.0 to 4.0 m in horizontal extent with several smaller points of

discharge nearby. The discharge water converges as it rises to merge into one large plume-like flow a short distance from the bottom. The dimensional analysis in sections 5.2 and 5.3 together with the observations indicate that this flow is buoyancy dominated at approximately one meter above bottom. The maximum height of rise estimated with this model using the observed initial conditions as inputs is about 42 m. This result is somewhat higher than that observed experimentally but within 15 to 20 percent.

The numerical model uses the horizontally integrated conservation equations of mass, momentum and buoyancy with Gaussian profiles to evaluate the integrals. The model calculations started off at one meter above the bottom where the flow was found to be plume-like. The maximum height of rise calculated numerically is within 15 percent of the heights measured acoustically. The experimentally determined plume widths as a function of height show variations similar to those calculated by the model. The model approximates the experimental results more closely with decreasing freshwater discharge. For a discharge rate of 0.05 m^3/sec and a discharge salinity of 29.5 we get the best fit between the model and the observations. The range of freshwater discharge rates estimated from the 1.0 to 2.0 m decrease in the water level of the lake was between 0.06 to 0.13 m^3/sec. The results of the numerical calculations point to the lower end of this range in contrast to the value of 0.14 m^3/sec determined from heat loss considerations by Sadler and Serson. The vertical velocities calculated by the model are of the same order as those inferred from the acoustic images but there are discrepancies between the predicted and observed variation of velocity with height.

Several recent studies (Munk and Garrett, 1973; Proni and Apel, 1975; Goodman and Kemp, 1981) have suggested that turbulent microstructure may cause acoustic backscatter at detectable levels. It is concluded in this thesis that

turbulent microstructure is likely responsible for the observed acoustic backscatter. This conclusion is supported by a number of experimental observations. The discharge water at the vent appears to be clear and free of bubbles and suspended sediments. Comparisons of the acoustic data and the rms fine structure in the temperature and salinity fields show some correlation. Estimates of the temperature and salinity microscales satisfy the scale-to-wavelength condition for acoustic backscatter to occur. Also very small turbulent eddies made visible by large variations in the optical refractive index were observed from the submersible. Finally it was shown that the radial decay of the backscatter could not be explained by simple spreading of conservative point scatters. It was also shown that entrainment in the spreading plume is not important at least for $r > 10.0$ m. By assuming a balance between advection and dissipation as in grid turbulence we expect a $1/r$ drop-off in the turbulent velocity field and from self-preservation arguments we get a $1/r^{3/4}$ drop-off in scalar fluctuations (Hinze, 1975, p. 301). In section 6.4 it was shown that the radial decay of the backscatter-amplitudes in the spreading plume fits a $1/r^{3/4}$ law reasonably well. Also the decay of the backscatter and the temperature and salinity fluctuations from CTD transect B through the plume show some agreement with the $1/r^{3/4}$ drop-off rate although the number of points in this case are insufficient.

REFERENCES

Abraham, G., Horizontal Jets is Stagnant Fluid of other Density, Proc. ASCE, J. Hyd. Div., 91, HY1 pp. 63 - 68, 1967.

Albertson, M. L., Y. B. Dai, R. A. Jensen, and H. Rouse, Diffusion of Submerged Jets, Trans. ASCE, 115, pp. 639 - 697, 1950.

Batchelor, G. K., Wave Scattering Due To Turbulence, *Proc. of the Symp. on Naval Hydrodynamics*, F.S. Sherman, ed., NAS - NRC, Publ. 518, pp. 409 - 430, 1957.

Blume, H. J. C., B. M. Kendall, and J. C. Fedors, Multifrequency Radiometer Detection of Submarine Freshwater Sources Along the Puerto Rican Coastline, *J. Geophy. Res.*, **86**, *C6*, 5283 - 5291, 1981.

Clay, C. S., and H. Medwin, *Acoustical Oceanography*, 544 pp., John Wiley, New York, 1977.

Ditmars, J. D. Computer Program for Round Buoyant Jets into Stratified Ambient Environments, W. M. Keck Lab., Technical Memorandum 69 - 1, California Institute of Technology, March, 1969.

Dunbar, M. Curious open water feature in the ice at the head of Cambridge Fiord. Extrait des comptes Rendu et Rapports, Assemblee Generale de Toronto, T. IV, pp. 514 a 519, Soc. Int. Geograph. (Gentbrugge 1958).

Fan, L. N., and N. H. Brooks, Horizontal Jets in Stagnant Fluid of other Density, Proc. ASCE, J. of Hyd. Div. HY2, pp. 423 - 429, 1966.

Fan, L. N., Turbulent Buoyant Jets into Stratified or Flowing Ambient Fluids, W. M. Keck Lab. Report No. KH - R - 15, California Institute of Technology, June, 1967.

Fan, L. N., and N. H. Brooks, Numerical Solutions of Turbulent Buoyant Jet Problems, W. M. Keck Lab. Report No. KH - R - 18, California Institute of Technology, January, 1969.

Farmer, D. M., and J. D. Smith, Tidal Interactions of Stratified Flow with a Sill in Knight Inlet, *Deep Sea Research*, **27**, pp. 239 - 254, 1980.

Fischer, H. B., E. J. List, R. C. Y. Koh, J. Imberger, and N. H. Brooks, Mixing in Inland and Coastal Waters, 483 pp., Academic Press, New York, 1979.

Gill, A. E., *Atmosphere-Ocean Dynamics*, 662 pp., Academic Press, New York, 1982.

Goodman, L., and K. Kemp, Scattering from Volume Variability, *J. of Geophysical Res.*, **86**, No. C5, pp. 4083 - 4088, 1981.

Haury, L. R., M. G. Briscoe, and M. H. Orr, Tidally Generated Internal Wave Packets in Massachusetts Bay, U.S.A., *Nature*, **278**, 312 - 317, 1979.

Hay, A. E., Remote Acoustic Imaging of the Plume from a Submarine Spring in an Arctic Fiord, *Science* **255**, 1154 - 1156, 1984.

Hay, A. E., On the Remote Acoustic Detection of Suspended Sediment at Long Wavelengths, *J. Geophys. Res.* **88**, 7525 - 7542, 1983.

Hay, A. E., R. W. Burling, and J. W. Murray, Remote Acoustic Detection of a Turbidity Current Surge, *Science* **217**, 833 - 835, 1982.

Hay, A. E., and E. B. Colbourne, Acoustic Remote Sensing of an Internal Surge in Insuguin Fiord, Baffin Island, In progress, 1987.

Kaye, G. T., Correlation between Acoustic Scatterers and Temperature Gradients, *J. Mar. Res.*, **37**, 319 - 326, 1979b.

List, E. J., Turbulent Jets and Plumes, *Ann. Rev. Fluid Mech.* **14**, 189, 1982.

Mackenzie, K., Nine Term Equation for Sound Speed in the Oceans, *J. Acoust. Soc. Amer.*, **70**, 807, 1981.

Manheim, F. T., *Trans. N. Y. Acad. Sci.*, **29**, 839, 1967.

Merewetter, R., M. S. Olsson, and P. Lonsdale, Acoustically Detected Hydrocarbon Plumes rising from 2 km depths in Guaymas Basin, Gulf of California, *J. Geophys. Res.*, **90**, 3075 - 3085, 1985.

Millero, F. J., Chen, C. T., Bradshaw, A., and Schleicher, K., A new High Pressure Equation of State for Seawater, *Deep-sea Res.*, **27A** 255 - 264, 1980,

Millero, F. J., and A. Poisson, International one Atmosphere Equation of state for Seawater, *Deep-Sea Res.*, **28A**, 625 - 629, 1981.

Morton, B. R., Forced Plumes, *J. of Fluid Mechanics*, **5**, pp. 151 - 163, 1959.

Morton, B. R., G. I. Taylor, and J. S. Turner, Turbulent Gravitational Convection from Maintained and Instantaneous Sources, *Proc. Roy. Soc. London*, **A234**, pp. 1 - 23, 1956.

Munk, W., and C. Garrett, Internal Wave Breaking and Microstructure, *Bdry - Layer Met.*, **4**, 37, 1973.

Ottersten, H., K. R. Hardy, and C. G. Little, Radar and Sodar probing of Waves and Turbulence in Statically Stable Clear-Air Layers, *Bdry - Layer Met.*, **4**, 47 - 89, 1973.

Palmer, D. R., and P. A. Rona, Acoustic Imaging of High Temperature Hydrothermal Plumes at Seafloor Spreading Centers, *J. Acoust. Soc. Amer.*, **80** (3), 888, 1986.

Pelech, I., G. G. Zipfel, and R. L. Holford, A Wake Scattering Experiment in Thermally Stratified Water, *J. Acoust. Soc. Amer.*, **73**, 528, 1983.

Proni, J. R., and J. R. Apel, On the use of High Frequency Acoustics for the study of Internal Waves and Microstructure, *J. Geophysical Res.*, **80**, 1147 - 1151, 1975.

Sadler, H. and H. Serson, An Unusual Polynya in an Arctic Fiord, In *Fiard Oceanography*, H. Freeland et al., Plenum 299 - 304, 1980.

Syvitski, J. P., and C. P. Blakeney, Sedimentology of Arctic Fiords, Canadian Data Report of Hydrography and Ocean Sciences, No. 12, Vol. 1., 1983.

Tatarski, V., *Wave Propagation in a Turbulent Medium*, Dover, 68, 1961.

Taylor, G. I., Flow Induced by Jets, *Journal Aerospace Science, Vol.* **25**, 464 - 465, 1958.

Tennekes, H. and J. Lumley, *A First Course in Turbulence*, 300 pp., MIT Press, 1972.

Thorpe, S., and J. Brubaker, Observations of Sound Reflection by Temperature Microstructure, *Limnol. Ocgy.*, **28**, 601, 1983.

Turner, J. S., *Buoyancy Effects in Fluids*, 368 pp., Cambridge U. P., 1973.

Vincent, C. A., R. A. Young, and D. J. P. Swift, The Relationship between Bedload and Suspended Sand Transport, *J. Geophys. Res.*, **87**, 4163 - 4170, 1982.

Weston, D. C., Observations on a Scattering Layer at the Thermocline, *Deep Sea Res.*, **5**, 44 - 50, 1958.

Young, R. A., J. T. Merrill, T. L. Clarke, and J. R. Proni, Acoustic Profiling of Suspended Sediments in the Marine Bottom Boundary Layer, *Geophys. Res. Lett.*, **9**, 175 - 178, 1982.

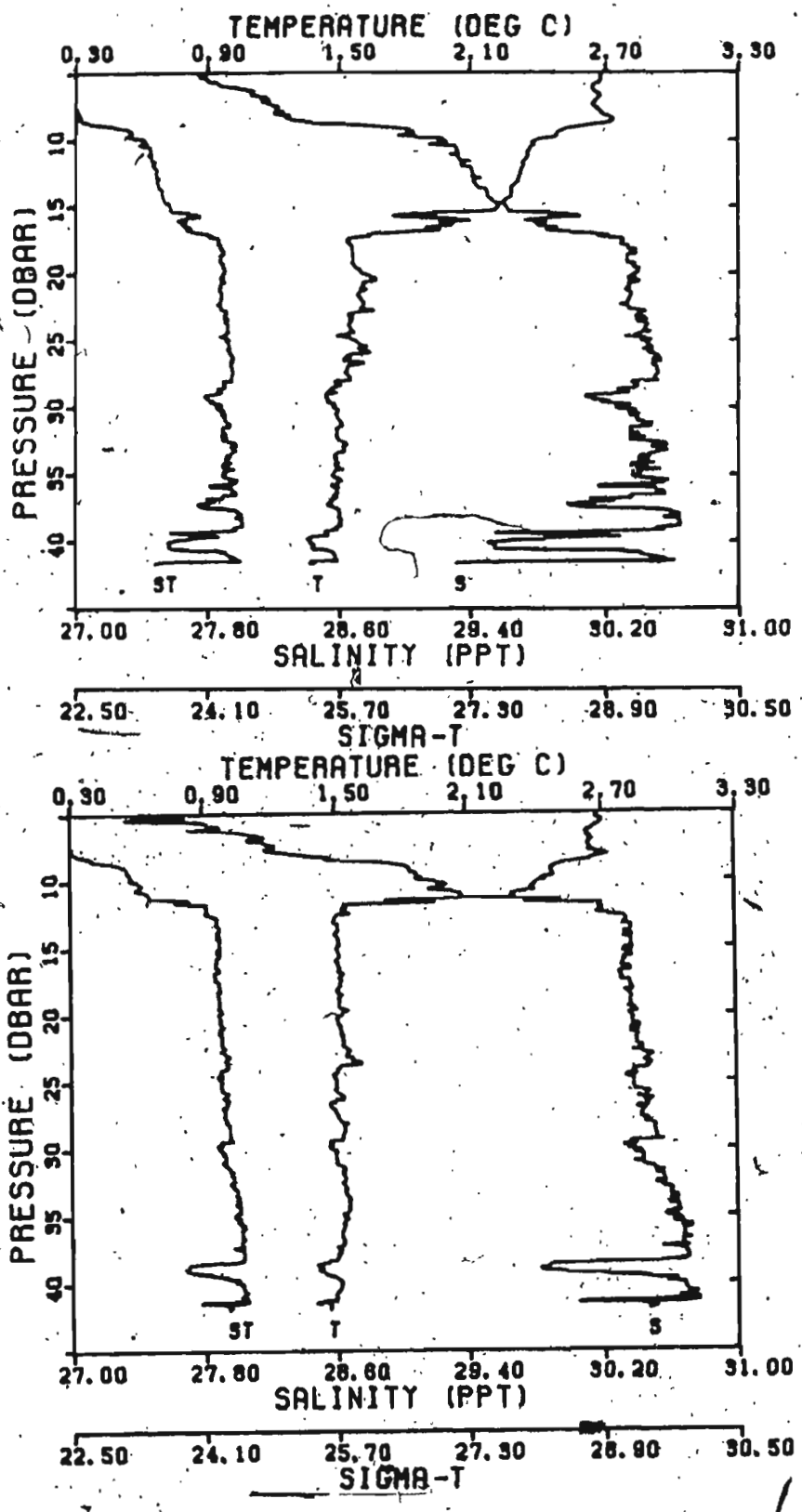

Figure A1. CTD profiles corresponding to cast numbers 2 (top) directly over the vent in the rising plume and 3 (bottom) in the rising plume.

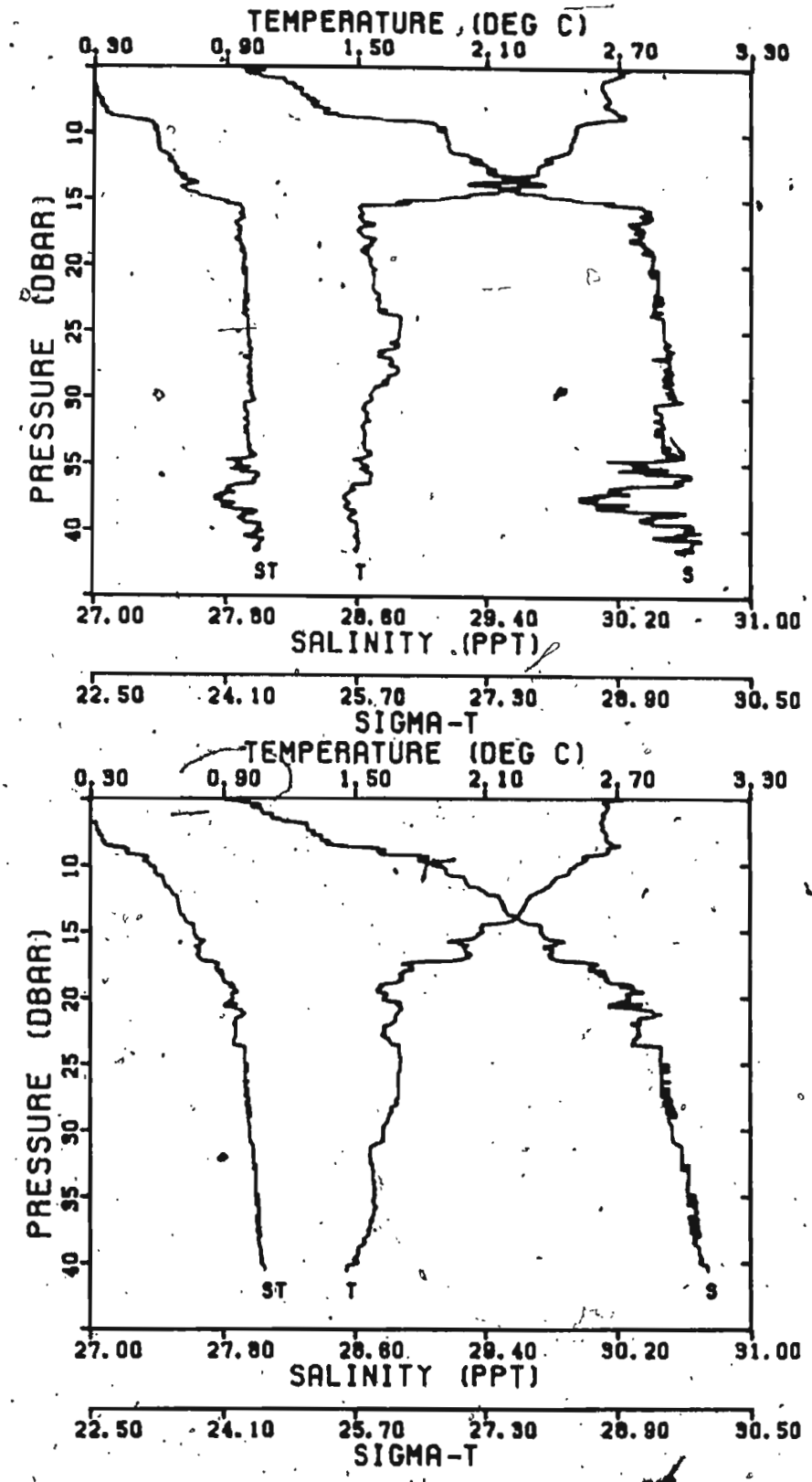

Figure A2. CTD profiles corresponding to cast numbers 4 (top) in the rising plume and 6 (bottom) in the spreading plume.

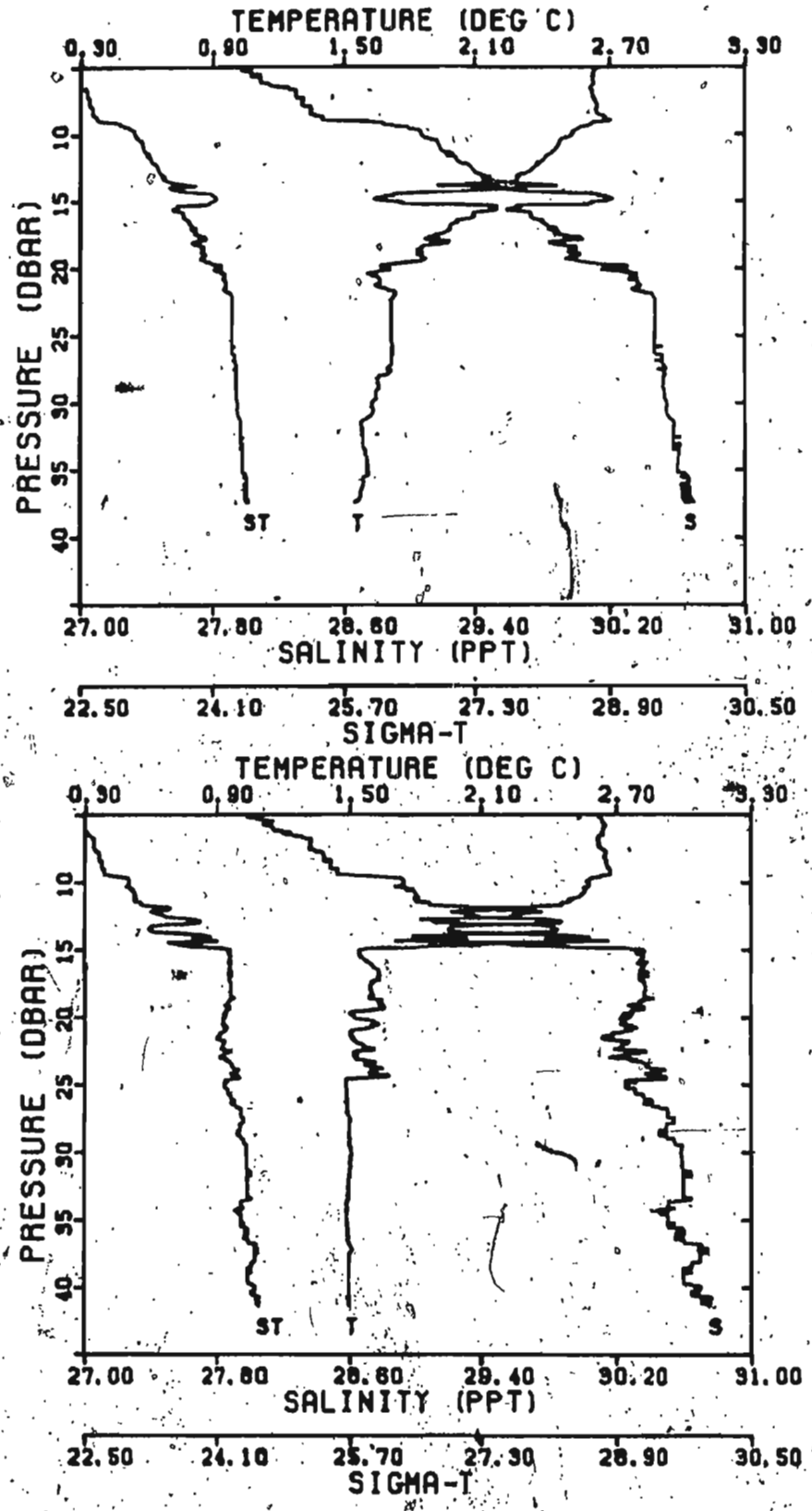

Figure A3. CTD profiles corresponding to cast numbers 7 (top) and 9 (bottom) in the spreading plume.

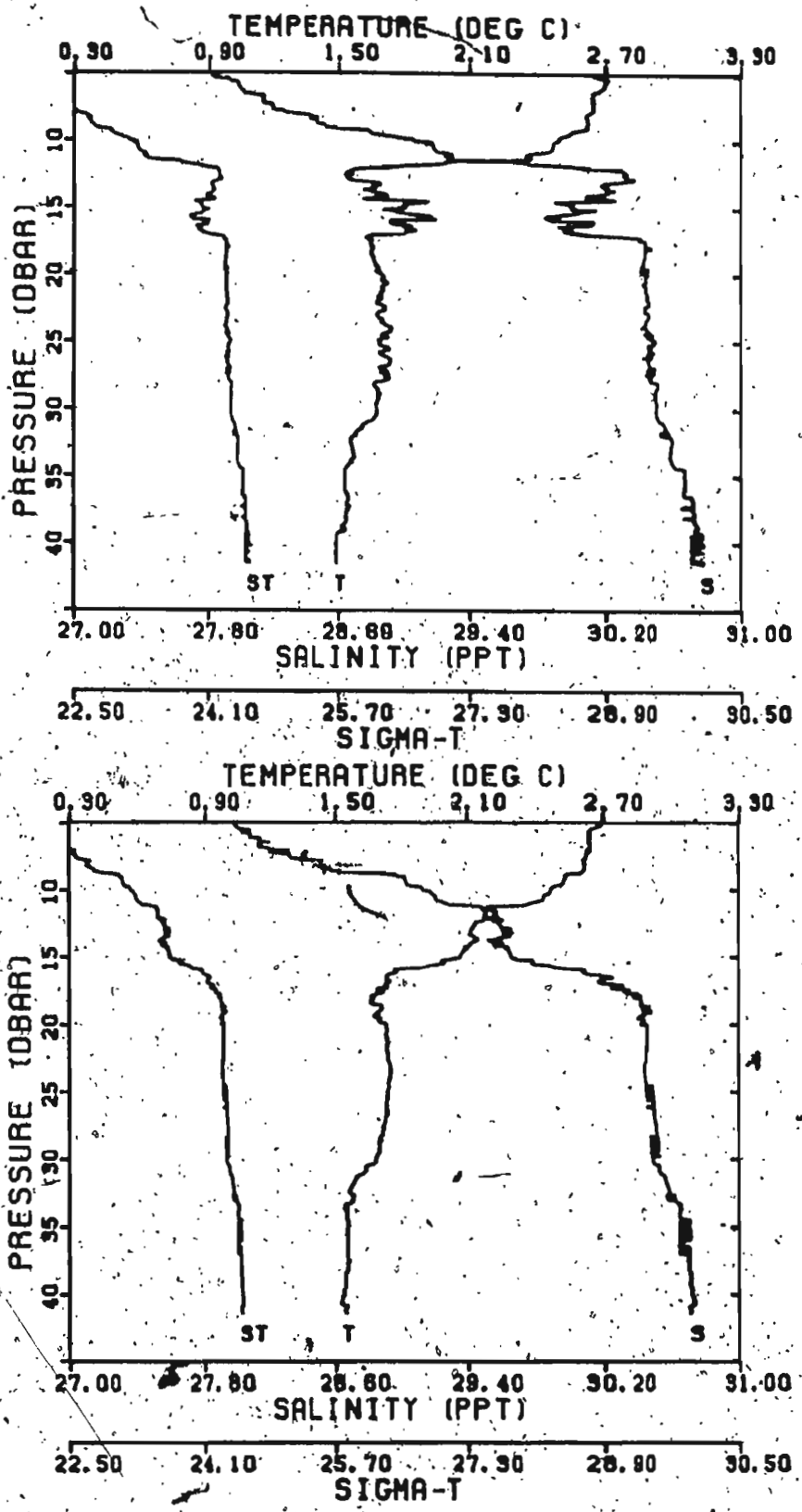

Figure A4. CTD profiles corresponding to cast numbers 10 (top) and 11 (bottom) in the spreading plume.

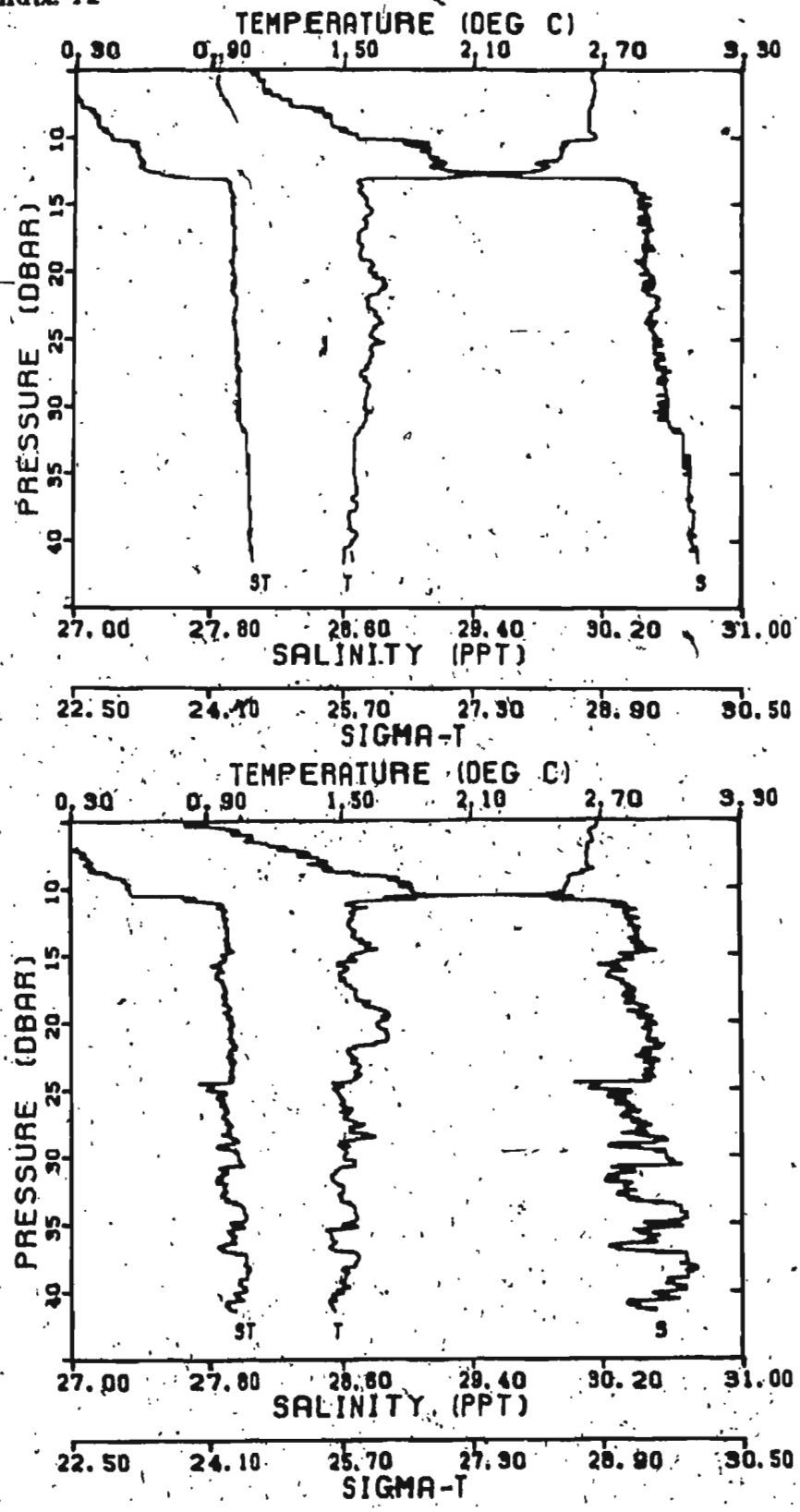

Figure A5. CTD profiles corresponding to cast numbers 12 (top) at the edge of the rising plume and 13 (bottom) in the rising plume.

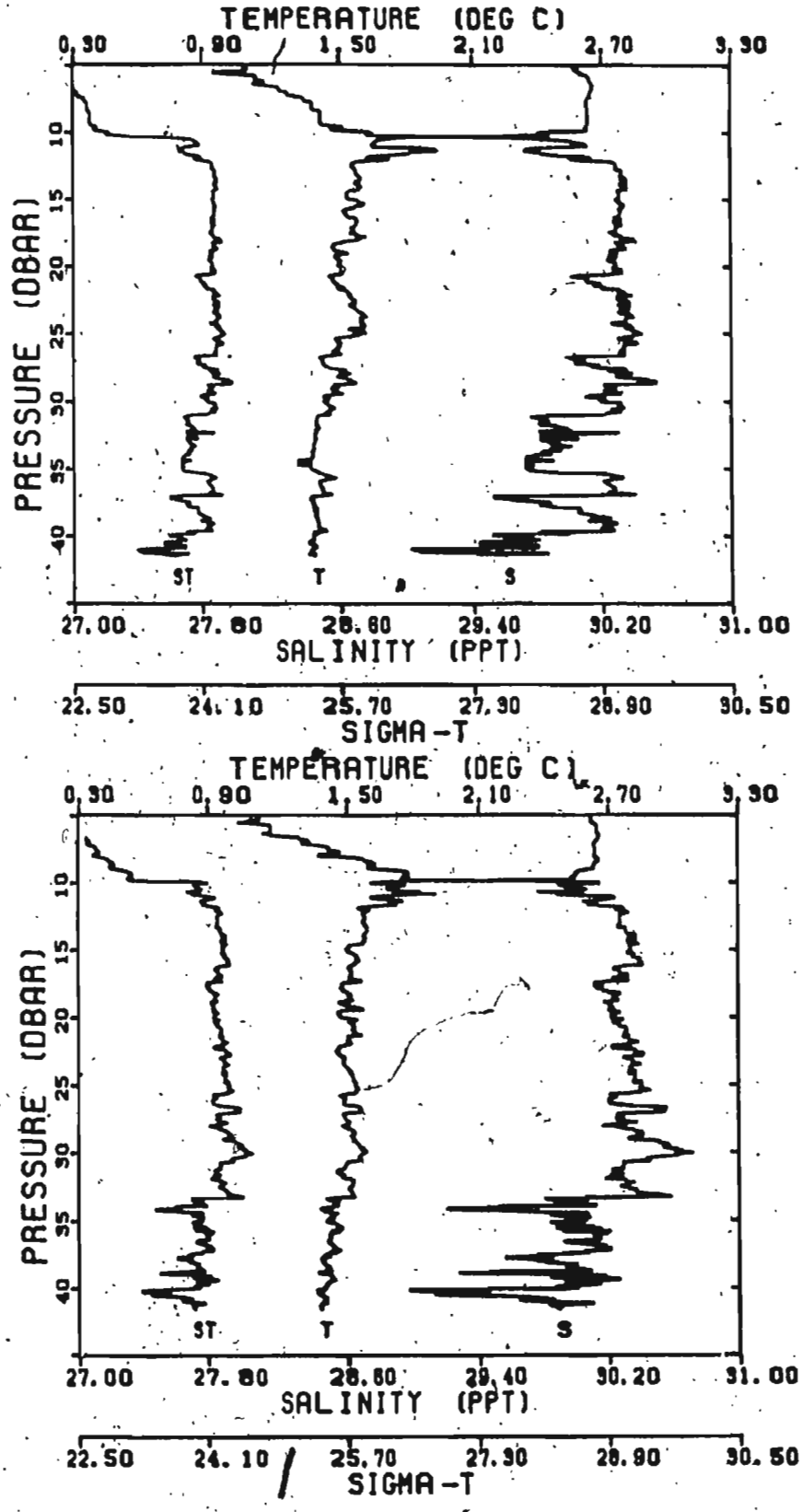

Figure A6. CTD profiles corresponding to cast numbers 14 (top) and 15 (bottom) in the rising plume.

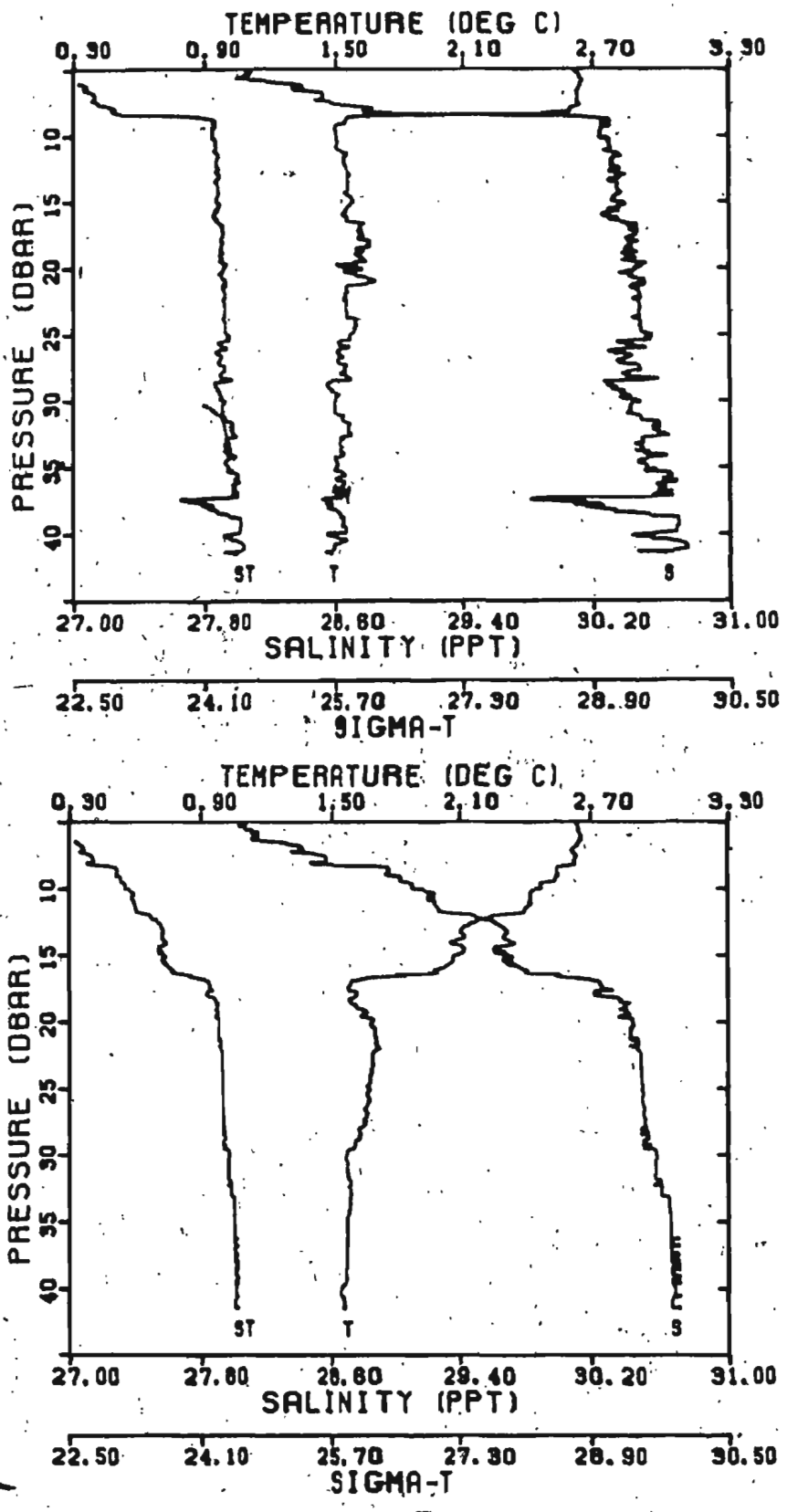

Figure A7. CTD profiles corresponding to cast numbers 16 (top) in the rising plume and 17 (bottom) in the spreading plume.

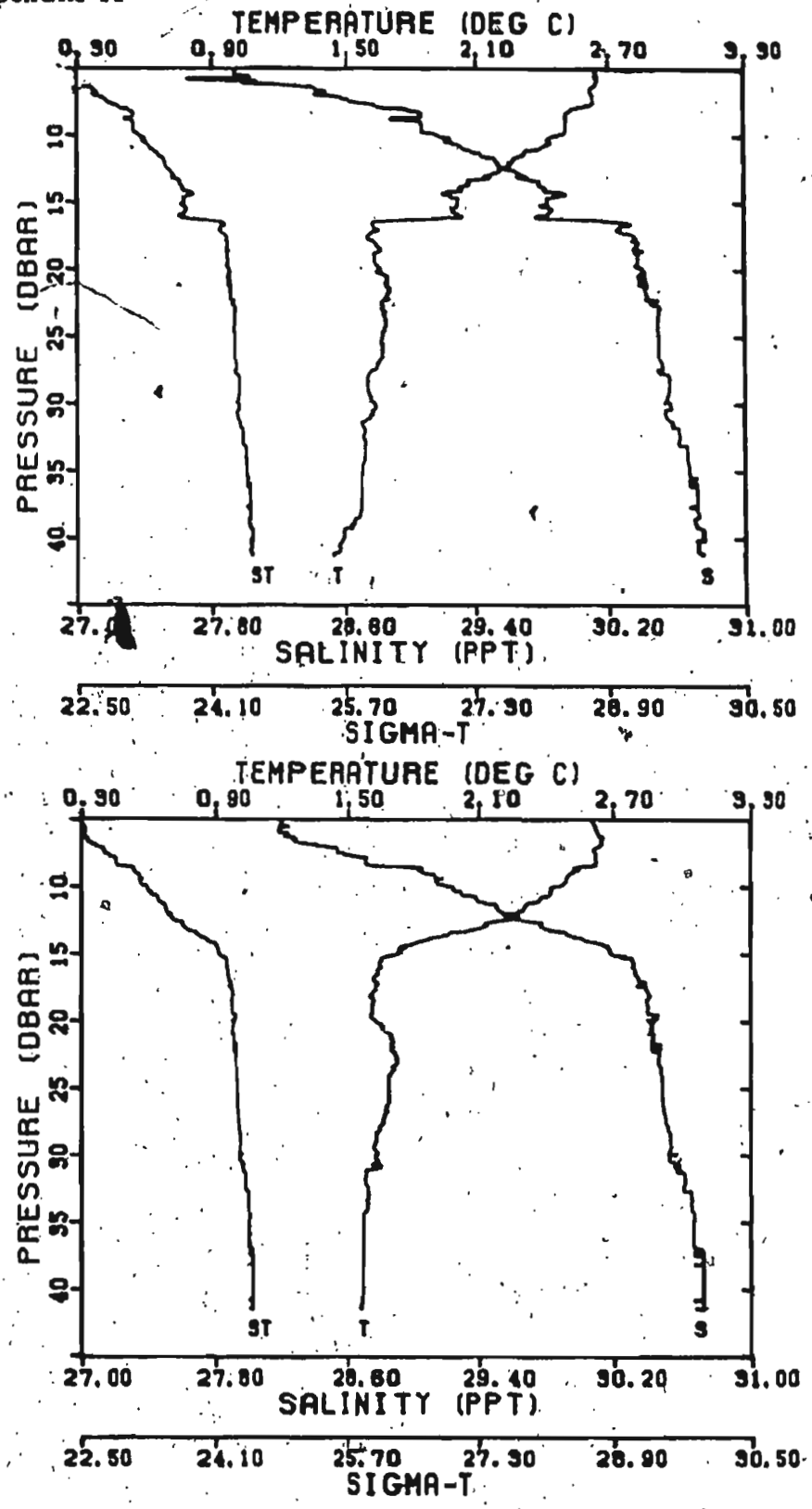

Figure A8. CTD profiles corresponding to cast numbers 18 (top) at the edge if the spreading plume and 19 (bottom) out of the plume.

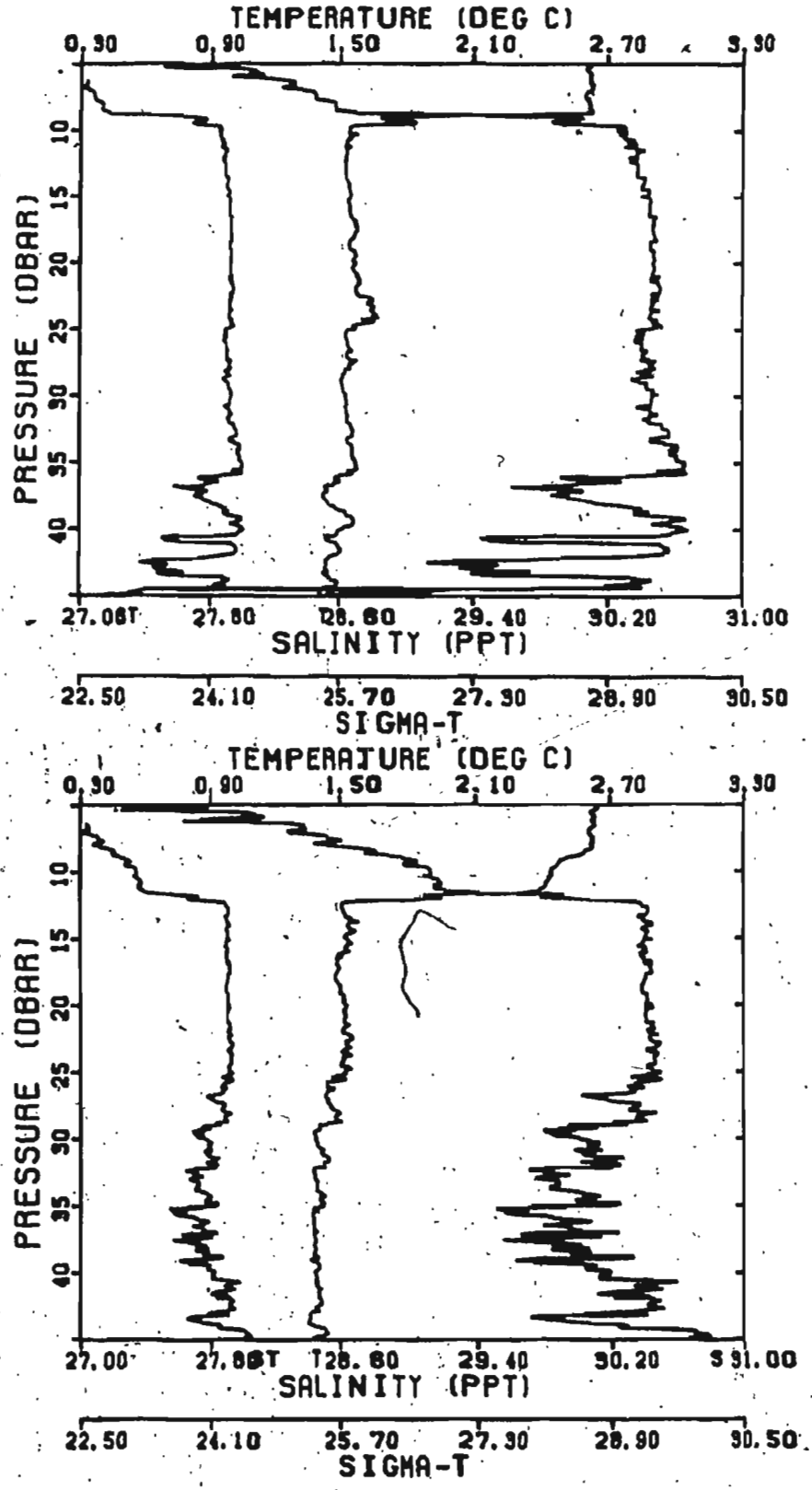

Figure A9. CTD profiles corresponding to cast numbers 21 (top) and 22 (bottom) directly over the vent in the rising plume.

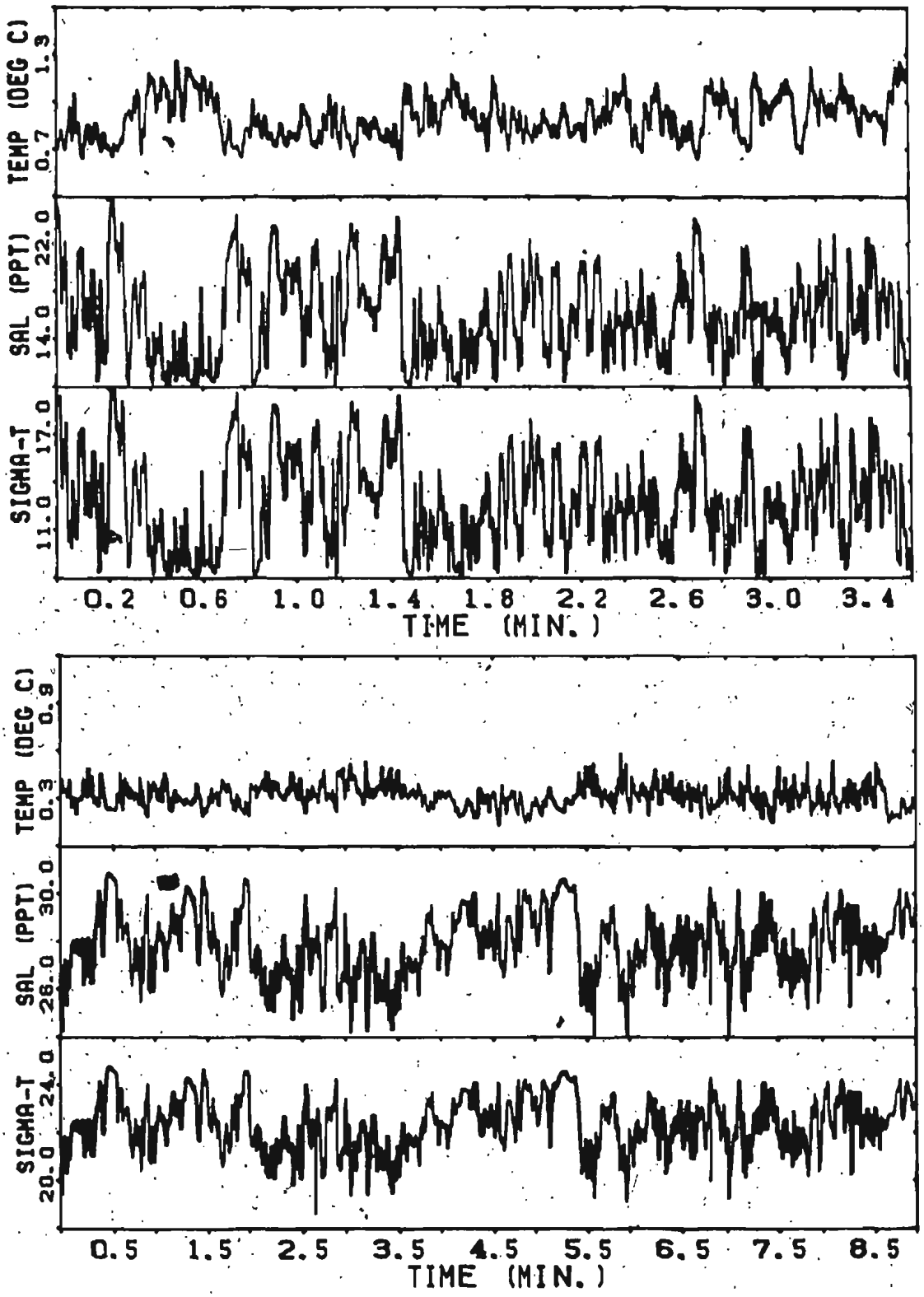

Figure B1. CTD time series obtained from the submersible at the vent about 48 m depth with the sensors directly in the discharge water.

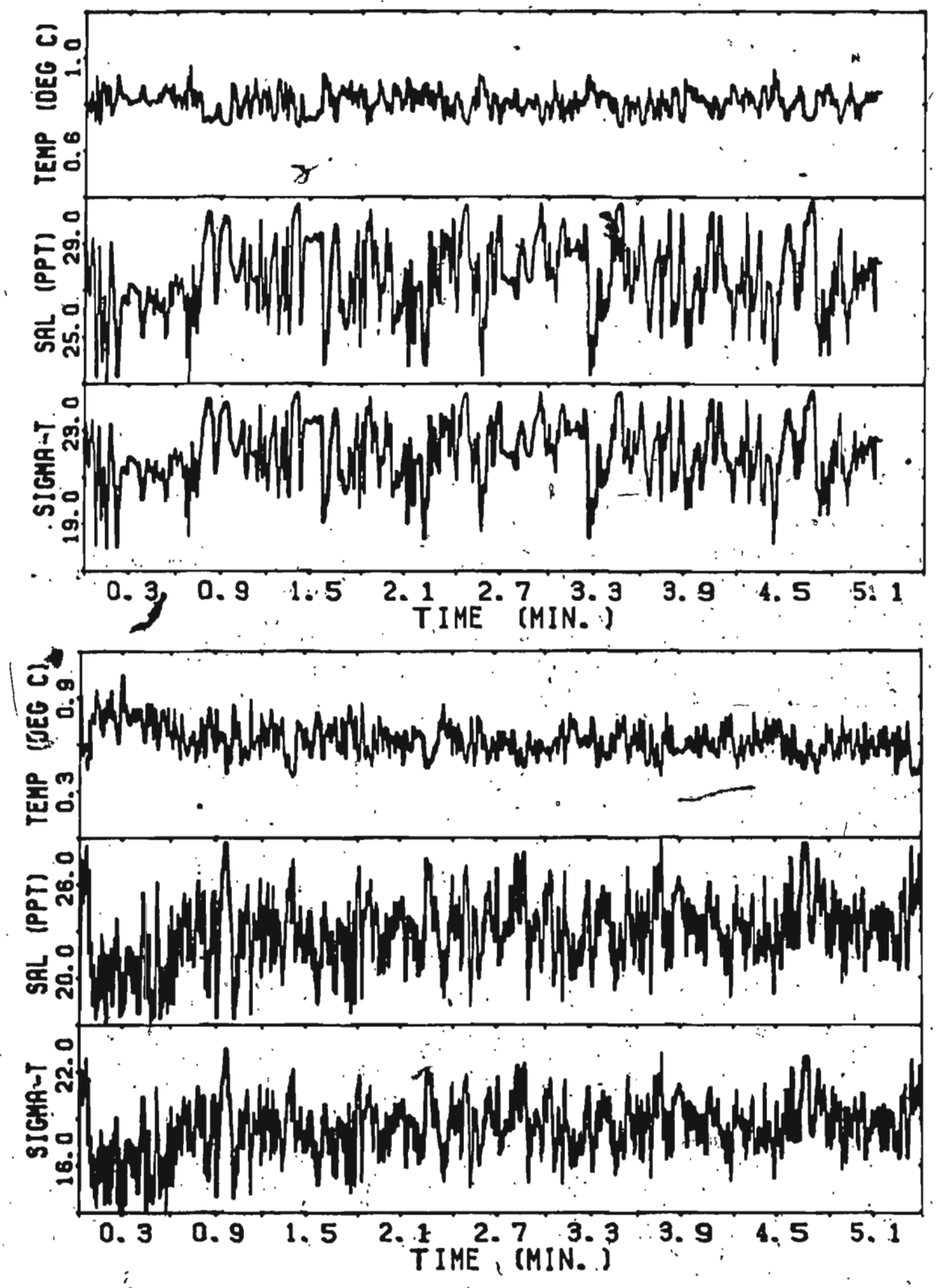

Figure B2. CTD time series obtained from the submersible at the vent close to the bottom with the sensors in the discharge plume.

Appendix C

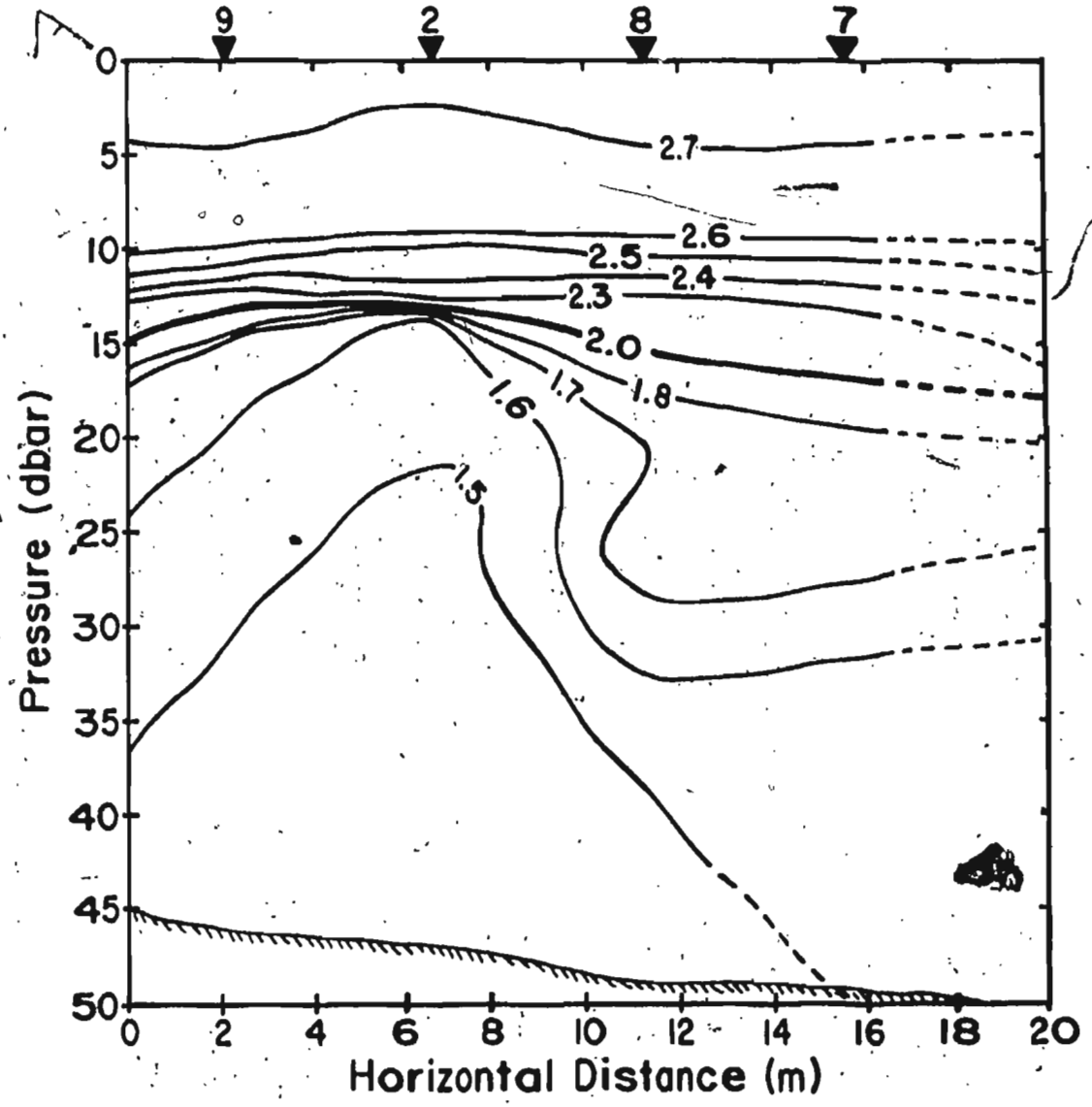

Figure C1. Temperature section for CTD transect A.

Appendix C

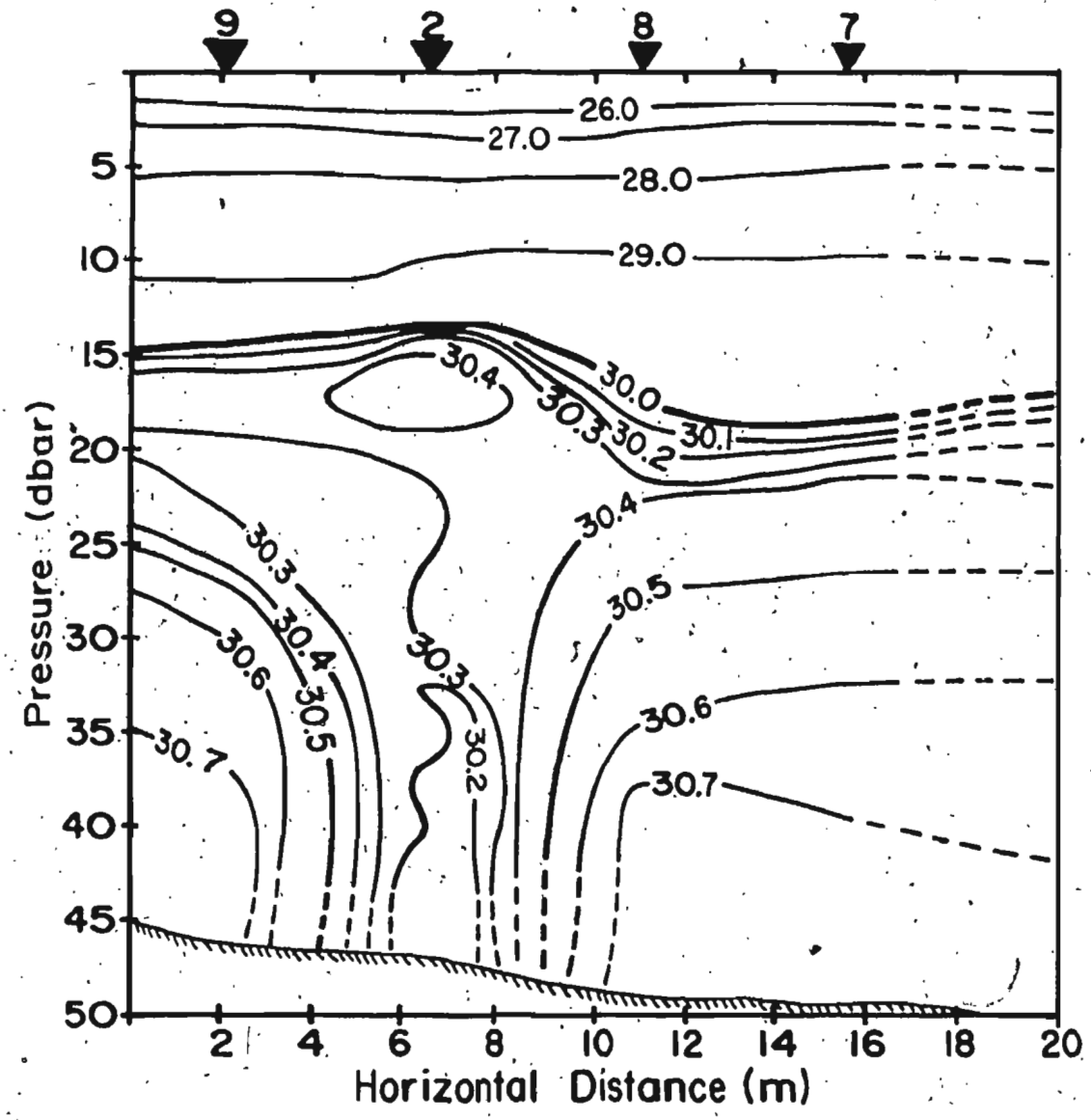

Figure C2. Salinity section for CTD transect A.

Appendix C

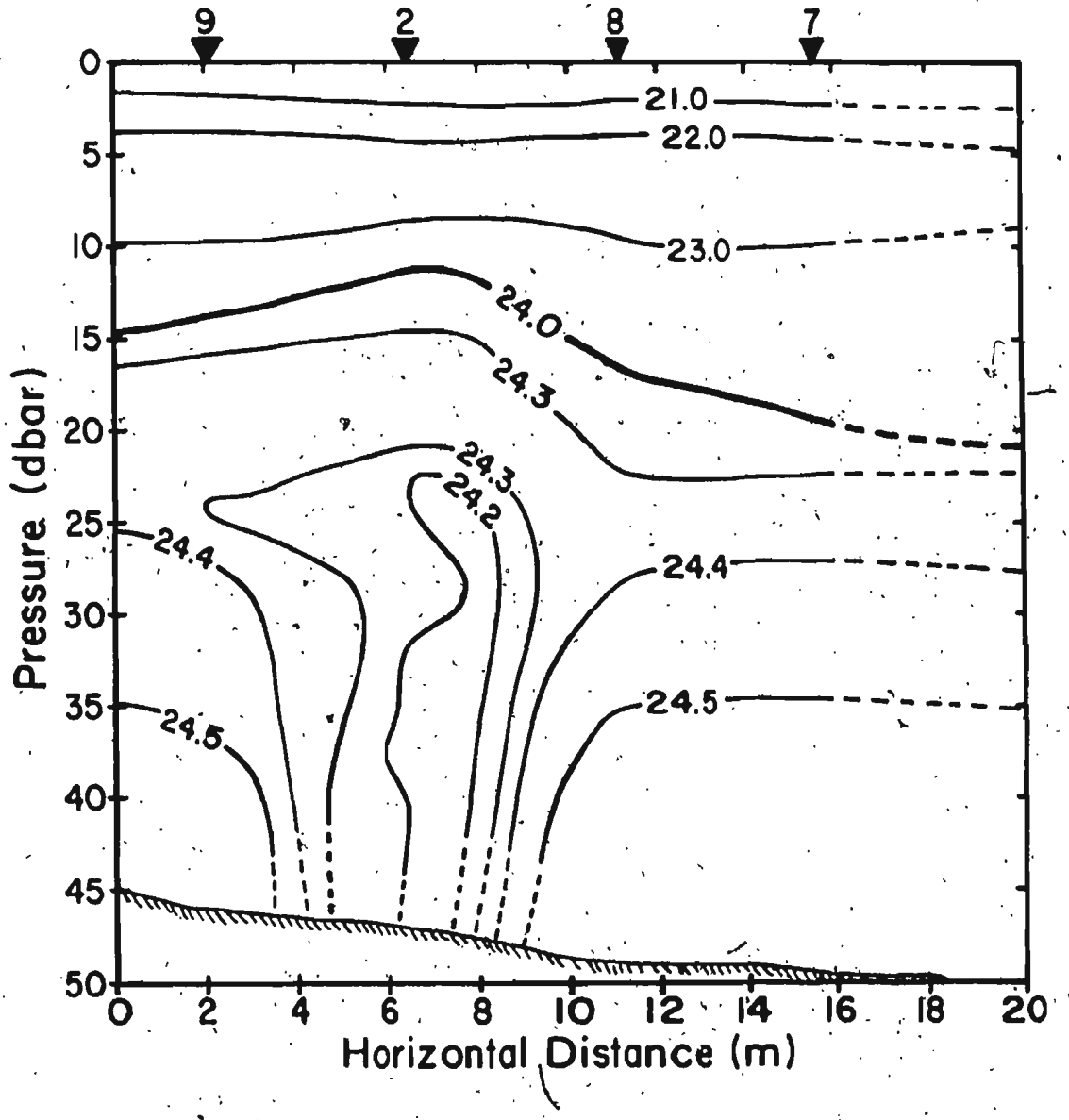

Figure C3. Sigma-t section for CTD transect A.

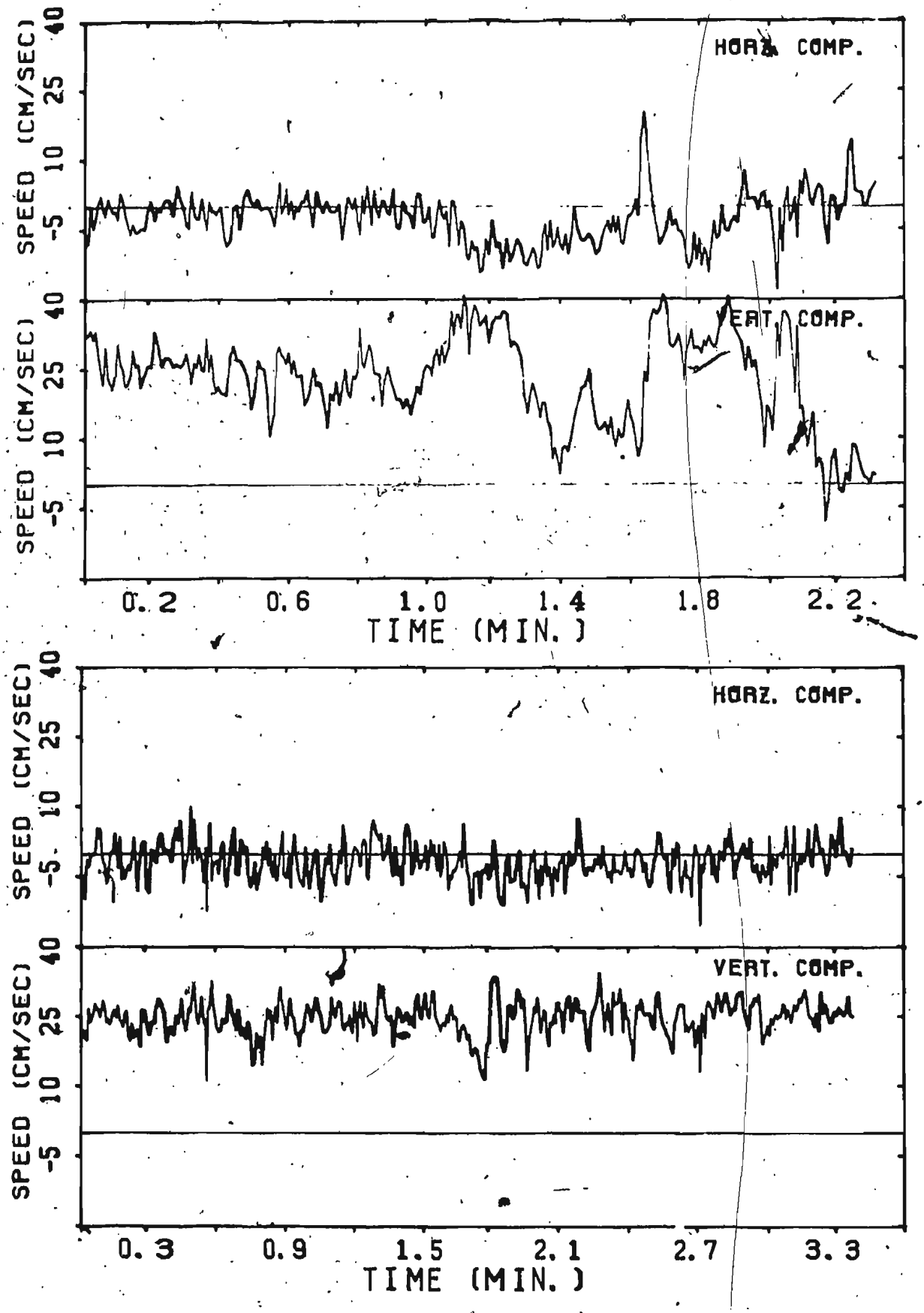

Figure D1. Horizontal and vertical velocities in the rising plume obtained from the submersible at the vent about 1.0 m from the bottom.

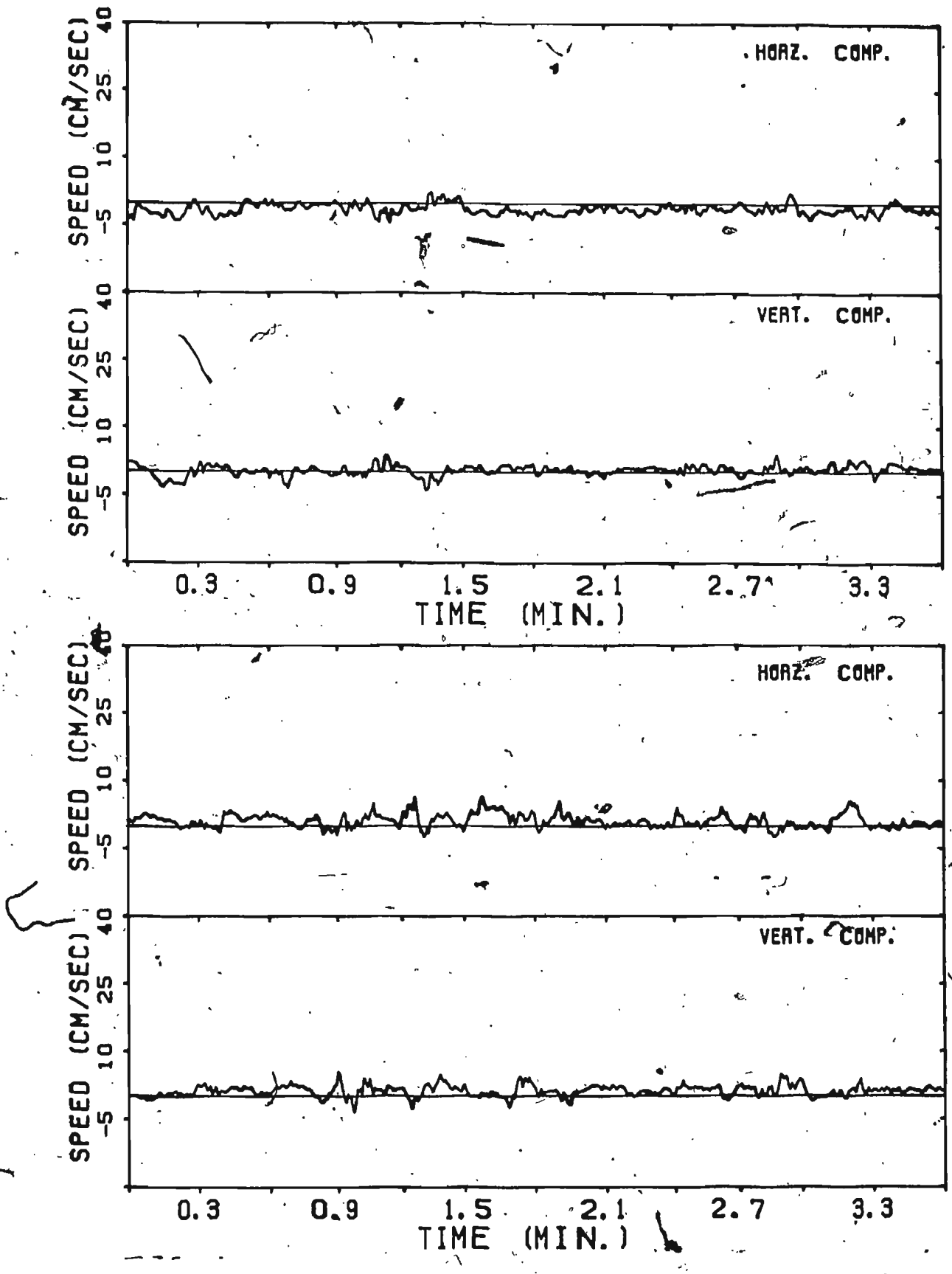

Figure D2. Horizontal and vertical velocities obtained from the submersible a short distance from the vent, showing the ambient currents near the plume.

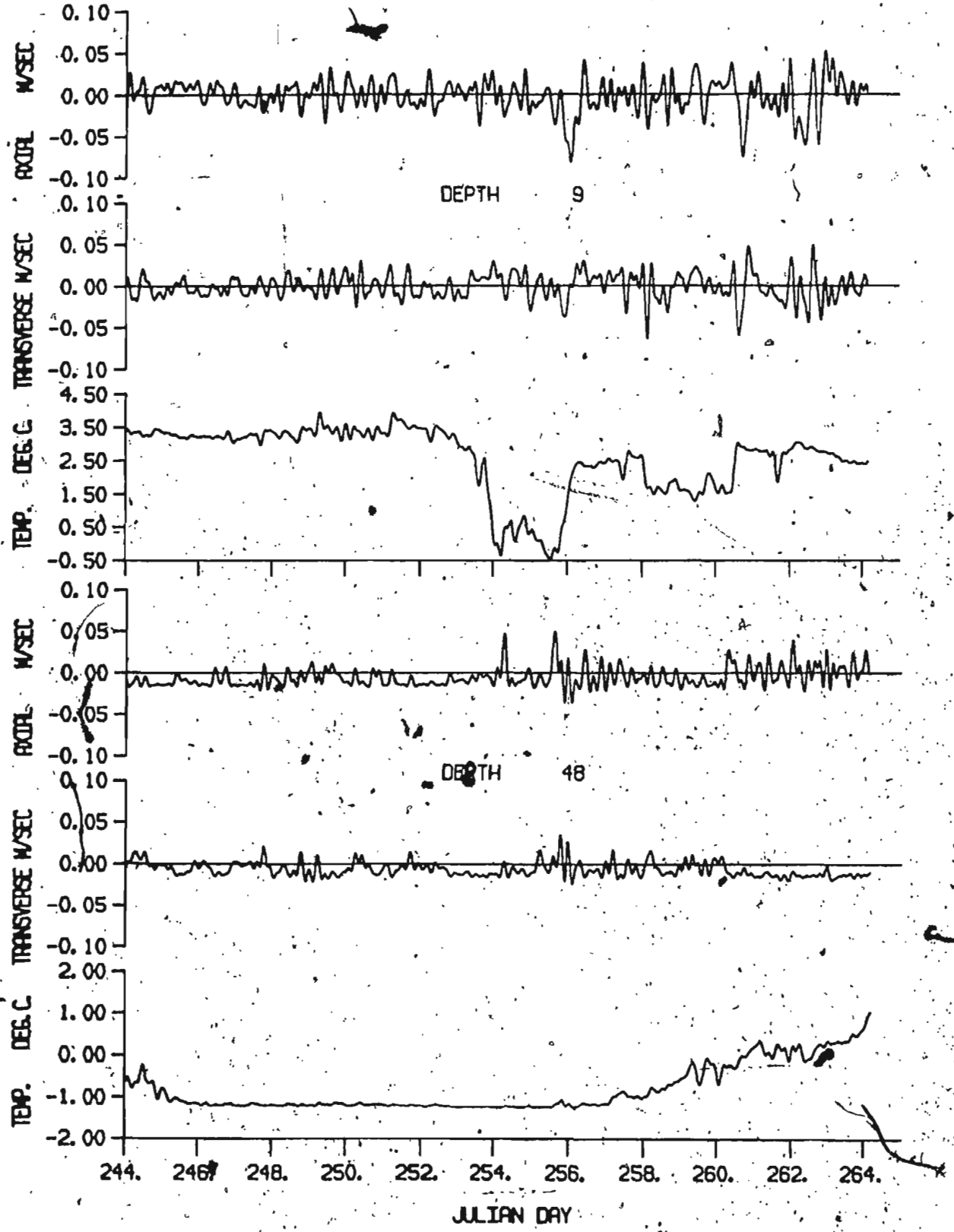

Figure D3. Low passed filtered axial and transverse currents and temperatures at 9.0 and 48.0 m depth for September 1985. The filter had a cutoff period of 4.0 hours.